Development of functional biomaterials by self-assembled nanostructures.(Dissertation_全文)

AUTHOR(S):

Yoshii, Tatsuyuki

Development of functional biomaterials by self-assembled nanostructures.

Tatsuyuki Yoshii

2014

Preface and Acknowledgements

The studies presented in this dissertation have been carried out under the direction of Professor Itaru Hamachi at the Department of Synthetic Chemistry and Biological Chemistry, Graduate School of Engineering, Kyoto University, from April 2005 to September 2014. The study is focused on the development of functional biomaterials by self-assembled nanostructures.

My heartfelt appreciation goes to Prof. Itaru Hamachi whose comments, suggestions, and encouragement were of inestimable value for my study. I am also indebt to Associate Prof. Masato Ikeda for his valuable and helpful advice, discussions and encouragement. I extend my sincere gratitude to Prof. Akio Ojida, Associate Prof. Shigeki Kiyonaka, Associate Prof. Shinya Tsukiji, Assistant Prof. Yousuke Takaoka, for their helpful suggestions.

I wish to acknowledge Prof. Kenji Urayama for technical help for rheological experiments. I also wish to acknowledge Prof. Kenji Matsuda and Assistant Prof. Takashi Hirose for their help with DLS analysis. I also wish to acknowledge Prof. Kazunari Akiyoshi, Dr. Sadaatsu Mukai, Prof. Shiyoshi Yokoyama and Dr. Hiroyuki Aoki for technical help for CLSM imaging.

I thank the past and present members of Hamachi laboratory for their suggestions and cooperation, and with whom I shared enjoyable time. In particular, I express my appreciation to Assistant Prof. Hiroshi Tsutsumi, Assistant Prof. Takashi Sakamoto, Assistant Prof. Hiroshi Nonaka. I am also grateful to Dr. Takahiro Kohira, Dr. Yoshiyuki Ishida, Dr. Hangxiang Wang, Dr.

Harunobu Komatsu, Dr. Shohei Fujishima, Dr. Assistant Prof. Daishiro Minato, Dr. Keigo Mizusawa, Dr. Takahiro Hayashi, Dr. Rui Kamada, Dr. Rika Ochi, Dr. Hajime Shigemitsu, Dr. Tomonori Tamura, Dr. Shohei Uchinomiya, Dr. Kazuya Matsuo, Dr. Yasutaka Kurishita, Mr. Keishi Kiminami and Mr. Ryosuke Yasui.

I also wish to express mu gratitude to Ms. Ikuyo Miyamae for their help with official business, and I would like to thank JSPS (Japan Society for the Promotion of Science) Young Scientist Fellowship for financial support.

Finally, I wish to express mu deepest gratitude for my parents, Yasuyuki Yoshii and Kisako Yoshii who have supported mu education and encouraged me affectionally.

September 2014

Tatsuyuki Yoshii

Table of contents

General Introduction

Introduction

Molecular self-assembly relies on a spontaneous association of small molecules driven by non-covalent interactions, such as hydrogen bond, π - π interaction, hydrophobic interaction, and electrostatic interaction[1]. Through molecular self-assembly, one can construct various well-ordered nano- and micro-structures including micelles, vesicles, nanofibers, and nanotubes by designing the molecular components (Figure 1). Self-assembled nanostructure have various unique features. (1) Spectroscopic Change: Some designed π-conjugated molecules change their spectroscopic properties depending on self-assembled state.[2] There are several types of spectral change such as fluorescence quenching or increase and color change. (2) Nano-space: Self-assembled nanostructures provide a unique nanospace different from solvent environment. Especially in water, the inner space of the nanostructure is generally hydrophobic and is protected from water or other hydrophilic molecules. (3) Reversible Formation and deformation: Since the driving forces for the formation of self-assembled nanostructure are non-covalent interactions, the structure can be formed reversibly. Thus, the formation of nanostructure can be controlled by the external stimuli.[3] (4) Multivalent effect: The molecules are highly condensed in the nanospace through molecular self-assembly. Thus the nanostructure shows strong multivalent effects. Owing to these four features, the supramolecular materials based on molecular self-assembly hold great promise for a wide range of biological applications such as tissue engineering, biomolecular detection/imaging, and controlled drug release. However, there still remain significant challenges to create and functionalize the supramolecular nanostructure, due to the difficulty to control the self-assembly in aqueous media.

In this introduction section, I summarize the recent progress in the self-assembled nanostructure

of small-molecules, which have emerged as new functional biomaterials for a variety of potential applications.

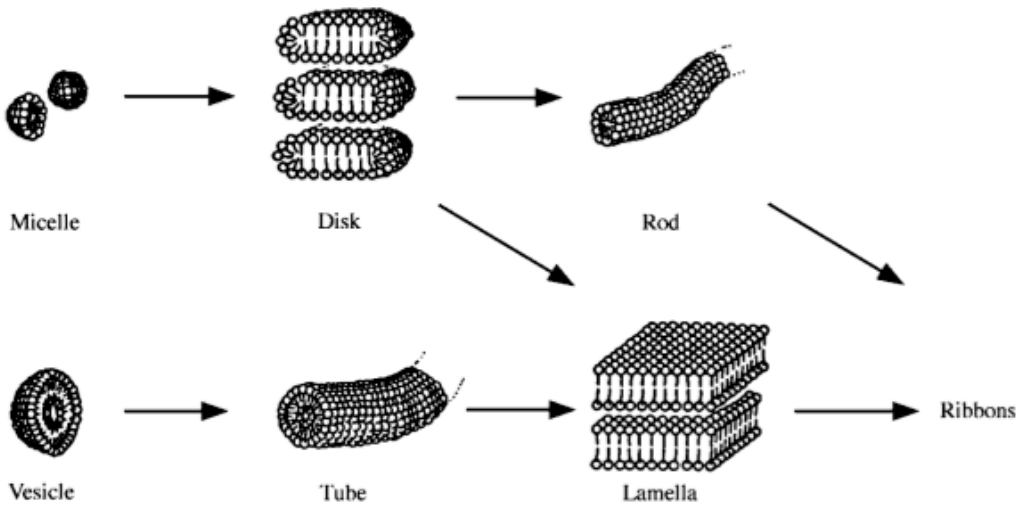

Figure 1. Schematic illustration of aggregate formation by amphiphilic small molecules in aqueous solution.

Outstanding Researches to Explore Chemistry and Biology Using Self-assembled Nanostructure

Biomolecular Sensing

Biomolecules such as proteins, nucleic acids, lipids, sugars and other organic and inorganic molecules have distinct functions to maintain their homeostasis. The concentration and subcellular distribution of these biomolecules are precisely controlled in biological systems. To understand the biological system, the sensing and imaging of the biomolecules is essential. Several researchers have utilized the self-assembled nanostructures to detect come of the important biomolecules.

In biomolecular sensing, the high-throughput technology is attractive. By using the properties of supramolecular hydrogel,[4] Hamachi et al. developed a semi-wet sensor-chip for biomolecules.[5] The supramolecular hydrogel can immobilize proteins, enzymes, or artificial receptors without loss of their activities (Figure 2A). Furthermore, they can be equipped with unique fluorescent read-out systems such as environmentally-sensitive fluorescence enhancement in supramolecular hydrogel. For example, a substrate for a protease bearing an environmentally sensitive dye was embedded in a supramolecular hydrogel. When the protease cleaves the peptide bond of the substrate, the resultant dye translocates from aqueous phase to the hydrophobic domain of the nanofiber, resulting in the increase of the fluorescence intensity (Figure 2B, C). A fluorescence resonance energy transfer (FRET)-based read out system can be also constructed in the supramolecular hydrogel by embedding the FRET acceptor in the nanofiber, which allowed us to estimate the enzyme activity more precisely by taking advantage of ratiometric detection.

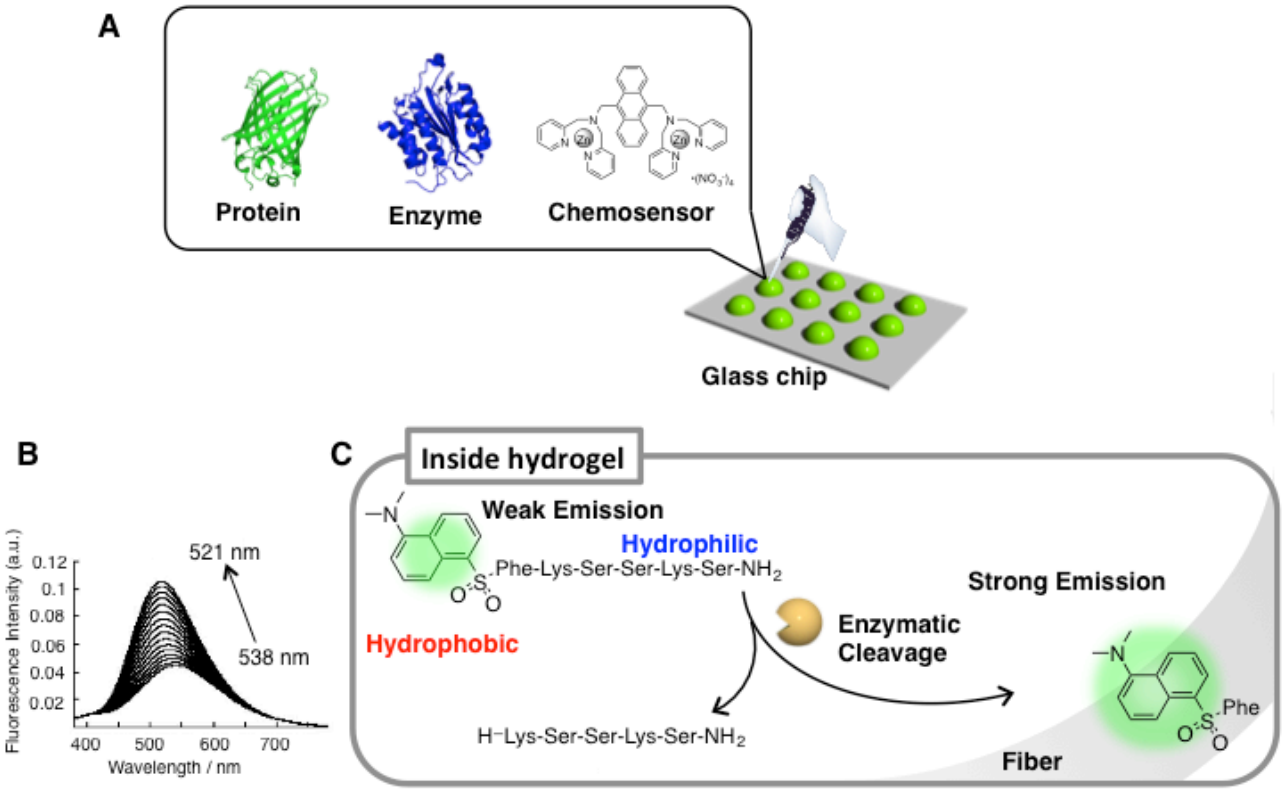

Figure 2. (**A**) Immobilization of various functional molecules to supramolecular hydrogel. (**B**) Fluorescence spectral change of supramolecular gel containing enzymatic substrate upon addition of chymotrypsin. (**C**) Schematic illustration of the fluorescence dye redistribution upon enzymatic cleavage.

A group of fluorogenic molecules show strong fluorescence in self-assembled state but non-emissive in monomer state.[2b,6] Such a phenomenon was called aggregation-induced emission (AIE). The main reason for the fluorescence increase is believed to be the restriction of intramolecular bond rotations. Kikuchi et al. reported an AIE based probe for detection of Sirt1 activity (Figure 3).[7] The enzymatic deacetylation of K(Ac)PS-TPE triggers the electrostatic interaction between the anionic sulphonate and cationic lysine and automatically leads to fluorescence enhancement. Since the fluorescence increase of the probe was restrained in the

presence of an HDAC inhibitor, they can also perform inhibitor assays by the probe. Thus, their prob may be valuable to the field of epigenetics and drug discovery.

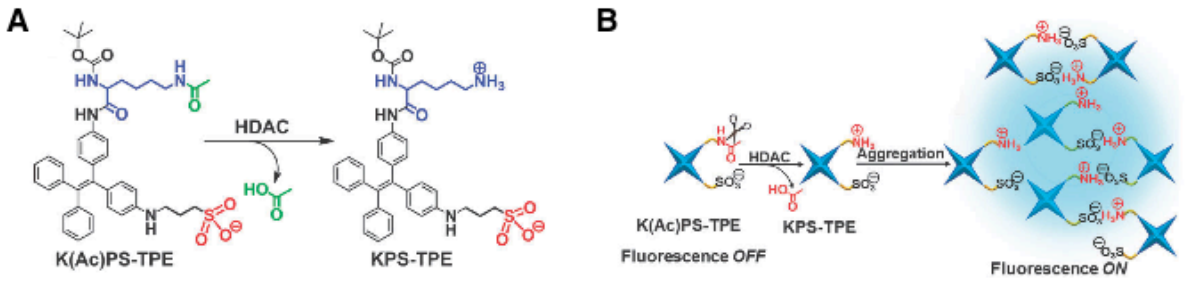

Figure 3. (**A**) Enzymatic deacetylation of K(Ac)PS-TPE to form KPS-TPE with HDAC. (**B**) Schematic representation of the aggregation-induced fluorescence enhancement of K(Ac)PS-TPE by HDAC reaction.

Fluorescence Imaging

Fluorescence imaging is a powerful tool for visualizing biomolecules in a real-time manner with high spatial resolution. To achieve the selective imaging, switching of fluorescence in response to a reaction or binding of target molecule is needed.[8]

Exploitation of AIE described above is one of the promising strategies for the development of Turn-ON fluorescence imaging probes. Liu et al. reported the caspase-3/-7 probe via conjugation of a hydrophilic DEVD peptide sequence and a hydrophobic AIE fluorogen (Ac-DEVDK-TPE, Figure 4A).[9] The probe is soluble in water and nonfluorescent. The specific cleavage of DEVD by caspase-3/-7 induces aggregation of the hydrophobic AIE residues and then the fluorescence turns on. This probe is capable of detecting caspase-3/-7 activities even in living cells (Figure 4B), and useful for real-time apoptosis imaging and in situ apoptosis-related drug screening.

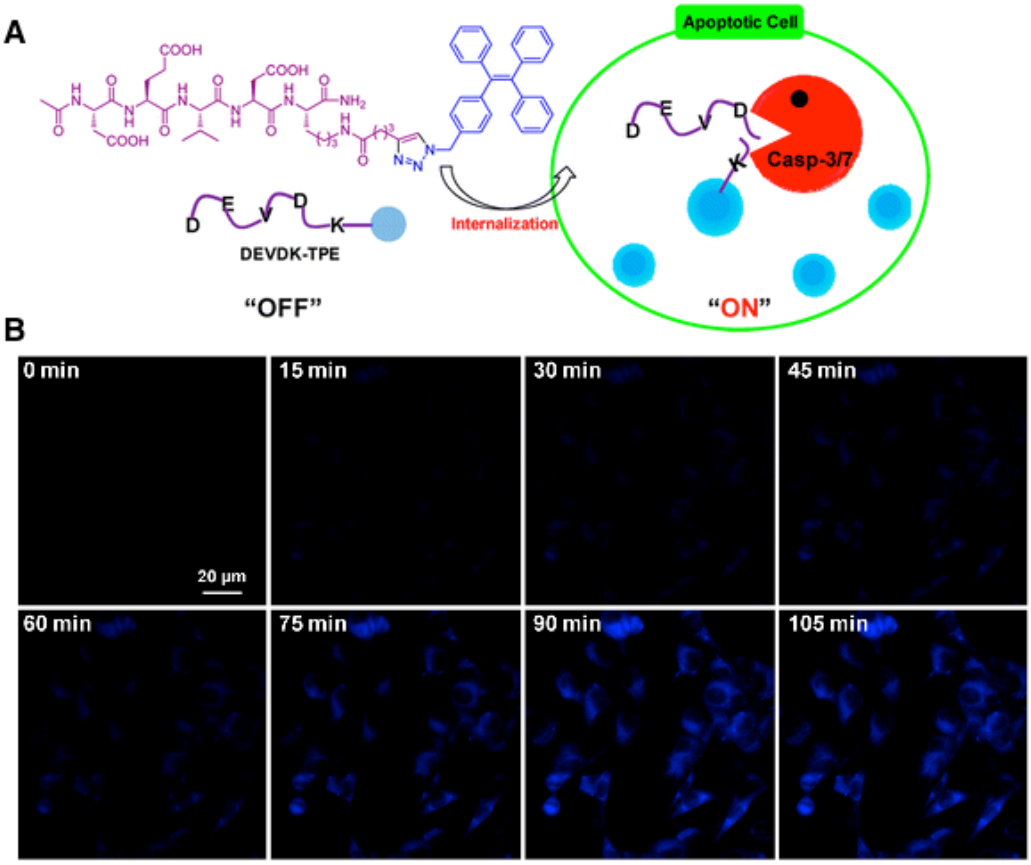

Figure 4. (**A**) Schematic illustration of monitoring of cell apoptosis by AIE-based caspase probe. (**B**) Real-time fluorescence images showing staurosporine-induced apoptotic process of MCF-7 cells with Ac-DEVDK-TPE.

Contrary to AIE, many fluorescence dyes shows quenched fluorescence in the self-assembled state. Hamachi et al reported Turn-ON fluorescence probes for protein detection by using fluorescence quenching in the self-assembled state and fluorescence enhancement after disassembly.[10] Amphiphilic molecules containing hydrophobic fluorescence dye and hydrophilic protein ligand assemble into the nanosphere in water. In the self-assembled state, the fluorescence of the dye was significantly quenched. In contrast, in the presence of target protein, the probe disassembles to enhance the drastic fluorescence change (Figure 5A). Furthermore, they extend this strategy for the cell-surface protein imaging by converting fluorophores to the more hydrophilic

ones such as fluorescein or rhodamine.[11] In this case, by introducing a hydrophobic module near the fluorophore, a new disassembly-driven turn-on nanoprobe was developed. They succeeded in imaging cancer-specific biomarkers such as the folate receptor (FR) and transmembrane-type carbonic anhydrases (CAs) under live cell conditions (Figure 5B). Furthermore, a cell-based inhibitor screening system for CAs under hypoxic live cell conditions was successfully demonstrated. An advantage of the probe is that the strategy can be applied to detection of the non-enzymatic proteins.

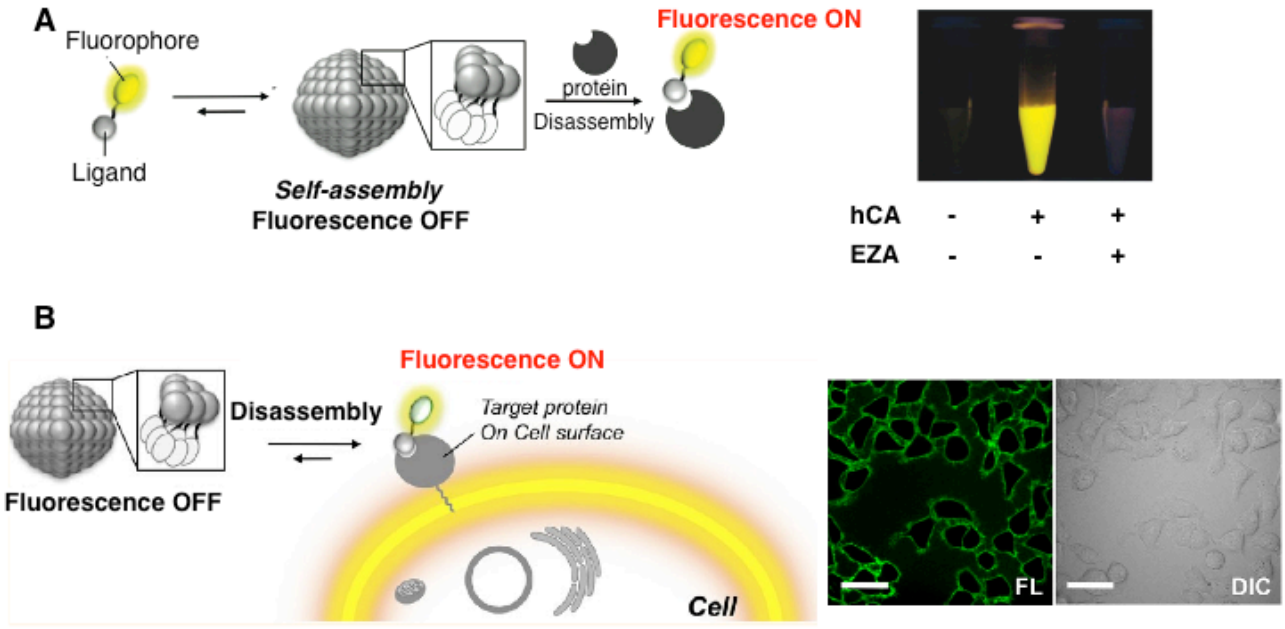

Figure 5. (**A**) Specific protein detection with disassembly-driven Turn-On fluorescent probes. (**B**) Cell-surface protein imaging with disassembly-driven Turn-On fluorescent probes.

MRI Imaging

Magnetic resonance imaging (MRI) is a promising technique for the visualization of biomolecules because of the noninvasive manner and utility for the deep tissue. The most widely used one is ^{1}H-MRI. However, ^{1}H-MRI has the limitation derived from low contrast-to-noise ratio because of the large background signals from water protons. By contrast, because ^{19}F-MRI is highly

sensitive and fluoride-containing molecules are not found in animal body, it has been paid much attention. Hamachi et al. reported aunique strategy to detect specific proteins with Turn-ON type signal change in ^{19}F NMR spectroscopy using dynamic self-assembled nanoparticles (Figure 6A). The basis of the idea is that the ^{19}F NMR signal is broadened and attenuated in the self-assembled state, but sharpens and recovers on their disassembly upon recognition by proteins (Figure 6B). As the signal response is derived from specific protein–ligand interactions, this strategy is applicable to the detection of both enzymes and non-enzymatic proteins.

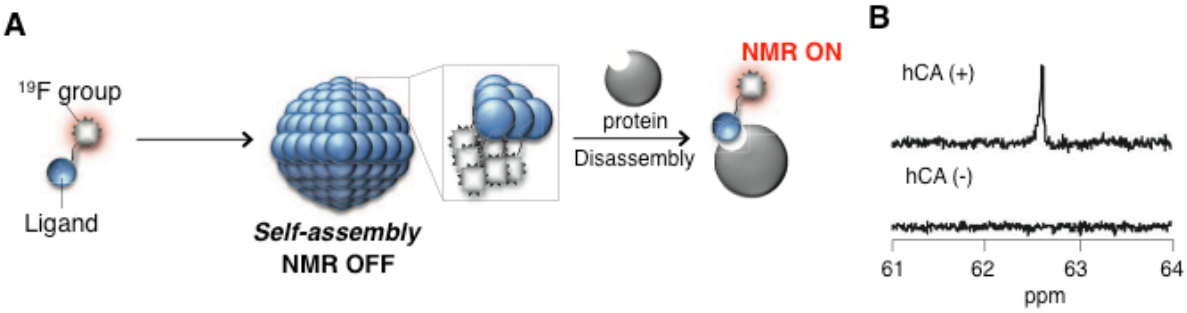

Figure 6. (**A**) Schematic representation of the specific protein detection with disassembly-driven Turn-On ^{19}F NMR probes. (**B**) Turn-On ^{19}F NMR signal of disassembly-driven Turn-On ^{19}F NMR probe in the presence or absence of human carbonic anhydrase (hCA).

Controlled Release

Controlled drug release has gained much attention because of the enhanced efficacy and economical standpoint. Supramolecular nanostructure can entrap drugs in the hydrophobic space. The entrapment is effective for protecting from the nonspecific enzymatic degradation and avoiding undesired side-effect. The stimuli-responsive properties of the nanostructures are suitable to create a functional career for controlled release.

Thayumanavan et al. reported that dendritic amphiphilic nano-containers can be disassembled

in stimuli-responsive manner.[13] As shown in Figure 7A, the nanostructure formed by biotin-incorporated dendrimer disassembled upon the addition of the avidin through ligand-receptor interaction due to the change of the hydrophilic-lipophilic balance.[13a] Consequently, the guest molecules are released (Figure 7B). By altering the structure of amphiphile, they created the nano-container responsive to other stimuli such as photo-irradiation and enzymatic cleavage. [13b, c]

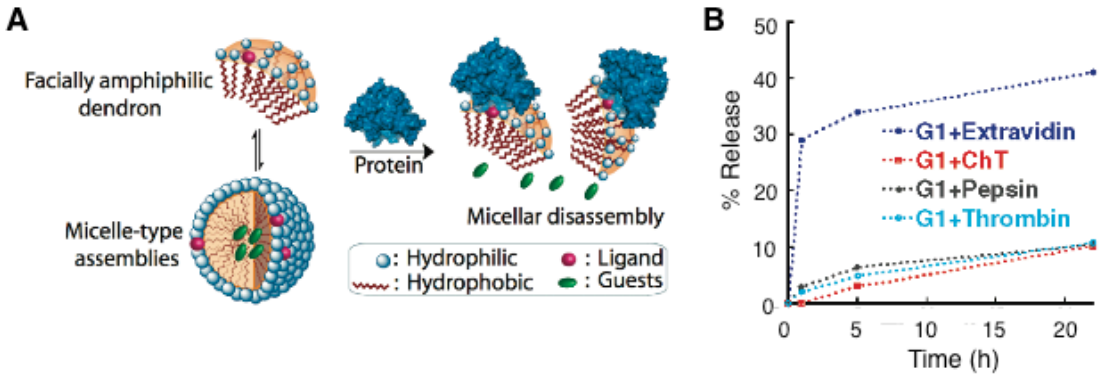

Figure 7. (**A**) Schematic illustration of protein-ligand binding-induced disassembly of dendritic micellar assemblies and resultant guest release. (**B**) Protein-induced release of the guest molecules from the dendritic micellar nano-containers.

Several researchers have reported covalent modifications of drugs to form nanostructures for controlled release. Cui et al. reported peptide nanofiber modified with anticancer drug such as camptothecin and taxol (Figure 8).[14] The disulfide linker of the drug-peptide conjugate cleaves in the presence of glutathione, a reducing agent that exist with high concentration in cytosol. This strategy has the strong advantage for high drug loading compared to the non-covalent encapsulation. Xu et al reported that the drug containing gelator shows unexpected isozyme selectivity. The conjugation of $_D$-amino acids to naproxen, a nonsteroidal anti-inflammatory drug, afforded the supramolecular hydrogel. In addition, the obtained molecule showed high selectivity toward cyclooxygenase-2 (COX-2) than COX-1.[15]

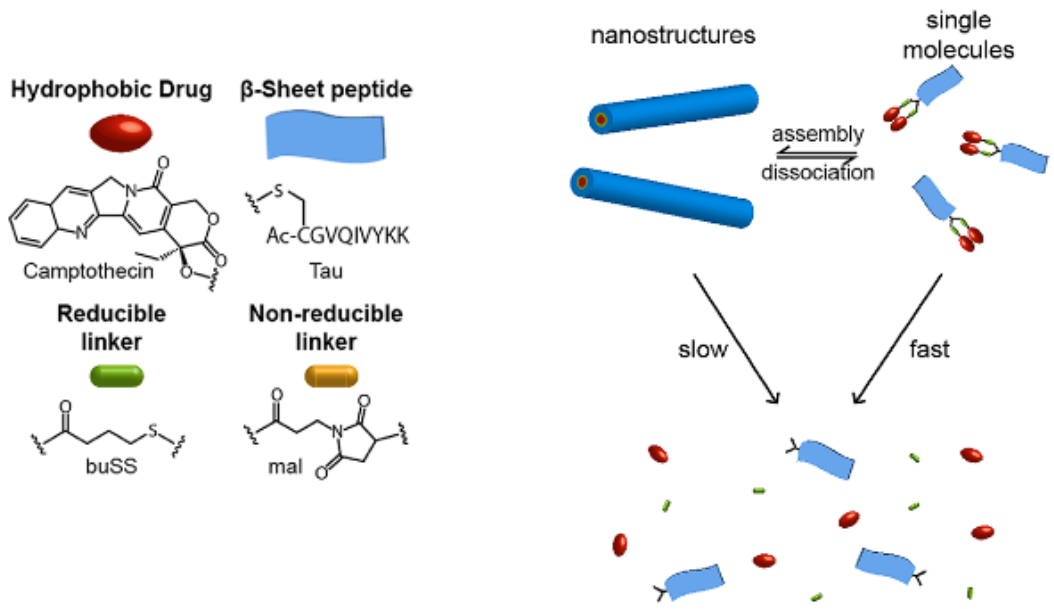

Figure 8. Schematic illustration of the degradation of the Drug Amphiphile (DA).

Cell Culture

Supramolecular hydrogels formed by the assembly of small molecule are utilized for the 3D-cell culture because the fibrous nanostructure is similar to the extracellular matrix such as collagen.[16] Furthermore, unique functions such as stimuli-responsiveness and selective recognition of the protein can be installed to the gel by precise design in single molecular level.

Ulijin et al. developed an anchorage-dependent cell culture scaffold by Fmoc-FF (F: pheynylalanine) and Fmoc-RGD co-assembled supramolecular hydrogel (Figure 9).[17] They confirmed the adherent of the human dermal fibroblast cell in three-dimensional (3D) manner by using a live/dead assay, F-actin staining, and a proliferation/viability assay. The binding of integrin to the RGD ligands was determined using an integrin blocking antibody. Gels containing RGE, a chemical analogue of RGD, do not promote cell adhesion. These results suggest that cell adhesion to the gel is driven by integrin binding to the RGD peptide.

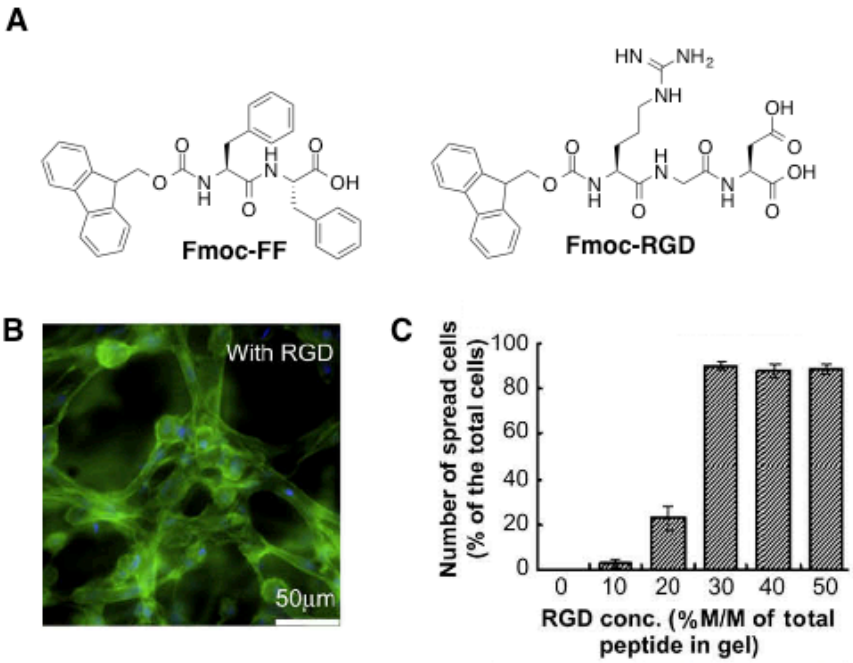

Figure 9. (**A**) Chemical structures of the Fmoc-FF and Fmoc-RGD. (**B**) Cell adhesion and morphology in the Fmoc-FF/RGD gel. (**C**) Spreading cell ratio in various Fmoc-RGD concentrations.

Lee et al. developed a thermo-responsive supramolecular hydrogel, which can be utilized for catching and releasing of cells.[18] The molecules composed of penta-*p*-phenylene unit and dendritic oligoethylene glycol self-assembled to form supramolecular hydrogel (Figure 10 A, B). The supramolecular hydrogel responds to temperature by transforming into a fluid solution upon cooling. Thus, the nanofiber solution can be mixed with cells at room temperature and then can be transformed into gels to encapsulate the cells in a three-dimensional environment upon being heated to physiological temperatures. They found that encapsulation of the cells in three-dimensional networks did not compromise the cell viability, and that subsequent cooling triggers the encapsulated cells to be released through a gel–sol transition (Figure 10 C, D).

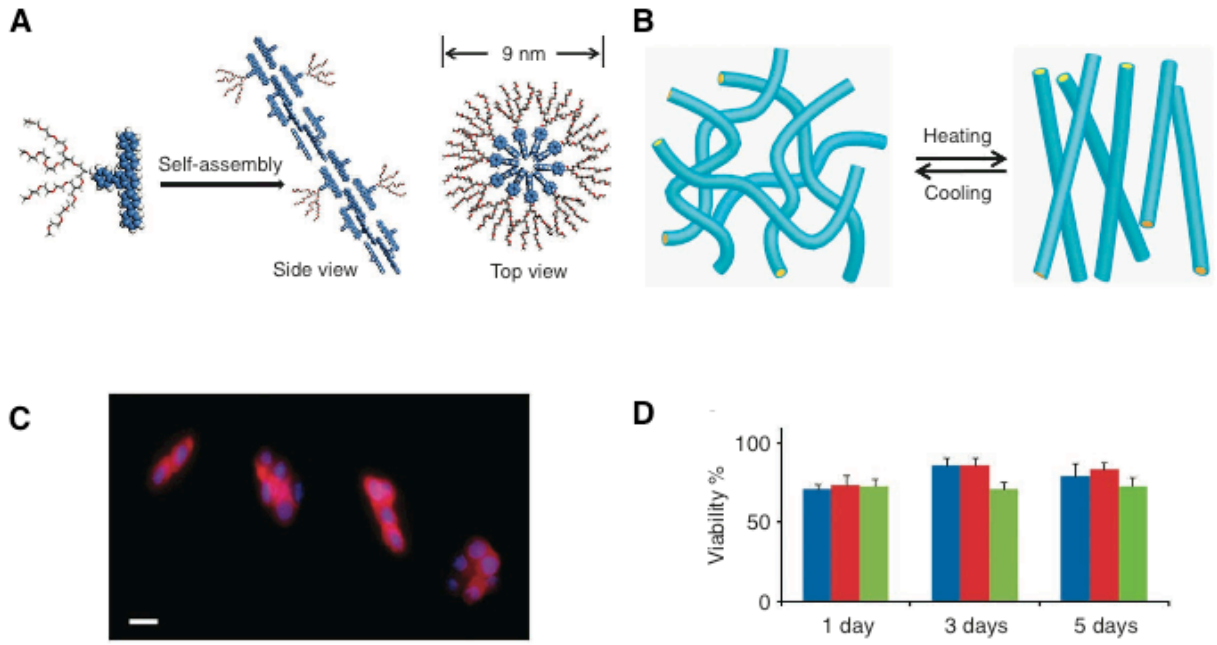

Figure 10. (**A**) Schematic illustration of the molecular arrangements of the nanofibers. (**B**) Schematic illustration of a reversible isotropic sol–gel phase transition of supramolecular nanofibers. (**C**) Fluorescent image of a stained cell after release from the gel. (**D**) The viability test of C2C12 cells grown in nanofiber gels (1 wt% (blue), 1.5 wt% (red) and 2 wt% (green)) for 5 days.

Cell Differentiation

Cell differentiation can also be controlled by the self-assembled nanofiber. Cells respond to both chemical substances and mechanical properties of surrounding environment. Therefore, dynamic control of extracellular environment leads to the cellular differentiation.[19]

As a pioneering work, Stupp et al. reported that the epitope (IKVAV) containing amphiphile self-assembles into nanofiber, which induced very rapid differentiation of neural progenitor cells into neurons compared with laminin or soluble peptide (Figure 11A).[20] The result suggests the importance of the high density of bioactive epitope presented to cells for the observed rapid and selective differentiation.

Zhang et al reported a utility of bio-orthogonal photoclick reaction to modulate the properties

of supramolecular hydrogel and cellular phenotype (Figure 11B).[21] Using biaryl-substituted tetrazole to modify short peptides gives supramolecular hydrogelators Tet(I)-GFF and Tet(II)-GFRGD that self-assemble to form hydrogels. The rapid intramolecular photoclick reaction of the tetrazole moiety turns on fluorescence and then gradually disturbs the self-assembly of the hydrogelator to induce photodegradation of the hydrogel. They demonstrated the photo-modulation of the microenvironment of C2C12 cells cultured on the gel surface or hMSCs encapsulated inside the gel.

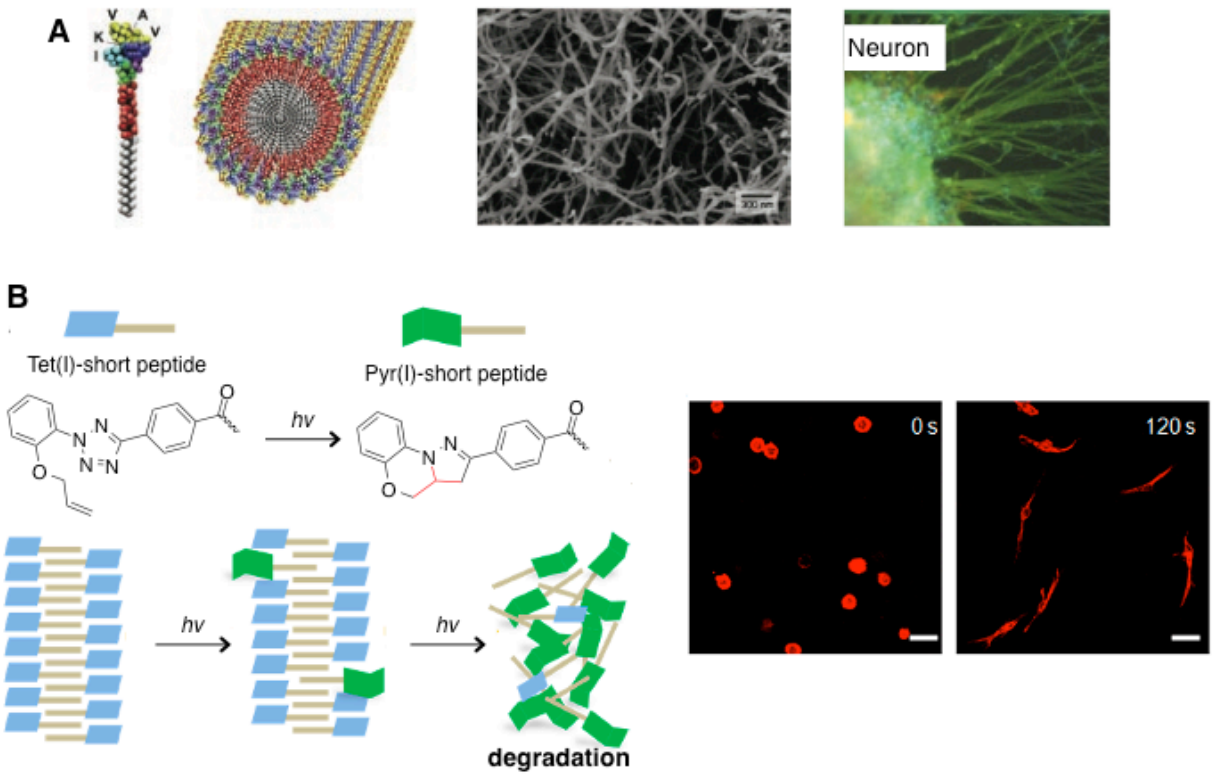

Figure 11. (**A**) Selective differentiation of neural progenitor cells by high-epitope density nanofibers formed by IKVAV-containing peptide amphiphile. (**B**) Photodegradable supramolecular hydrogel and control of cellular differentiation.

Bacterial Inhibition

Bacterial strains have developed resistance toward conventional antibiotics as a consequence of evolution, which has been considered as a social problem. Recently, antimicrobial peptides capable of targeting a wide range of "multidrug-resistant" strains have been paid much attention. [22] However, potential therapeutic applications of these peptides have suffered from several problems such as selectivity, toxicity, and bioavailability. Various approaches have been adopted to mimic the function of natural antimicrobial peptides.[23] Schneider et al. reported that self-assembled nanofiber formed by arginine-rich self-assembling peptides were effective at killing both gram-positive and gram-negative bacteria, including multi-drug resistant *Pseudomonas aeruginosa* (Figure 13A, B).[24] Although the hydrogel is toxic for bacterium, it is compatible toward the mammalian cells. Moreover, the hydrogel is stiff and displays shear-thin recovery behavior, which allows its delivery to wounds via simple injection.

Intracellular enzymatic formation of supramolecular nanostructures can also control the fate of bacterial cells. Xu et al. reported that enzymatic hydrolysis of hydrogel precursor containing phosphate group induced the formation of nanofibers in *E. Coli.* (BL21) overexpressing phosphatase (Figure 13C).[25] The formation of the nanofiber results in the inhibition of *E. Coli.*. The result suggests a new antibacterial therapeutic strategy by the virtue of supramolecular chemistry.

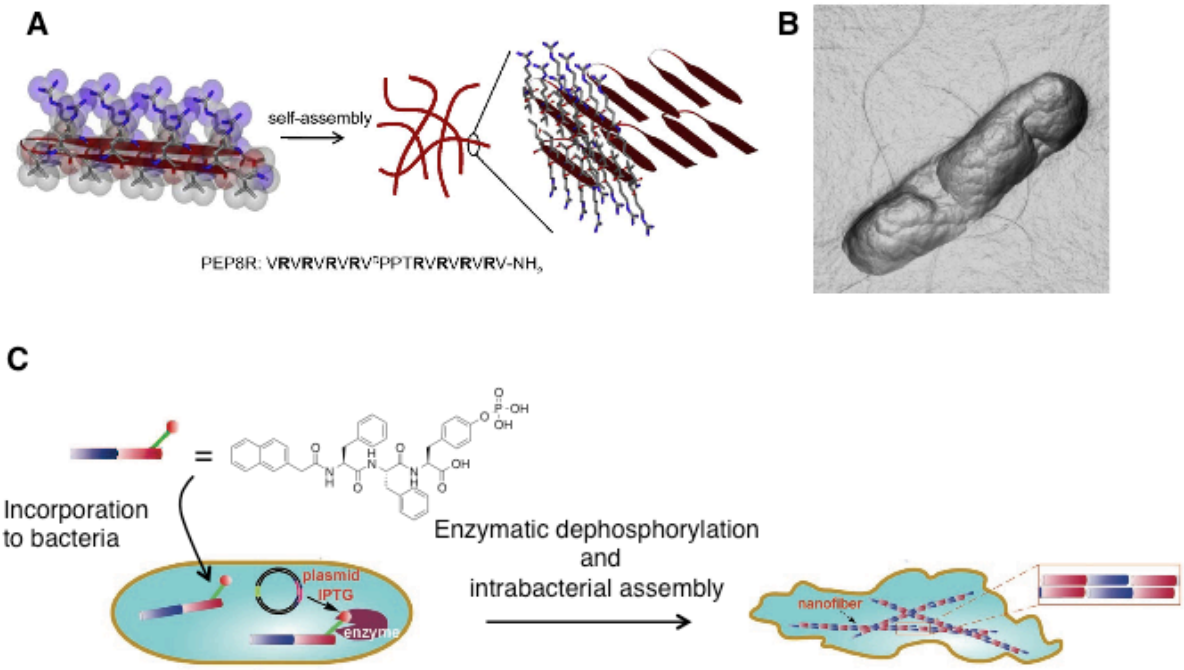

Figure 13. (**A**) Self-assembly of PEP8R peptide and formation of hairpin β-sheet rich fibrils. (**B**) Three-dimensional orthogonal projection images (derived from AFM height data) of *E. coli* cells on 2 wt% hydrogel surface. (**C**) Schematic representation of intracellular nanofiber formation and inhibition of bacterial growth

Anticancer Effect

Xu et al. reported the formation of nanofibers inside living cells caused the anticancer effect (Figure 14A).[26] A peptide gelator (Nap-FF) forms nanofiber in glioblastoma cells and disrupt the dynamics of microtubules, which consequently induces apoptosis. On the contrary, Nap-FF does show neither the nanofiber formation nor toxicity in neuronal cell. They speculated that the selectivity of the toxicity is derived from the tendency of small molecules to accumulate in cells. They also reported the enzymatic formation of nanofibers of a small $_D$-peptide derivative in pericellular space to show the anticancer activities (Figure 14B).[27] Surface and secretory phosphatases dephosphorylate a precursor of a hydrogelator to trigger the self-assembly of the

hydrogelator and to result in pericellular nanonets selectively around the cancer cells that overexpress phosphatases. Cell-based assays confirm that the pericellular nanofibers block cellular mass exchange to induce apoptosis of cancer cells, including multidrug-resistance cancer cells, MES-SA/Dx5. The formation of pericellular nanofibers of small molecules to exhibit distinct functions illustrates a fundamentally new way to engineer molecular assemblies spatiotemporally in cellular microenvironment for inhibiting cancer cell growth and even metastasis.

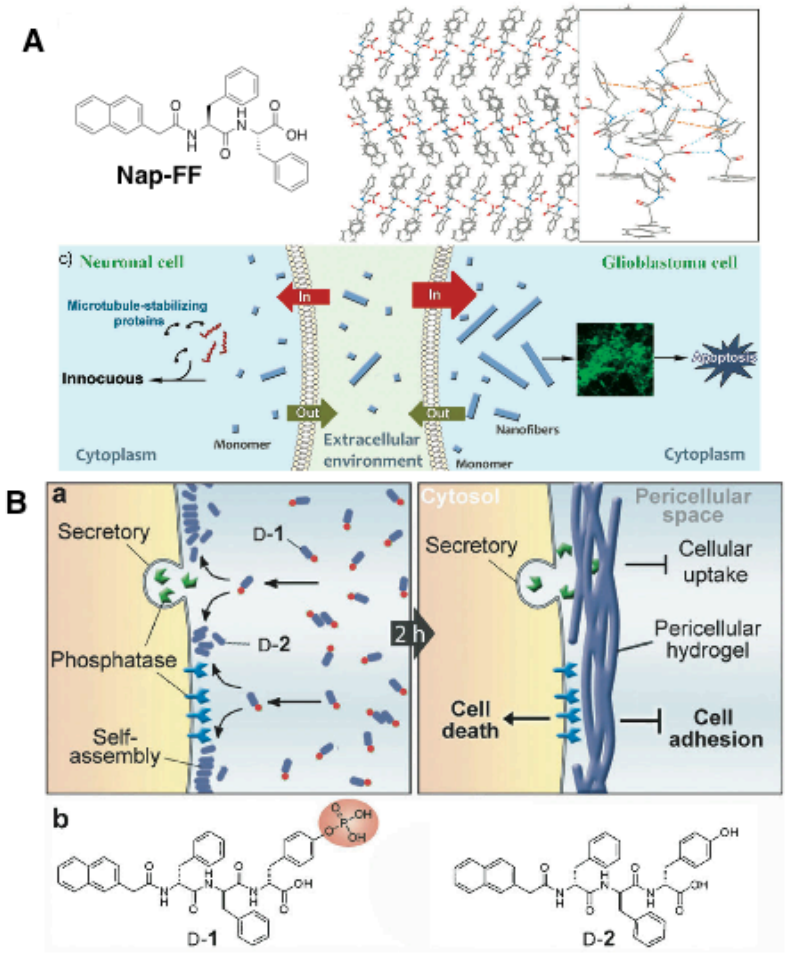

Figure 14. (**A**) Selective inhibition of glioblastoma cells by nanofibers of small hydrophobic molecules. (**B**) Enzyme-catalyzed formation of pericellular hydrogel/nano- nets to induce cell death.

Controlling Protein Activities

Proteins play pivotal roles in biological system. Therefore, controlling of protein activities is important for drug discovery or protein engineering. Recently, several researchers reported that functions of some proteins can be regulated using the self-assembled nanostructures.

Shoichet et al. reported that the colloidal aggregate of the small molecular drug has unusual properties for the nonspecific protein inhibition (Figure 15A).[28] They confirmed a mechanism for the nonspecific inhibition by hydrogen-deuterium exchange mass spectrometry (HDX-MS) and trypsin digestion experiment. In the presence of the colloidal aggregate, protein contained higher deuterium content than that in the absence of the aggregate. Moreover, the proteins were more susceptible to proteolytic degradation. From these results, they suggest that the mechanism of the protein inhibition by the colloidal aggregate is partially ascribed to unfolding of the protein upon binding.

Contrary to the Shoichet's work, Wells and co-worker found a nano-assembled enzyme activator (Figure 15B).[29] From high-throughput screening, they identified a compound, called 1541, which activate caspase-3. Interestingly, the activator 1541 self-assembles in water to form nanofibers with 2.6 nm in width and more than 1 μm in length. The self-assembly of 1541 is essential for activation of caspase-3. Although the mechanism of the activation has yet to be fully resolved, their finding suggests a new insight into the drug-discovery.

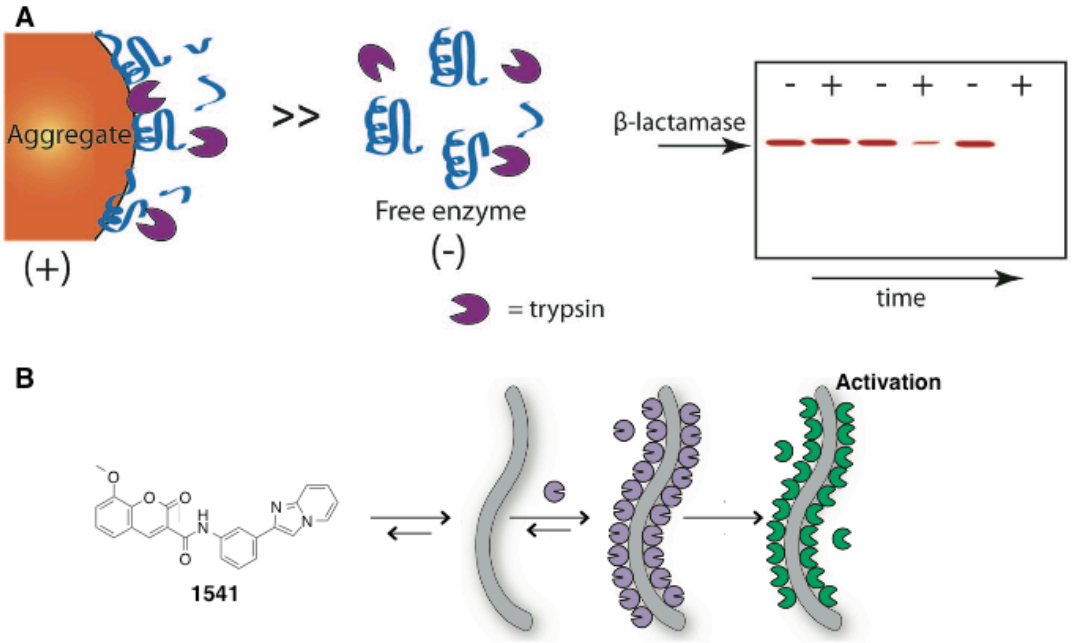

Figure 15. (**A**) Schematic representation of the promiscuous protein inhibition of small-molecule aggregators. (**B**) Schematic representation of the activation of caspace-3 by self-assembled nanofiber.

Summary of this thesis

As described above, many efforts have been devoted to develop functional biomaterials for detection/imaging of the biomolecules or controlling of biological systems by using the unique functions of self-assembled nanostructures. Precise control of the nanostructure dynamics leads to the development of novel functional biomaterials.

In this thesis, I successfully constructed the functional self-assembled nanostructure useful for biological application such as biomolecular sensing (chapter 1), controlling materials motion (chapter 2), and live-cell imaging (chapter 3). This thesis consists of three chapters, which are summarized as follows:

In chapter 1, I describe the development of fluorocolorimetric sensor for polyamines such as spermine and spermidine by hybridization of a supramolecular hydrogel with montmorillonite, an inorganic material, adsorbing a fluorescent dye,. The utility of this hybrid sensor system is successfully demonstrated in the naked eye detection of the polyamines in artificial urine.

In chapter 2, I constructed the first two-photon responsive supramolecular hydrogel by incorpolating photo-responsive coumarin group in peptide. The fluidity inside the supramolecular hydrogel was presicely controlled with high spatial resolution (10 μm × 10 μm × 10 μm). I successfully demonstrated the Off-On switching of Brownian motion of nanobeads and bacterial chemotaxis by two-photon excitation.

In chapter 3, I describe the development of disassembly-driven turn on fluorescence nanoprobe for the imaging of endogeneous proteins in living cells. I specifically visualized human carbonic anhydrase and heat shock protein 90 inside living mammalian cells. The reversible assembly/disassembly of the supramolecular probes allowed us to construct an imaging-based

inhibitor assay system in live cells.

Reference

(1) a) Whitesides, G. M.; Grzybowski, B. *Science* **2002**, *295*, 2418–2421. b) Gazit, E. *Chem. Soc. Rev.*, **2007**, *36*, 1263–1269.

(2) a) Zhai, D.; Xu, W.; Zhang, L.; Chang, Y. T. *Chem. Soc. Rev.* **2014**, 43, 2402–2411. B) Ding, D.; Li, K.; Liu B.; Tang, B. Z., *Acc. Chem. Res.*, **2013**, *46*, 2441–2453.

(3) a) Mart, R. J.; Osborne, R. D.; Stevens, M. M.; Ulijn, R. V. *Soft Matter*, **2006**, *2*, 822–835. b) Kim, H.-J.; Kim, T.; Lee, M. *Acc. Chem. Res.*, **2011**, *44*, 72–82.

(4) a) Estroff, L. A.; Hamilton, A. D. *Chem. Rev.* **2004**, *104*, 1201−1217. b) Hirst, A. R.; Escuder, B.; Miravet, J. F.; Smith, D. K. *Angew. Chem., Int. Ed.* **2008**, *47*, 8002–8018.

(5) a) Ikeda, M.; Ochi R.; Hamachi, I. *Lab Chip* **2010**, *10*, 3325−3334. b) Kiyonaka, S.; Sada, K.; Yoshimura, I.; Shinkai, S.; Kato, N.; Hamachi, I. *Nat. Mater.* **2004**, *3*, 58–64. c) Yoshimura, I.; Miyahara, Y.; Kasagi, N.; Yamane, H.; Ojida, A.; Hamachi, I. *J. Am. Chem. Soc.* **2004**, *126*, 12204−12205. d) Tamaru, S.-i.; Kiyonaka S.; Hamachi, I. *Chem.–Eur. J.* **2005**, *11*, 7294–7304. e) Yamaguchi, S.; Yoshimura, T.; Kohira, T.; Tamaru, S.-i.; Hamachi, I. *J. Am. Chem. Soc.* **2005**, *127*, 11835–11841.

(6) Hong, Y.; Lamab, J. W. Y.; Tang, B. Z. *Chem. Soc. Rev.* **2011**, *40*, 5361–5388.

(7) Dhara, K.; Hori, Y.; Baba, R.; Kikuchi, K. *Chem. Commun.,* **2012**, *48*, 11534–11536.

(8) Kobayashi, H.; Ogawa, M.; Alford, R.; Choyke, P. L.; Urano, Y. *Chem. Rev.* **2010**, *110*, 2620–2640.

(9) Shi, H.; Kwok, R. T. K.; Liu, J.; Xing, B.; Tang, B. Z.; Liu. B. *J. Am. Chem. Soc.* **2012**, *134*, 17972−17981.

(10) Mizusawa, K.; Mizusawa, K.; Ishida, Y.; Takaoka, Y.; Miyagawa, M.; Tsukiji, S.; Hamachi, I. *J. Am. Chem. Soc.* **2010**, *132*, 7291–7293.

(11) Mizusawa, K.; Takaoka, Y.; Hamachi, I. *J. Am. Chem. Soc.* **2012**, *134*, 13386–13995.

(12) a) Takaoka, Y.; Sakamoto, T.; Tsukiji, S.; Narazaki, M.; Matsuda, T.; Tochio, H.; Shirakawa, M.; Hamachi, I. *Nat. Chem.* **2009**, *1*, 557–561. b) Takaoka, Y.; Kiminami, K.; Mizusawa, K.; Matsuo, K.; Narazaki, M.; Matsuda, T.; Hamachi, I. *J. Am. Chem. Soc.* **2011**, *133*, 11725–11731.

(13) a) Azagarsamy, M. A.; Yesilyurt, V.; Thayumanavan, S. *J. Am. Chem. Soc.* **2010**, *132*, 4550–4551. b) Azagarsamy, M. A.; Sokkalingam, P.; Thayumanavan, S. *J. Am. Chem. Soc.* **2009**, *131*, 14184–14185. c) Yesilyurt, V.; Ramireddy, R.; Thayumanavan, S. *Angew. Chem., Int. Ed.* **2011**, *50*, 3038 –3042.

(14) a) Cheetham, A. G.; Zhang, P.; Lin, Y. A. Lock, L. L.; Cui, H. *J. Am. Chem. Soc.* **2013**, *135*, 2907−2910. b) Lin, R.; Cheetham, A. G.; Zhang, P.; Lin, Y. A.; Cui, H. *Chem. Commun.,* **2013**, *49*, 4968–4970. c) Cheetham, A. G.; Ou, Y.; Zhang, P.; Cui H. *Chem. Commun.* **2014**, *50*, 6039–6042.

(15) Li, J.; Kuang, Y.; Gao, Y.; Du, X.; Shi, J.; Xu, B. *J. Am. Chem. Soc.* **2012**, *135*, 542–545.

(16) a) Zhang, S.; Holmes T. C.; , Dipersio G. M.; Hynes, R.O.; Su X.; *Biomaterials* **1995**, *16*, 1385–1393. b) Kretsinger, J. K.; Haines, L. A.; Ozbas, B.; Pochan, D. J.; Schneider, J. P.; *Biomaterials* **2005**, *26*, 5177–5186.

(17) Zhou, M.; Smith, A. M.; Das, K. A.; Hodson, N. W.; Collins, R. F.; Ulijn, R. V.; Gough, J. E. *Biomaterials* **2009**, *30*, 2523–2530.

(18) a) Moon, K.-S.; Kim, H.-J.; Lee, E.; Lee, M. *Angew. Chem., Int. Ed.* **2007**, *46*, 6807–6810. b) Huang, Z.; Lee, H.; Lee, E.; Kang, S.-K.; Nam, J.-M.; Lee, M. *Nat. Commun*. **2011**, *2*, 459, DOI: 10.1038/ ncomms1465.

(19) a) A. Engler, S. Sen, H.L. Sweeney, D. Discher, *Cell*, 2006, 126, 677–689. b) Benoit, D. S. W.; Schwartz, M. P.; Durney, A. R.; Anseth, K. S. *Nat. Mater.* **2008**, *7*, 816–823. c) Lutolf, M. P.; Hubbell, J. A. *Nat. Biotechnol*. **2005**, *23*, 47–55.

(20) Silva, G. A.; Czeisler, C.; Niece, K. L.; Beniash, E.; Harrington, D. A.; Kessler, J. A.; Stupp, S. I. *Science* **2004**, *303*, 1352–1355.

(21) He, I. M.; Li, J.; Tan, S.; Wang, R.; Zhang, Y. *J. Am. Chem. Soc*. **2013**, *135*, 18718–18721.

(22) a) Zasloff, M. *Nature* **2002**, *415*, 389−395. (b) Brogden, K. A. *Nat. Rev. Microbiol.* **2005**, *3*, 238−250. (c) Hancock, R. E.; Sahl, H. G. *Nat. Biotechnol*. **2006**, *24*, 1551−1557. (d) Boman, H. G. *Cell* **1991**, *65*, 205− 207. (e) Bulet, P.; Stocklin, R.; Menin, L. *Immunol. Rev.* **2004**, *198*, 169−184.

(23) Srinivas, N.; Jetter, P.; Ueberbacher, B. J.; Werneburg, M.; Zerbe, K.; Steinmann, J.; Meijden, B. V.; Bernardini, F.; Lederer, A.; Dias, R. L. A.; Misson, P. E.; Henze, H.; Zumbrunn, J.; Gombert, F. O.;Obrecht,D.;Hunziker,P.;Schauer,S.;Ziegler,U.;Kaĕh,A.;Eberl, L.; Riedel, K.; DeMarco, S. J.;

Robinson, J. A. *Science* **2010**, *327*, 1010−1013. (b) Liu, L.; Xu, K.; Wang, H.; Tan, P. K. J.; Fan, W.; Venkatraman, S. S.; Li, L.; Yang, Y. Y. *Nat. Nanotechnol.* **2009**, *4*, 457−463.

(24) Veiga, A. S.; Sinthuvanich, C.; Gaspar, D.; Franquelim, H. G.; Castanho, A. R. B. M.; Schneider, J. P. *Biomaterials* **2012**, 33, 8907–8916.

(25) Yang, Z.; Liang, G.; Guo, Z.; Guo, Z.; Xu, B. *Angew. Chem., Int. Ed.* **2007**, *46*, 8216–8219.

(26) Kuang, Y.; Xu, B. *Angew. Chem., Int. Ed.* **2013**, *52*, 6944–6948.

(27) Kuang, Y.; Shi, J.; Li, J.; Dan Yuan, Alberti, K. A.; Xu, Q.; Xu, B. *Angew. Chem., Int. Ed. Early View,* DOI: 10.1002/anie.201402216

(28) a) Coan, K. E.; Maltby, D. A.; Burlingame, A. L.; Shoichet, B. K. *J. Med. Chem.* **2009**, *52*, 2067−2075. (b) Owen, S. C.; Doak, A. K.; Wassam, P.; Shoichet, S. M.; Shoichet, B. K. *ACS Chem. Biol.* **2012**, *7*, 1429–1435. (c) Sassano, M. F.; Doak, A. K.; Roth, B. L.; Shoichet, B. K. *J. Med. Chem.* **2013**, *56*, 2406–2414.

(29) a) Wolan, D. W.; Zorn, J. A.; Gray, D. C.; Wells, J. A. *Science* **2009**, *326*, 853–858. b) Zorn, J. A.; Wille, H.; Wolan, D. W.; Wells, J. A. *J. Am. Chem. Soc.* **2011**, *133*, 19630–19633. c) Zorn, J. A.; Wolan, D. W.; Agard, N. J.; Wells, J. A. *J. Biol. Chem.* **2012**, *287*, 33781–33795.

Chapter 1

Montmorillonite-Supramolecular Hydrogel Hybrid for Fluorocolorimetric Sensing of Polyamines

Abstract

Fluorescent sensor materials for rapidly and conveniently detecting polyamines in biological fluids are highly desirable for cancer diagnosis. I herein describe the hybridization of a supramolecular hydrogel with a layered inorganic host adsorbing a fluorescent dye, which produces a fluorocolorimetric sensor for biologically important polyamines such as spermine and spermidine. The utility of this hybrid sensor system is successfully demonstrated in the naked eye detection of the polyamines in complex biological fluids.

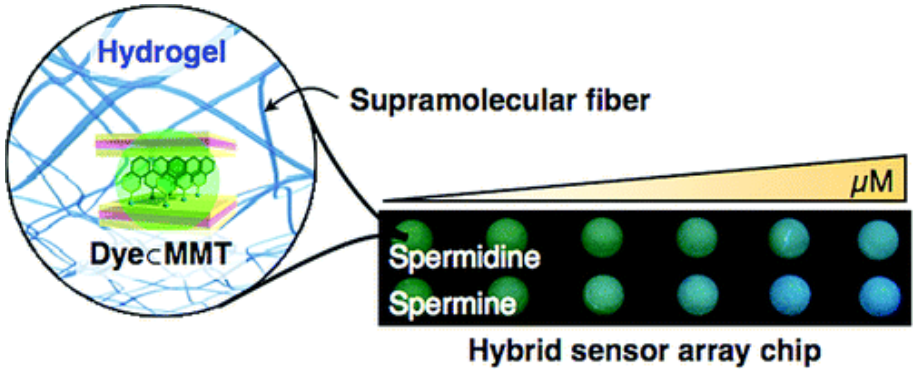

1-1. Introduction

Polyamines, such as spermine and spermidine, are known to play an important role in cell growth and proliferation and thus are expected to be good biomarkers for abnormally and rapidly growing cancers.[1] For example, it is reported that determination of urinary polyamine concentrations can be used for assessing the effectiveness of cancer chemotherapy.[2] Although these polyamines are currently detected using immunoassays[1b] and chromatographic techniques,[1c,2a] these are time-consuming tedious procedures involving expensive equipments. Convenient diagnostic tools capable of sensing such biomarkers in a rapid, label-free, and high-throughput manner are highly desirable.[3,4] Tsubaki *et al* reported the polyamine chemosensor based on the phenolphthalein and two crown loops (Figure 1). Unfortunately this chemosensor works only in the organic solvent such as methanol. In addition, the fluorescence response of their chemosensor is On-Off manner (Off-On-type sensor is more desirable). Swager *et al.* developed a flouorocolorimetric polyamine sensor by using a conjugated polyelectrolyte (CPE, Figure 2). The fluorescence-response of the CPE-based sensor relies on nonspecific electrostatic interactions, which is susceptible to interference from multiply charged species, such as proteins and multivalent cations, commonly found in complex biological fluids.

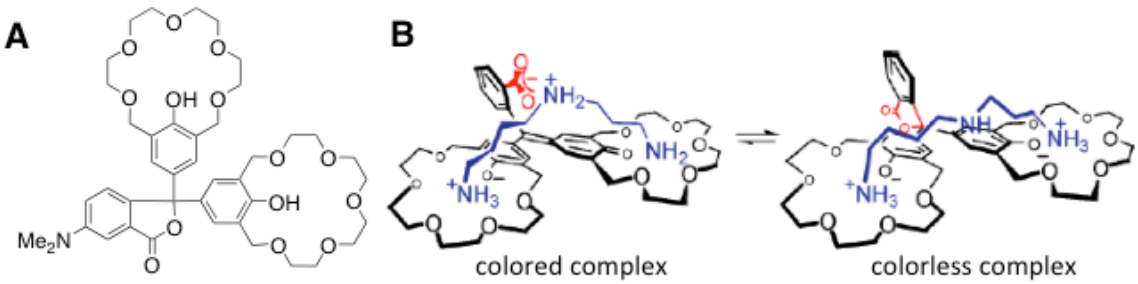

Figure 1. (**A**) Chemical structure of phenolphthalein-based polyamine sensor. (**B**) Equilibrium between colored and colorless complexes.

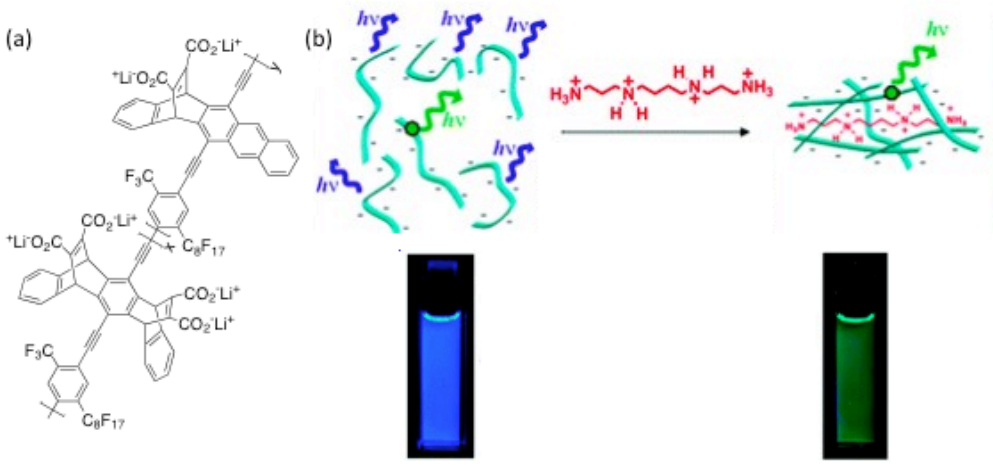

Figure 2. (**A**) Chemical structure of CPE-based polyamine sensor. (**B**) Schematic illustration of the spermine-induced aggregation of the anionic CPE and the accompanying blue-to-green fluorescence color change.

Previously our group developed semiwet fluorescent sensor materials by hybridization of a supramolecular hydrogel with an nanoporous inorganic host encapsulating a fluorescent dye as a probe (Figure 3).[5c] In this gel-based sensor, an anionic fluorescent dye (**Cou-pSer**) is encapsulated into a cationic mesoporous silica for detecting *polyanions*. It was demonstrated that the supramolecular hydrogel not only serves as an immobilization matrix, but also plays an active role in converting signals of the fluorescent dye. Since the self-assembled fibers in the supramolecular hydrogel provide continuous hydrophobic nano-spaces, the fluorescent dye bearing a hydrophobic part can be entrapped inside the fibers upon being released from the host through a selective exchange with the target (guest) substances, which causes fluorescence spectral changes. Thus, the fluorescent dye acts as a probe for following the exchange phenomena.

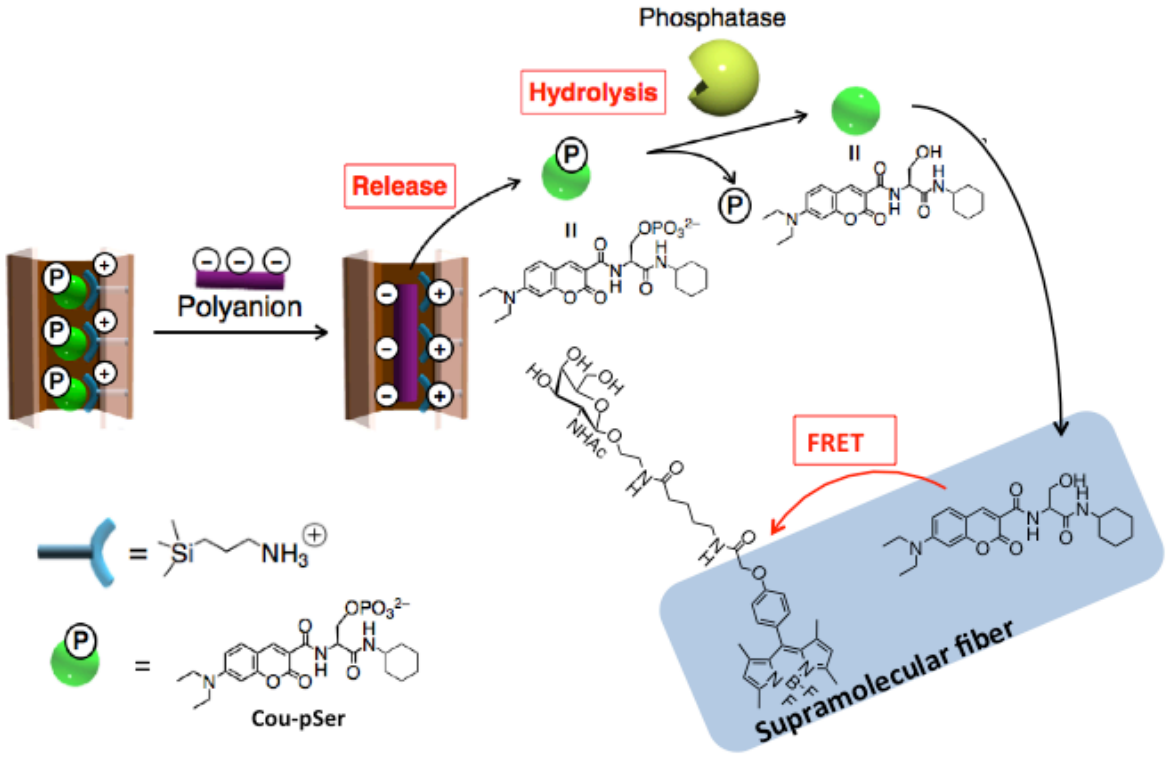

Figure 3. Construction and mechanism operating in fluorescent dye encapsulated MCM-Enzyme-Supramolecular hydrogel hybrid sensory system for polyanions.

I herein successfully expanded this strategy toward sensing *polycations* using a naturally abundant anionic layered material, montmorillonite[6] (MMT), as the host and a cationic fluorescent dye as the probe which both are embedded in supramolecular hydrogel **1**[7] (Figure 4). In the present system, it was crucial that the surface of the MMT nanosheet had high anionic charge density to facilitate aggregation of the cationic fluorescent probe (G-Coum).[8] The adsorbed cationic probe showed a weak greenish, excimer emission, which converted to an intensified blue, monomer emission through its release via the cation-exchange and the subsequent translocation to the supramolecular fibers **1**. This gave rise to a unique fluorocolorimetric readout mechanism, different from the previous systems.[5] I also demonstrated that an array using the miniaturized hybrid sensor is promising for user-friendly naked eye detection of spermine and spermidine in artificial urine.

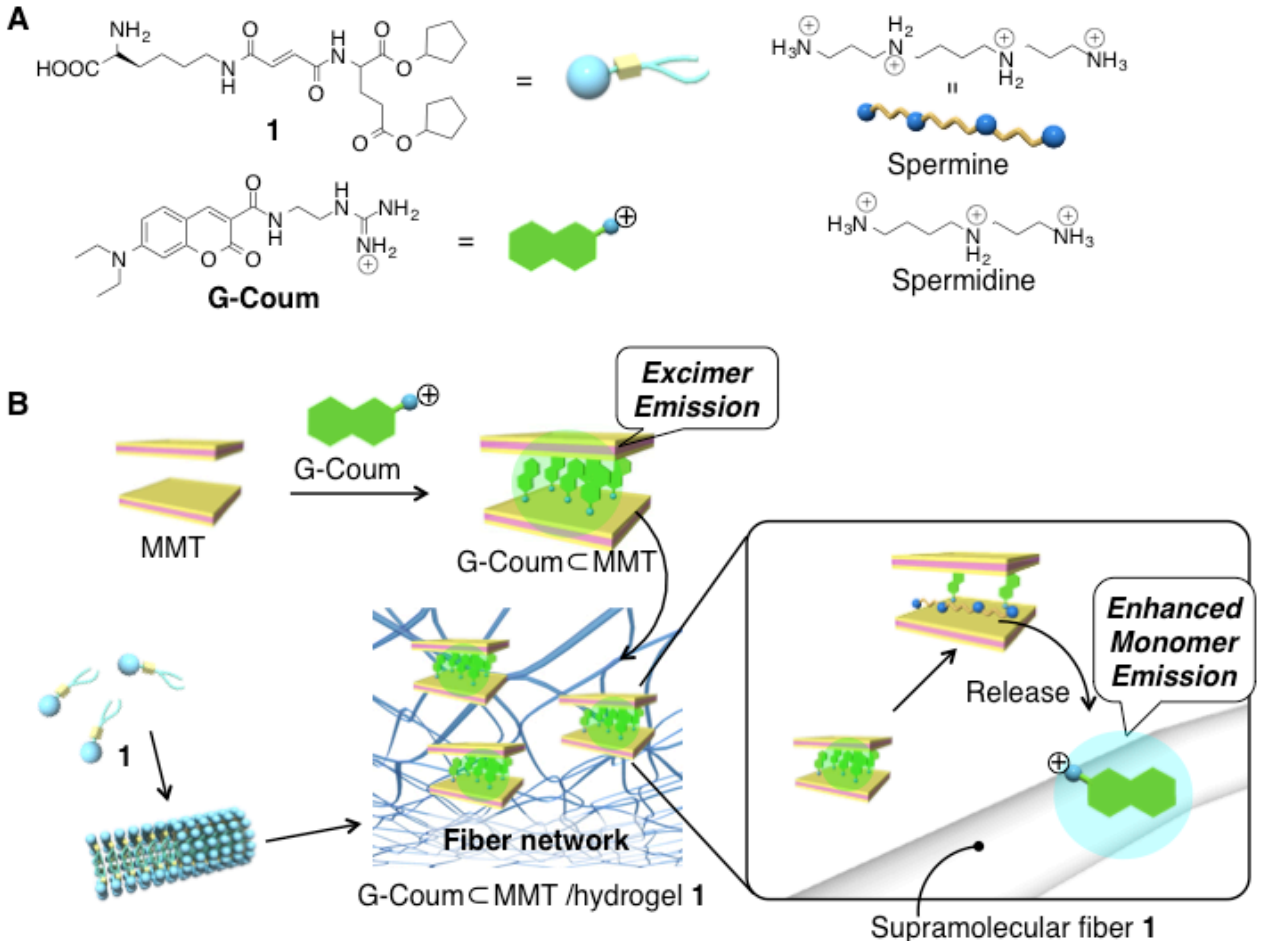

Figure 4. (A) Chemical structures of hydrogelator **1**, G-coum, and polyamines **(B)** construction and the mechanism of action of the fluorescence dye (G-coum) adsorbed MMT/supramolecular hydrogel **1** hybrid sensory system for polyamines.

1-2. Result and Discussion

1-2-1. Adsorption and Cation exchange of MMT

The catch and release function of MMT for cationic substances was first investigated as an aqueous suspension system. Adsorption of three cationic fluorescent dyes (G-coum, G-Dansyl, and G-NBD, Figure 4A, 5A) bearing a guanidium group to MMT occurred almost quantitatively by mixing the dyes and MMT in neutral aqueous media (Figure 5B). The adsorbed G-coum and G-Dansyl to MMT (G-coum⊂MMT) were released by the addition of spermine (32% and 20%, respectively) but not by propylamine (1.5% and 4.2%, respectively). In contrast, the spermine-induced release was not observed in the case of the G-NBD. Since G-coum showed the largest difference in release ratio between the addition of spermine and propylamine, I used G-coum for further study. Release efficiency did not show strong dependency on % loading (in a range of 4–19% loading against CEC of MMT (1.19 μmol/mg)) (Figure 6B). As summarized in Figure 7, it was clear that the release was efficiently induced by polyamines such as spermine and spermidine and several diamines,[10] but not by propylamine (monoamine), urea, or ATP (adenosine triphosphate), indicating that substances having more than two positive charges can facilitate the cation-exchange reaction of G-coum with MMT.

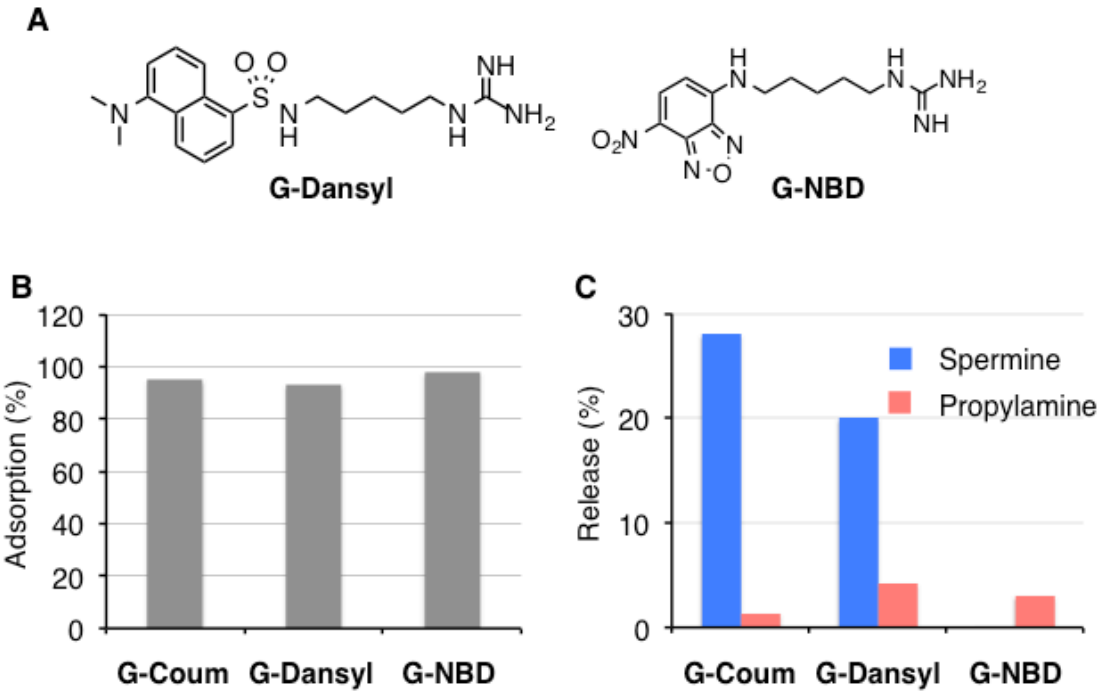

Figure 5. (**A**) Chemical structures of G-NBD and G-Dansyl. (**B**) Adsorption efficiency (%) of cationic fluorescent dyes to MMT evaluated from the absorption spectra of the supernatants. (**C**) Release efficiency (%) of fluorescent dyes from MMT induced by spermine and propylamine evaluated from the absorption spectra of the supernatants. Conditions: [Dye⊂MMT] = 0.5 mg/mL, [Spermine, Propylamine] = 10 mM, 50 mM HEPES (pH 7.4), room temperature.

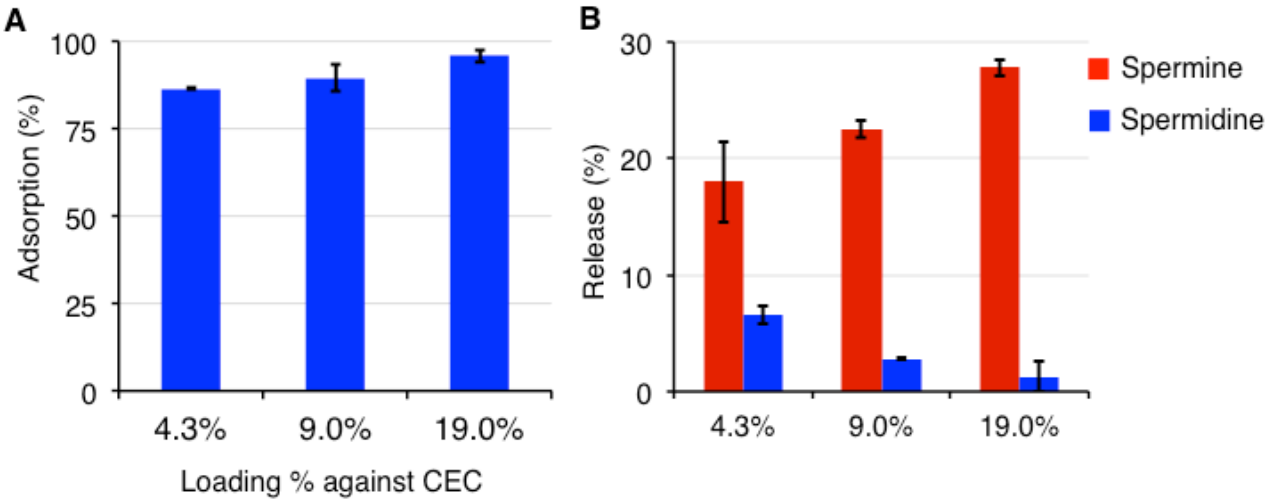

Figure 6. (**A**) Adsorption efficiency (%) of G-coum to MMT evaluated from the absorption spectra of the supernatants. (**B**) Release efficiency (%) of G-coum from MMT induced by spermine and propylamine evaluated from the absorption spectra of the supernatants. Conditions **B**: [G-coum⊂MMT] = 1.0 mg/mL, [Spermine, Propylamine] = 9.1 mM, 50 mM HEPES (pH 7.4), room temperature.

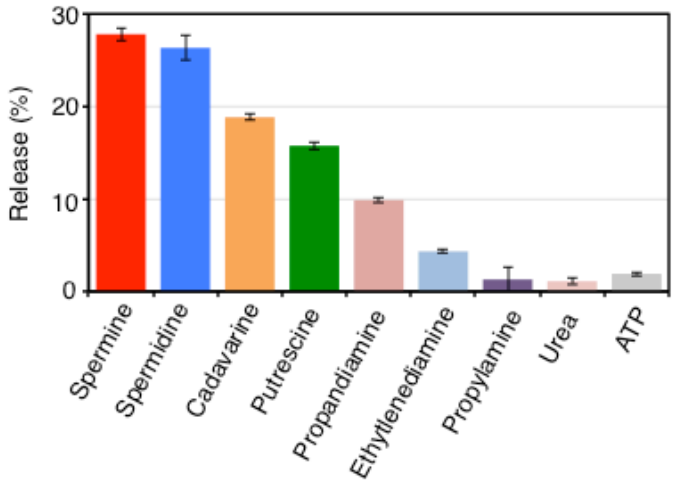

Figure 7. (**A**) Release of G-coum from MMT upon the addition of various substances. Conditions: [G-coum⊂MMT] = 1.0 mg/mL, [G-coum] = 0.23 μmol/mg of MMT (19% CEC), [Substances] = 10 mM, 50 mM HEPES (pH 7.4).

1-2-2. Spectroscopic properties of G-Coum

Absorption and fluorescence spectra showed the different state of G-Coum in solution and in MMT. At lower loadings such as 4%, both the monomer (470 nm) and the excimer emission (540 nm) [12] were observed (Figure 8A). Excitation spectra of the excimer emission peak showed a peak at 395 nm with a shoulder at 444 nm (Figure 8C), which is shifted compared with the absorption band of the monomeric form (430 nm), indicating that G-coum combined with MMT interacts with each other in the ground state. With increasing loading, the ratio of excimer emission (540 nm) was increased (Figure 8B and C). Concurrently, a broadened absorption band (fwhm: from 51 to 88.5 nm) was observed for G-coum in MMT (Figure 8C). As shown in Figure 8D (from (a) to (b)), it is interesting that the excimer emission at 540 nm decreased, whereas the monomer emission at 470 nm increased by the addition of spermine. These results suggest that G-coum was adsorbed and aggregated on the anionic surface of MMT at high loading levels compared to its CEC (cation-exchange capacity) and the aggregated G-coum in MMT was released into the aqueous phase as a monomeric form through the cation-exchange with spermine.

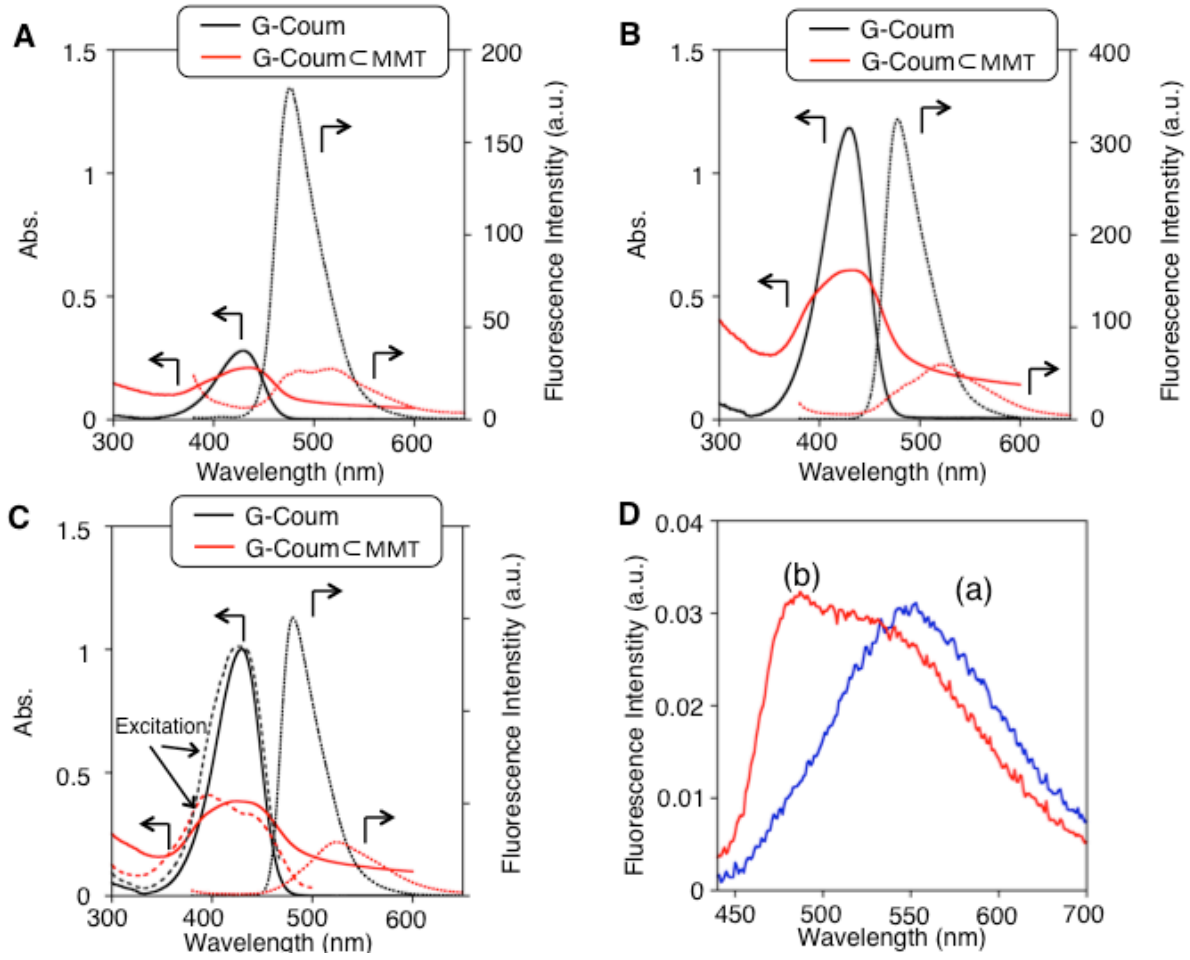

Figure 8. Absorption and fluorescence (λ_{ex} = 360 nm) spectra of aqueous G-coum solution ([G-coum] = 26 μM for (**A**) and 54 μM for (**B**)) and aqueous G-coum⊂MMT suspension for (**A**) 4.3% and (**B**) 9.0 %, and G-coum against CEC ([G-coum⊂MMT] = 0.50 mg/mL) and (**C**) Absorption, fluorescence (λ_{ex} = 360 nm), and excitation spectra (λ_{em} = 470 nm for G-coum and 540 nm for G-coum⊂MMT) of aqueous G-coum solution ([G-coum] = 117 μM for absorption and fluorescence spectra, 12 μM for excitation spectrum) and aqueous G-coum⊂MMT suspension ([G-coum⊂MMT] = 0.50 mg/mL, [G-coum] = 0.23 μmol/mg MMT (19%CEC)) at room temperature. (**D**) Fluorescence spectral change (λ_{ex} = 410 nm, MCPD (multichannel photodetector), see Supporting Information for details) of G-coum⊂MMT suspension (a) before and (b) after the addition of spermine. Conditions: [G-coum⊂MMT] = 0.40 mg/mL, [G-coum] = 0.23 μmol/mg of MMT (19% CEC), [Spermine] = 0.91 mM, 50 mM HEPES (pH 7.4).

1-2-3. Fluorescence change of G-coum⊂MMT/hydrogel 1 hybrid

Interestingly, the blue-shifted fluorescence of G-coum released by spermine was significantly intensified when the G-coum⊂MMT was embedded in a supramolecular hydrogel matrix (G-coum⊂MMT/hydrogel **1** hybrid) (Figure 9A). The fluorescence intensity at 470 nm by the addition of spermine was 5.0-fold greater than that in aqueous medium without hydrogel **1** (Figure 8C). This type of fluorescence spectral change, from the excimer to the enhanced monomer emission, can be ascribed to both the environmentally sensitive nature of the G-coum fluorescence[13] and the binding capacity of the supramolecular fiber. That is, the G-coum released from MMT by the exchange with spermine was spontaneously translocated from the aqueous phase to the hydrophobic space of supramolecular fibers **1**, where G-coum showed the intensified monomeric emission (Figure 10).[10] Confocal laser scanning microscopy supported the spermine-induced translocation of G-coum as follows. In hydrogel **1**, the fluorescence of G-coum⊂MMT was observed as fluorescent spots of 1-10 μm in diameter (Figure 11), indicating that G-coum was predominantly bound to MMT even in the hydrogel **1**. It was also evident that MMT was segregated from the supramolecular fibers **1** stained by a hydrophobic BODIPY dye. Clearly, these two microdomains are spatially orthogonal to each other in the semiwet matrix. After the addition of spermine, the segregated spots due to G-coum became smeared and more importantly the G-coum fluorescence was localized along the fibers **1** and overlapped significantly with the BODIPY fluorescence (the merged image, Figure 11B). The large change in fluorescence intensity along with the emission peak shift of the G-coum⊂MMT/hydrogel **1** hybrid upon the addition of spermine enabled us to accurately monitor the spermine concentration by two-wavelength emission ratiometry. As shown in Figure 9B, plotting the fluorescence intensity ratio between the monomer

and the excimer (F_{470}/ F_{540}) as a function of spermine concentration showed a typical saturation behavior, which clearly validates the fluorescence sensing ability of G-coum⊂MMT/hydrogel **1** hybrid for spermine. From the fluorescence titration experiments of various substances (Figure 9B), it was demonstrated that spermine and spermidine can be detected in the range of 20-100 μM (EC_{50} (the analyte concentration inducing 50% of the maximum signal change) = 29 (1.4 and 55 (4.8 μM for spermine and spermidine, respectively), whereas propylamine, urea, and ATP were not detected because of their low cation-exchange capability. This order is in good agreement with that obtained in the aqueous G-coum⊂MMT suspension system, indicating the cation selectivity of MMT remained even after the hybridization of supramolecular hydrogel. Figure 12A summarizes the sensing selectivity of G-coum⊂ MMT/hydrogel **1** for various substances on the basis of the changes in the fluorescence intensity ratio (F_{470}/F_{540}). It is clear that polyamines such as spermine and spermidine were detected the best, while aminoglycoside antibiotics such as neomycin and kanamycin and poly(L-lysine)[11] (low Mw: PLL-LMW) were also detectable effectively. However, diamines with spacers longer than C2 and proteins such as BSA (bovine serum albumin) were detected with only moderate sensitivity. By contrast, monoamines, ethylenediamine, anions such as ATP, heparin, and sucrose-octasulfate (Suc-8S), and neutral substances such as urea were not detectable. There was little difference in the sensing selectivity between pH 6.8 and 7.4, but the sensing selectivity was lowered at pH 8.0 most probably due to partial deprotonation of polyamines (Figure 14). Interestingly, these selective and large fluorescence peak shifts enabled us to distinguish polyamines with the naked eye in a high-throughput manner using a G-coum⊂MMT/hydrogel **1** hybrid sensor array chip. As shown in an inset of Figure 12A, intensified blue fluorescence spots for spermine (a1), spermidine (a2), putrescine (a4), and

PLL-LMW (b3) were observed, whereas other spots were weakly green for polyanions such as heparin (c3), Suc-8S (c4), and inositol hexaphosphate (IP6, c5).

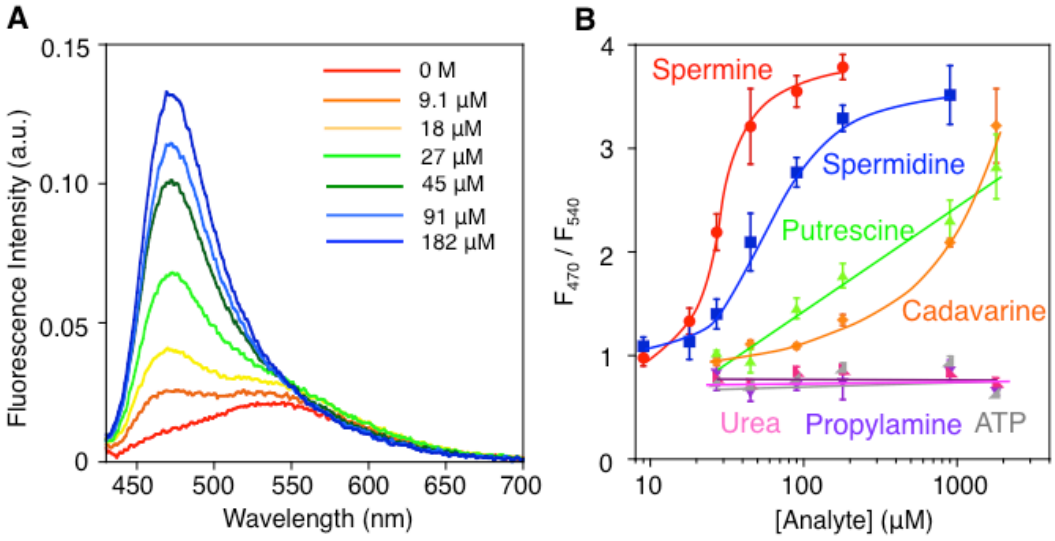

Figure 9. (A) Fluorescence spectral change (λ_{ex} = 410 nm, MCPD) of G-coum⊂MMT/hydrogel 1 upon the addition of spermine and (B) fluorescence titration curves (see also Figure S3 for the spectral changes). Lines for spermine and spermidine are best fit of Hill equation to data points. Error bars represent standard deviation (n = 3). Conditions: [**1**] = 0.18 wt %, [G-coum⊂MMT] = 0.40 mg/mL, [G-coum] = 0.23 μmol/mg of MMT (19% CEC), 50 mM HEPES (pH 7.4).

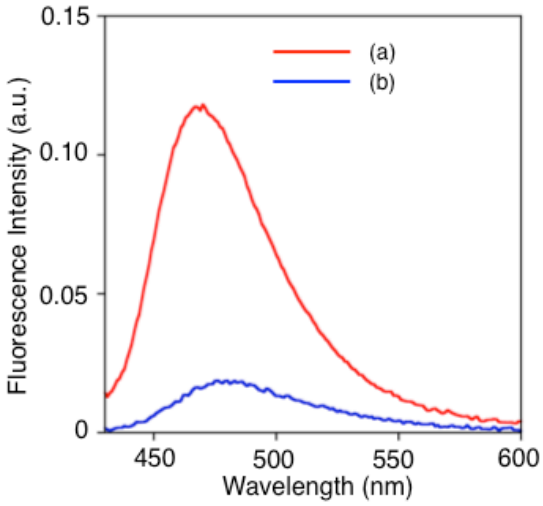

Figure 10. Fluorescence spectra (λex = 410 nm, MCPD) of G-coum (10 μM) in (a) 50 mM HEPES (pH 7.4) aqueous buffer and (b) hydrogel **1** ([**1**] = 0.20 wt%, 50 mM HEPES (pH 7.4)), room temperature.

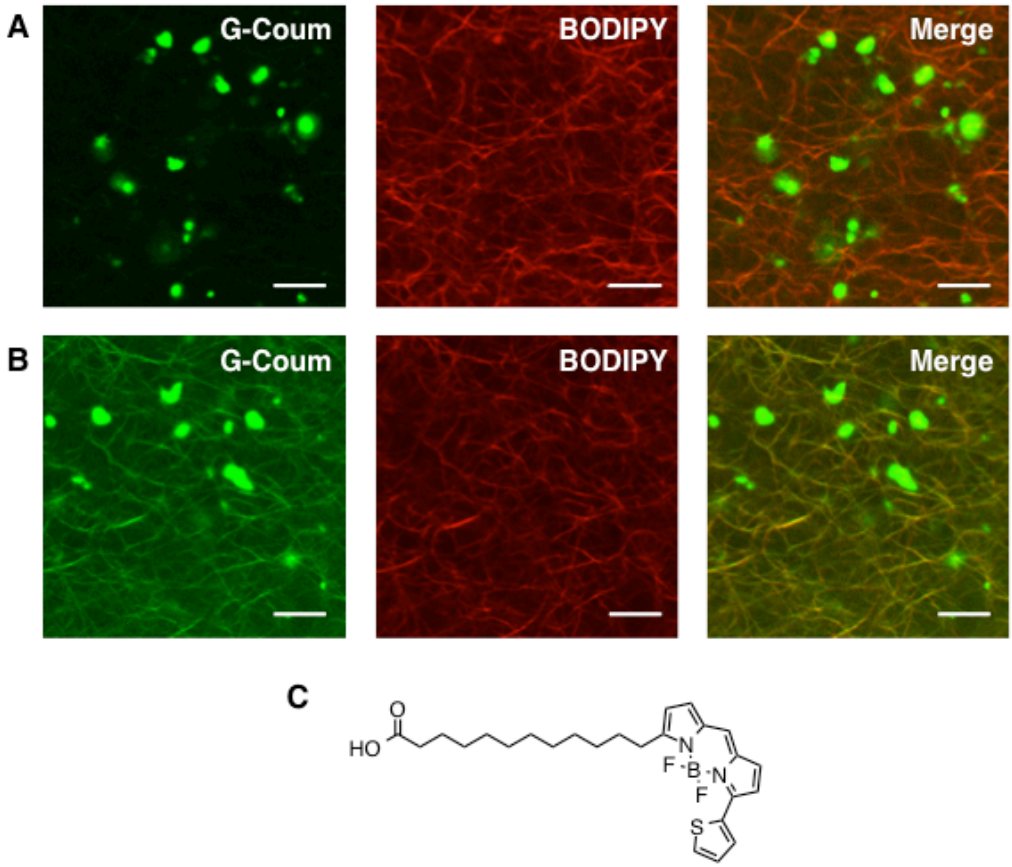

Figure 11. CLSM images of hydrogel **1** containing BODIPY dye and G-coum⊂MMT (**A**) before and (**B**) after 30 min of spermine addition. (left: λ_{ex} = 458 nm/ λ_{em} = 460–560 nm, center: λ_{ex} = 543 nm/λ_{em} = 565–605 nm, right: merged image). The merged image shown in the right panels were obtained by summing the images of left and center. (**C**) Chemical structure of BODIPY dye. The scale bars are 5 μm. Conditions: [**1**] = 0.18 wt%, [BODIPY] = 9.1 μM, [G-coum⊂MMT] = 0.40 mg/mL, [Spermine] = 182 μM, room temperature.

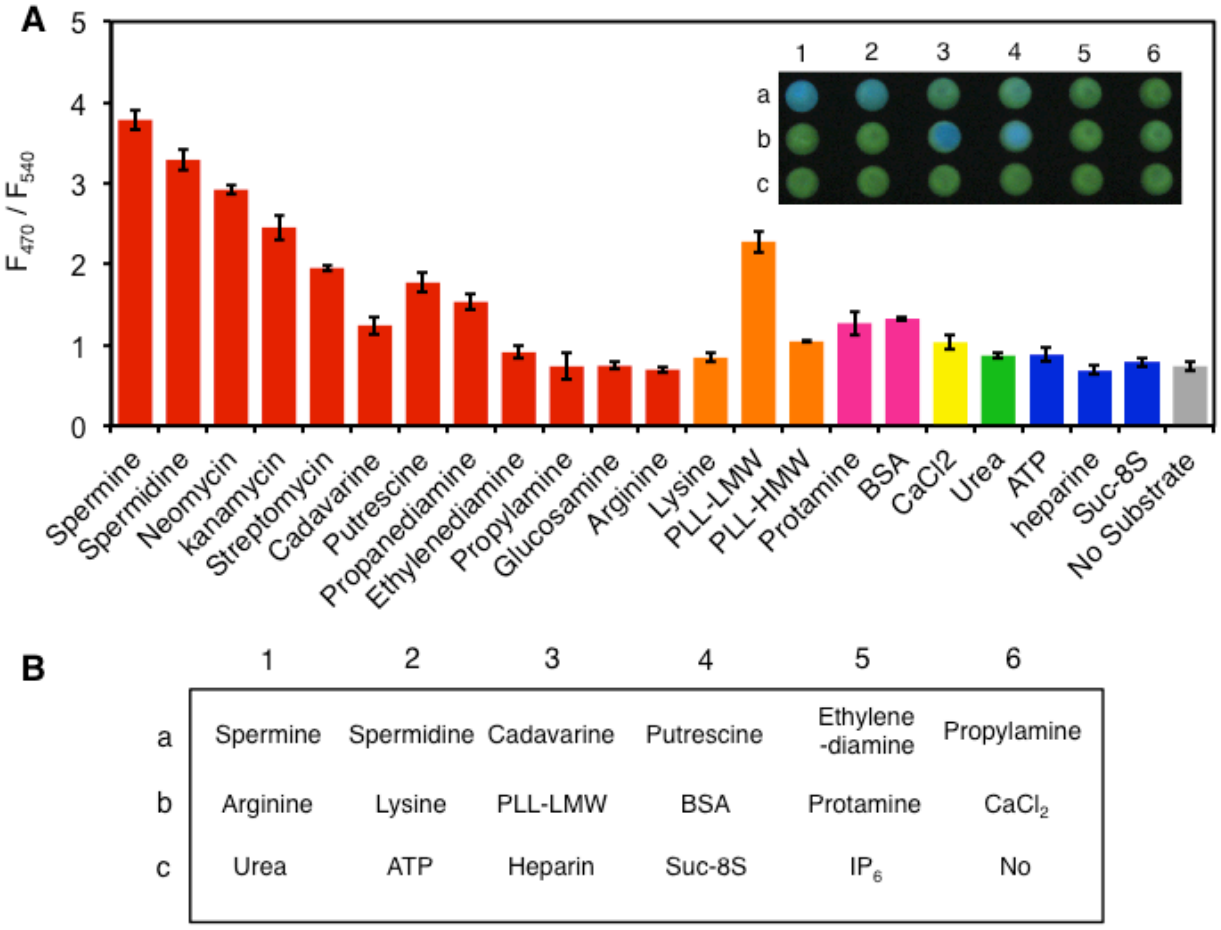

B

	1	2	3	4	5	6
a	Spermine	Spermidine	Cadavarine	Putrescine	Ethylene -diamine	Propylamine
b	Arginine	Lysine	PLL-LMW	BSA	Protamine	$CaCl_2$
c	Urea	ATP	Heparin	Suc-8S	IP_6	No

Figure 12. (**A**) Change in fluorescence intensity ratio (F_{470}/F_{540}) upon the addition of various substances. Inset shows photograph of G-coum⊂MMT/hydrogel **1** hybrid sensor chip (λ_{ex} = 365 nm) for high-throughput sensing of a variety of substances and the spotted position of the substances is shown in panel **B**. Conditions: spotted volume = 22 μL, [**1**] = 0.18 wt %, [G-coum⊂MMT] = 0.40 mg/mL, [G-coum] = 0.23 μmol/mg of MMT (19% CEC), [Substance] = 182 μM, 50 mM HEPES (pH 7.4).

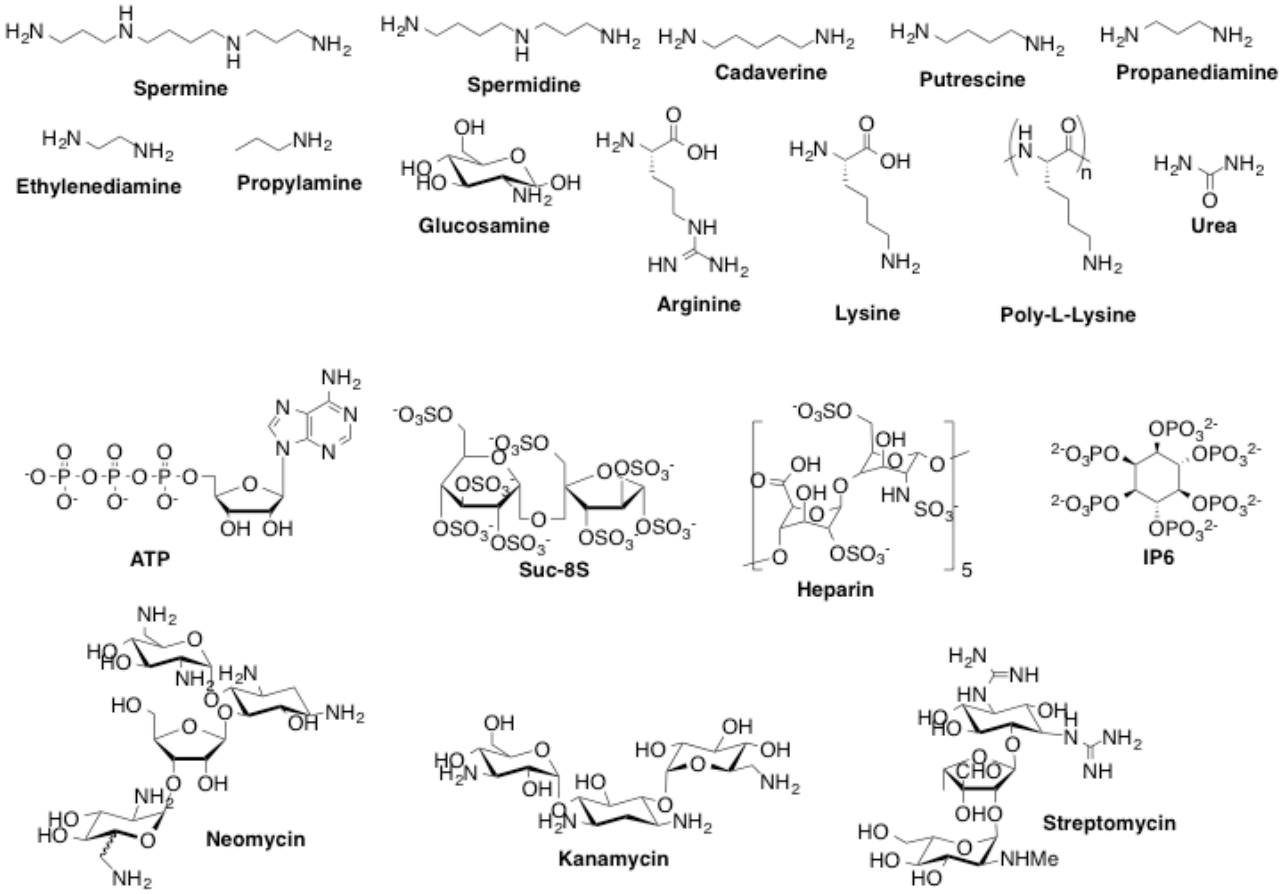

Figure 13. Chemical structures of analytes.

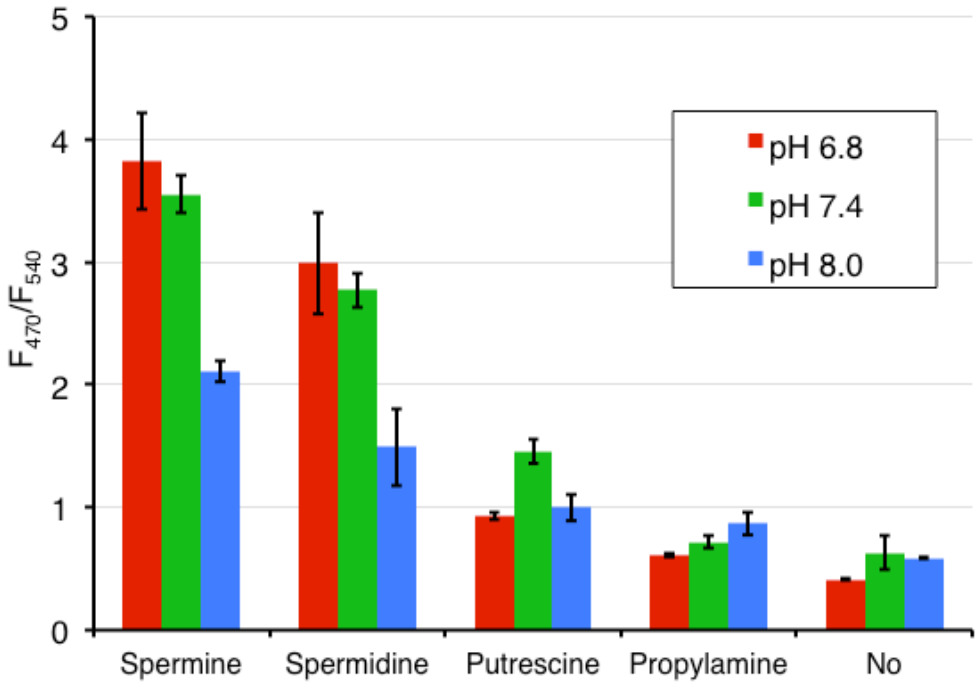

Figure 14. Change in fluorescence intensity ratio (F_{470}/F_{540}) upon the addition of various substances at different pH (6.8, 7.4, and 8.0). Conditions: spotted volume = 22 μL, [**1**] = 0.18 wt%, [G-coum⊂MMT] = 0.40 mg/mL, [G-coum] = 0.23 μmol/mg of MMT (19% CEC), [Substance] = 91 μM, 50 mM HEPES, room temperature.

1-2-3. Colorimetric detection of urinary polyamines in G-coum⊂MMT/hydrogel 1 hybrid

To demonstrate the potential in the practical utility of this hybrid sensor material, I finally conducted fluorocolorimetric imaging of spermine and spermidine in artificial urine by using the hybrid sensor array chip. It is proposed that changes in urinary spermine and spermidine concentrations are critical in the range from 1 to 10 μM and 10 to 50 μM, respectively, for cancer diagnosis.[1,12] As shown in Figure 15A, changes in the fluorescence colors were clearly distinguished from green to blue for spermidine (lane a) indeed in such a concentration range (0-45 μM) and for spermine (lane b) in a slightly higher concentration range (0-27 μM), relative to such criteria. The color change required only a few minutes, and both the pixel intensity ratios (I_{blue}/I_{green})

of the digital photograph and the fluorescence intensity ratios (F_{470}/F_{540}) of the fluorescence spectra almost linearly increased (Figure 15B,C). These results suggest that the present hybrid fluorescent sensor array is tolerant of biological fluids and substances such as serum albumin (HSA) and creatinine (Figures 16, 17) and could be rapid and sensitive enough for diagnosis applications.

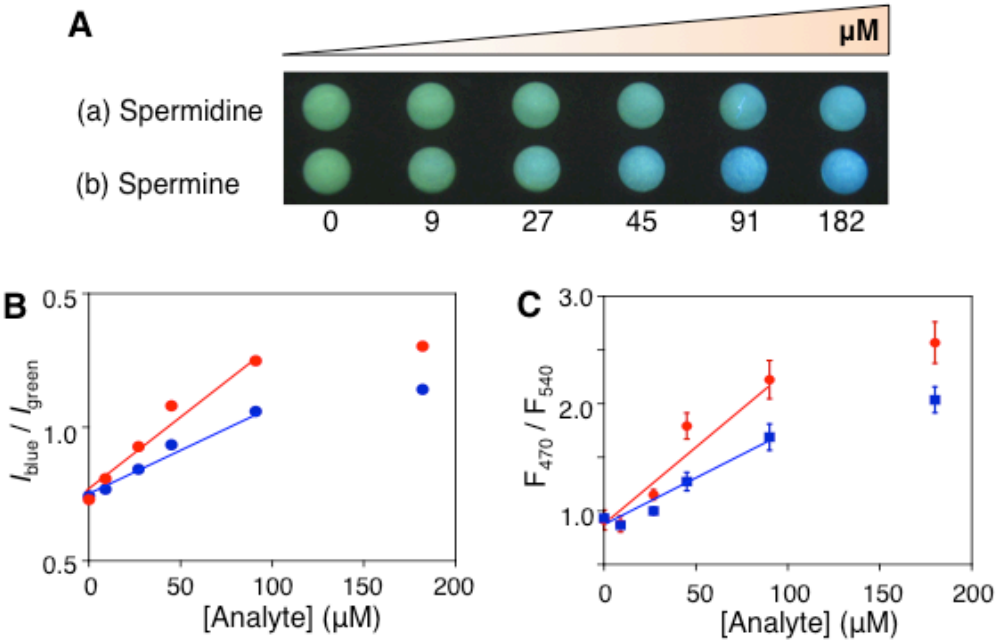

Figure 15. Photograph of G-coum⊂MMT/hydrogel **1** hybrid sensor chip (λ_{ex} = 365 nm) for (**A**) fluorocolorimetric sensing of (a) spermidine and (b) spermine in artificial urine and the corresponding changes in (**B**) pixel intensity ratio (I_{blue}/I_{green}) and (**C**) fluorescence intensity ratio (F_{470}/F_{540}, MCPD). Conditions: spotted volume = 22 μL, [**1**] = 0.18 wt %, [G-coum⊂MMT] = 0.40 mg/mL, [G-coum] = 0.23 μmol/mg of MMT (19% CEC), 50 mM HEPES (pH 7.4).

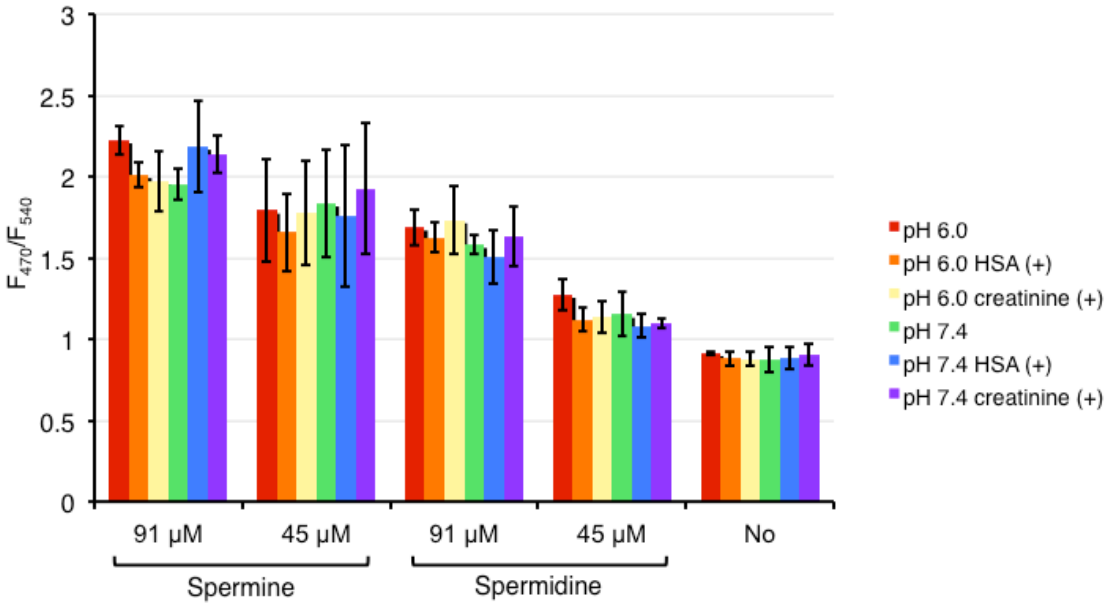

Figure 16. Change in fluorescence intensity ratio (F_{470}/F_{540}, MCPD) upon the addition of artificial urine (pH 6.0 and 7.4) containing spermine or spermidine with HSA ([HSA] = 15 μM (1.0 mg/mL[12])) or creatinine ([Creatinine] = 7 mM). Conditions: spotted volume = 22 μL, [**1**] = 0.18 wt%, [G-coum⊂MMT] = 0.40 mg/mL, [G-coum] = 0.23 μmol/mg of MMT (19% CEC), [Spermine, Spermidine] = 45, 91 μM, 50 mM HEPES (pH 7.4).

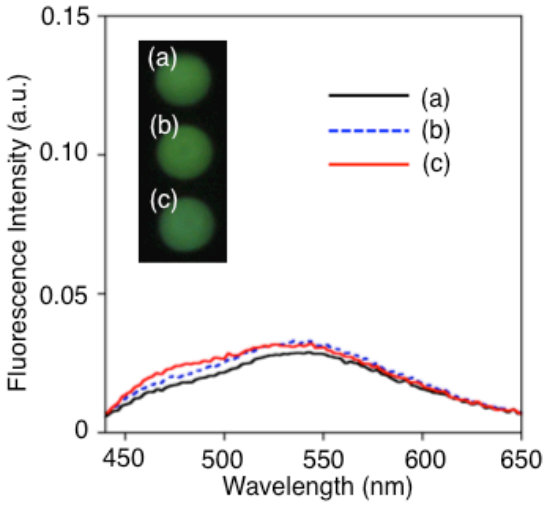

Figure 17. Fluorescence spectra (λ_{ex} = 410 nm, MCPD) of G-coum⊂MMT /hydrogel **1** hybrid sensor spots (20 μL) (a) before and after the addition of (b) HEPES buffer (50 mM, pH 7.4, 2.0 μL) and (c) artificial urine (2.0 μL). ([**1**] = 0.18 wt%, [G-coumMMT] = 0.40 mg/mL). Inset shows the corresponding photograph of G-coumMMT/hydrogel **1** hybrid sensor chip.

1-3. Conclusion

I succeeded in developing a new hybrid material of G-coum⊂MMT/supramolecular hydrogel **1** that can fluorocolorimetrically sense polyamines in a biological fluid mimic, achieving rapid and the naked eye detection. The sensing sensitivity was almost in the range demanded for cancer diagnosis and clinical usage, although further practical tests for verification are required. The present results also demonstrated that the rational hybridization of inorganic hosts with supramolecular hydrogel is a general approach for designing sensor systems for a variety of analytes. Construction of not only sensors but also controlled drug release materials may be attractive targets or further research using this type of hybrid soft materials.

1-4. Experimental Section

Generals.

Unless stated otherwise, all commercial reagents were used as received. Synthetic Na^+-saturated MMT (Kunipia-F, CEC = 1.19 μmol/mg) was kindly supplied from Kunimine industries Co. (Japan). Unless otherwise specified, all water used in the experiments refers to ultra pure water obtained from a Millipore system having a specific resistance of 18 MΩ•cm. Thin layer chromatography (TLC) was performed on silica gel $60F_{254}$ (Merck). Column chromatography was performed on silica gel 60N (Kanto, 40–50 μm). ^{1}H NMR spectra were obtained on a Varian Mercury 400 spectrometer with tetramethylsilane (TMS) or residual non-deuterated solvents as the internal references. Multiplicities are abbreviated as follows: s = singlet, d = doublet, t = triplet, q = quartet, m = multiplet, dd = double doublet, br = broad. Mass spectrometry was performed on a Thermo Scientific Exactive mass spectrometer. The absorption and fluorescence spectra were measured using a Shimadzu UV2550 and a Perkin-Elmer LS55 spectrometer, respectively. Fluorescence spectra of hydrogel spots on a slide glass plate were recorded using an Otsuka Electronics high sensitivity Spectro multichannel photodetector, MCPD-7000. Elemental analysis was carried out by the services at Kyoto University.

Synthesis.

Compounds **1**[7], **2**[13], and **7**[14] were synthesized according to the methods reported previously. G-coum was prepared from **2** as shown in **Scheme 1**.

Scheme 1.

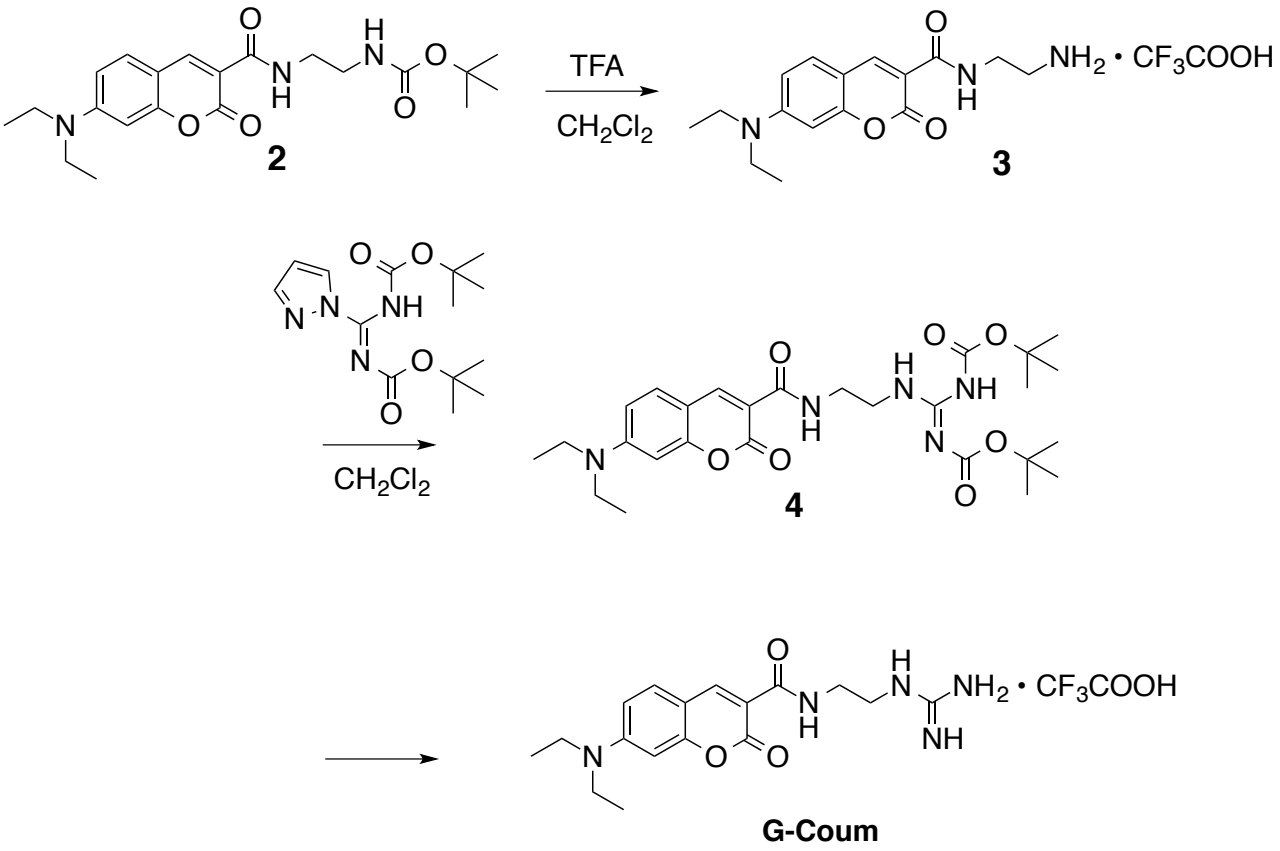

Synthesis of compound 3.

To a solution of compound **2** (608 mg, 1.5 mmol) in dry dichloromethane (CH_2Cl_2, 4 mL) was added trifluoroacetic acid (TFA, 2 mL), and the mixture was stirred at room temperature for 90 min. The solvent was then evaporated and the residual TFA was removed by azeotropy with toluene. The residue was precipitated with diisopropyl ether to give compound **3** (594 mg, 94%) as a yellow solid. ^{1}H NMR (400 MHz, $CDCl_3$, room temperature): δ = 1.24 (t, J = 7.2 Hz, 6H), 3.16 (t, J = 5.8 Hz, 2H), 3.54 (q, J = 7.1 Hz, 4H), 3.67 (t, J = 5.8 Hz, 2H), 6.59 (d, J = 2.4 Hz, 1H), 6.81 (dd, J = 2.4 and 8.8 Hz, 1H), 7.56 (d, J = 8.8 Hz, 1H), 8.66 ppm (s, 1H).

Synthesis of compound 4.

To a solution of compound **3** (300 mg, 0.72 mmol) and *N,N*-diisopropylethylamine (DIPEA,

500 μL, 2.9 mmol) in dry acetonitrile (CH_3CN, 7 mL) was added *N,N'*-di-Boc-1H-pyrazole-1-carboxamidine (186 mg, 0.60 mmol), and the mixture was stirred at room temperature overnight. The solvent was removed under reduced pressure and the residue was purified by column chromatography (SiO_2, hexane: ethyl acetate (AcOEt) = 1:1). To remove residual pyrazole completely, the obtained yellow solid was dissolved in AcOEt (50 mL) and the solution was washed with saturated aqueous $NaHCO_3$ (50 mL × 3), 5% aqueous citric acid (50 mL × 3), and brine (50 mL). The organic layer was collected and dried over anhydrous Na_2SO_4 and filtrated. The filtrate was evaporated to dryness to give compound **4** (316 mg, 97%) as a yellow solid. 1H NMR (400 MHz, $CDCl_3$, room temperature): δ = 1.24 (t, J = 7.0 Hz, 6H), 1.48–1.50 (s × 2, 18H), 3.45 (q, J = 7.2 Hz, 4H), 3.61–3.67 (m, 4H), 6.49 (d, J = 2.4 Hz, 1H), 6.64 (dd, J = 2.4 and 8.8 Hz, 1H), 7.42 (d, J = 9.2 Hz, 1H), 8.57 (br s, 1H), 8.69 (s, 1H), 8.94 (m, 1H), 11.48 ppm (br s, 1H).

Synthesis of G-coum.

To a solution of compound **4** (315 mg, 0.58 mmol) in dry CH_2Cl_2 (10 mL) was added TFA (5 mL). The mixture was stirred at room temperature for 3 h. The solvent was then evaporated and the residual TFA was removed by azeotropy with toluene. The residue was dissolved in a minimal amount of methanol and reprecipitated with diisopropyl ether. The solid was collected by filtration, washed with diisopropyl ether, and dried *in vacuo* to give **G-coum**•TFA (210 mg, 79%) as a yellow solid. ^{1}H NMR (400 MHz, CD_3OD, room temperature): δ = 1.23 (t, J = 7.2 Hz, 6H), 3.39 (t, J = 6.2 Hz, 2H), 3.48–3.59 (m, 6H), 6.58 (d, J = 2.0 Hz, 1H), 6.83 (dd, J = 2.4 and 8.8 Hz, 1H), 7.56 (d, J = 8.8 Hz, 1H), 8.65 ppm (s, 1H). HR-FTMS (ESI): Calcd. for $[M(C_{17}H_{23}N_5O_3)+H]^+$: m/z = 346.1879;

Found: 346.1862. Anal. Calcd. for $C_{17}H_{23}N_5O_3$•TFA: C, 49.67; H, 5.27; N, 15.24; Found: C, 49.38; H, 5.50; N, 15.08 %.

Scheme 2.

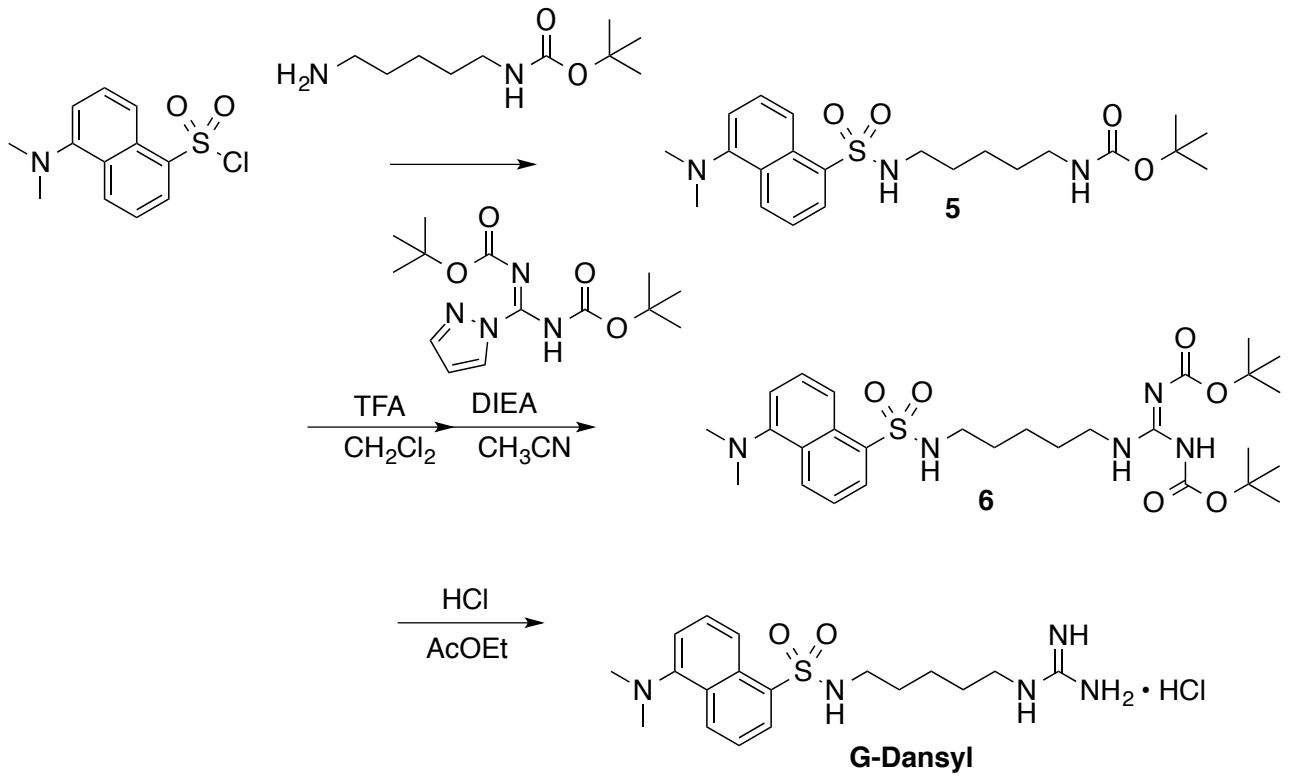

Synthesis of 5

To a stirred dry CH_2Cl_2 (8.0 mL) solution of Dansyl-Chloride (253 mg, 0.94 mmol) and DIEA (490 µL, 2.8 mmol) was added *N*-(*tert*-Butoxycarbonyl)-1,5-diaminopentane (228 mg, 1.1 mmol). The solution was stirred at rt overnight. The solvent was removed under reduced pressure and the residue was purified by column chromatography (silica, hexane: AcOEt = 4:1 to 2:1) to give **5** (394 mg, 96%) as yellow solid. ^{1}H NMR (400 MHz, $CDCl_3$, room temperature): δ = 1.21–1.32 (m, 2H), 1.14–1.20 (m, 2H), 1.35–1.45 (m, 11H), 2.86–2.96 (m, 10H), 4.40 (brs, 1H), 4.62 (brs, 1H), 7.20 (d, J = 6.8 Hz, 1H), 7.51–7.59 (m, 2H), 8.23–8.30 (m, 2H), 8.55 ppm (d, J = 8.4 Hz, 1H).

Synthesis of 6

To a stirred dry CH_2Cl_2 (8 mL) solution of **5** (130 mg, 0.30 mmol) was added TFA (2.0 mL). The solution was stirred for 30 min. The volatile was removed under reduced pressure. After azeotropic with toluene (20 mL x 3), the residue was dried *in vacuo*. Then the residue was dissolved in CH_3CN (5.0 ml). To this solution, DIEA (260 μL, 1.5 mmol) and *N*,*N*'Bis(*tert*Butoxycarbonyl) 1H-Pyrazole-1-carboxyamidine (127 mg, 0.41 mmol) was added. After stirring at rt for 14 h, the solvent was removed under reduced pressure. Then the residue was dissolved in CH_2Cl_2 (20 mL). The organic layer was washed with water (20 mL) and brine (20 mL) and dried over $MgSO_4$. The solvent evaporated to dryness. The residue was purified by column chromatography (silica, hexane:AcOEt = 4:1 to 2:1) to give **6** (136 mg 79%) as light green amorphas. ^{1}H NMR (400 MHz, $CDCl_3$, room temperature): δ = 1.17–1.50 (m, 24H), 2.86 – 2.92 (m, 8H), 3.24 (q, J = 6.5, 2H), 4.54 (t, J = 6.0 Hz, 1H), 7.19 (d, J = 8.0 Hz, 1H), 7.51–7.59 (m, 2H), 8.20–8.28 (m, 3H), 8.55 ppm (d, J = 8.4 Hz, 1H).

Synthesis of G-Dansyl

To a stirred dry AcOEt (2 mL) solution of **6** (50 mg, 87 μmol) was added 4N HCl/AcOEt (5.0 mL). The solution was stirred for 24 min. After evaporation, the residue was washed with ether (10 mL) to give **G-Dansyl** (39 mg, 100%) as light green amorphas. ^{1}H NMR spectroscopy (CD_3OD, 400 MHz, rt): δ = 1.29–1.37 (m, 2H), 1.43–1.52 (m, 4H), 2.89 (t, J = 6.8 Hz, 2H), 3.09 (t, J = 7.0 Hz, 2H), 3.47 (s, 6H), 7.84–7.91 (m, 2H), 8.08 (d, J = 7.6 Hz, 1H), 8.36 (d, J = 7.2 Hz, 1H), 8.60 (d, J = 8.8 Hz, 1H), 8.91 ppm (d, J = 8.8 Hz, 1H).

Scheme 3.

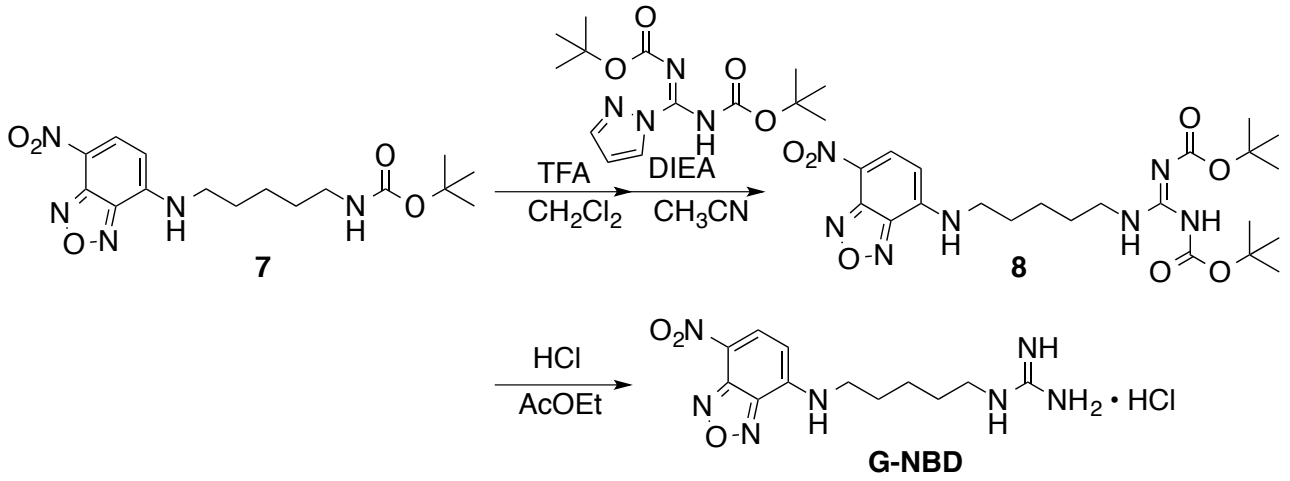

Synthesis of 8

To a stirred dry CH_2Cl_2 (8 mL) solution of 7[14] (120 mg, 0.33 mmol) was added TFA (2.0 mL). The solution was stirred for 30 min. The volatile was removed under reduced pressure. After azeotropy with toluene (2 mL x 3), the residue was dissolved in CH_3CN (5.0 mL). To this solution, DIEA (230 μL, 1.3 mmol) and *N*,*N*'Bis(*tert*Butoxycarbonyl) 1H-Pyrazole-1-carboxyamidine (127 mg, 0.26 mmol) was added. The solution was stirred at rt for 14 h. The solvent was removed under reduced pressure. Then the residue was dissolved in CH_2Cl_2 (20 ml). The organic layer was washed with water (20 mL) and brine (20 mL) and dried over $MgSO_4$.The solid was removed by filtration. The solvent was removed under reduced pressure. The residue was purified by column chromatography (silica, hexane:AcOEt = 4:1 to 2:1) to give **8** (91 mg 69%) as orange amorphous. ^{1}H NMR spectroscopy ($CDCl_3$, 400 MHz, rt): δ = 1.45-1.58 (m, 20H), 1.65-1.70 (m, 2H), 1.83-1.89 (m, 2H), 3.43-3.55 (m, 4H), 6.19 (d, J = 8.8 Hz, 1H), 6.32 (brs, 1H), 8.36 (brs, 1H), 8.50 (d, J = 8.8 Hz, 1H), 11.5 ppm (s, 1H).

Synthesis of G-NBD

To a stirred dry AcOEt (2 mL) solution of **8** (48 mg, 87 μmol) was added 4N HCl/AcOEt (5.0 mL). The solution was stirred for 27 h. The appeared orange solid was collected by filtration and was washed with AcOEt (10 mL x 3). The residue was dried in vacuo to give **G-NBD** (39 mg 100%) as orange solid. ^{1}H NMR (400 MHz, CD_3OD, room temperature): δ = 1.51–1.56 (m, 2H), 1.63–1.71 (m, 2H), 1.79–1.86 (m, 2H), 3.19 (t, J = 7.0 Hz, 2H), 3.56 (brs, 2H), 6.36 (d, J = 8.4 Hz, 1H), 8.53 (d, J = 8.8 Hz, 1H)

Preparation of G-coumMMT.

MMT (10 mg) was suspended in a designated concentration (60, 120, 240 μM) of G-coum aqueous solution (50 mM HEPES (pH 7.4), 10 mL) and the resultant suspension was vortexed and sonicated. After overnight standing at room temperature, the suspension was centrifuged (5000 rpm, 10 min) and the supernatant was removed. The obtained solid was washed with 50 mM HEPES (pH 7.4, 5.0 mL) for four times to afford G-coumMMT as a yellow solid. All supernatants were collected and un-encapsulated G-coum was evaluated by absorption spectroscopy. The obtained G-coumMMT in aqueous suspension (0.50 mg/mL, 50 mM HEPES (pH 7.4)) in a 2-mm path length quartz cell (2 mm × 1 cm) was subjected to fluorescence and absorption spectroscopy.

Release experiments of G-coum⊂MMT.

An aqueous suspension of G-coum⊂MMT (1.0 mg/mL, 500 μL) in 50 mM HEPES (pH 7.4) in a 1-mL tube was centrifuged (5000 rpm, 10 min) and the supernatant was removed. To the tube was added each substance solutions (10 mM, 500 μL), pipetted gently and incubated for 1 h at room

temperature. The suspension was then centrifuged (5000 rpm, 10 min) and the supernatant was subjected to absorption spectroscopy to determine the released G-coum.

Preparation of G-coum⊂MMT/hydrogel 1 hybrid.

A suspension of gelator **1** (2.2 mg) in 50 mM HEPES buffer (pH 7.4, 1.0 mL) was heated to form homogeneous solution and allowed to cool to room temperature. This solution (450 μL) was immediately added to an aqueous suspension of G-coum⊂MMT (4.0 mg/mL, [G-coum] = 0.23 μmol/mg MMT (19%CEC), 50 μL) in 50 mM HEPES (pH 7.4) buffer. The resultant suspension was pipetted gently and allowed to gelate at room temperature to prepare G-coumMMT/hydrogel **1** hybrid.

CLSM observation for investigating translocation of G-coum.

A freshly prepared suspension (20 μL) of G-coum⊂MMT and **1** containing BODIPY dye (10 μM) as described above was spotted on a glass-bottom dish (Matsunami, non-coat, 0.15–0.18 mm-glass bottom) and incubated to complete gelation in a sealed box with high humidity at room temperature for 30 min. The samples before and 30 min after the addition of spermine (2.0 mM, 2.0 μL) were subjected to observations using an inverted confocal laser scanning microscope (Olympus FV1000-ASW) equipped with a 543 nm and 633 nm Helium Neon, a 458, 488, 515 nm multi Ar laser (Coherent Inc.). A 100×, NA = 1.40 oil objective or a 10×, NA = 0.40 air objective were employed to obtain images.

Fluorescent sensing of polyamine utilizing G-coum⊂MMT/supramolecular hydrogel 1 hybrid.

A freshly prepared suspension of G-coum⊂MMT and **1** as described above was spotted on a slide glass plate (Matsunami, 76 × 26 mm (24 well, φ = 4 mm), each spot contains 20 μL). The plate was incubated to complete gelation in a sealed box with high humidity at room temperature for 30 min and each substance solution (2.0 μL) at designed concentrations was added to a spot. After 30 min, the plate was subjected to MCPD fluorescence measurements. The photographs of the hydrogel chip were collected by using a digital camera (Canon, Powershot G7) equipped with a cut-off filter (<440 nm)) in the front of the lens under UV irradiation using a handy lamp (365 nm, 4 W). The images were analyzed with ImageJ 1.38 on a Macintosh PC.

Preparation of artificial urine.

An artificial urine solution was prepared according to the method reported previously.[15] The artificial urine solution contained 1.1 mM lactic acid, 2.0 mM citric acid, 25 mM sodium bicarbonate, 170 mM urea, 2.5 mM calcium chloride, 90 mM sodium chloride, 2.0 mM magnesium sulfate, 10 mM sodium sulfate, 7.0 mM potassium dihydrogen phosphate, 7.0 mM dipotassium hydrogen phosphate, and 25 mM ammonium chloride all mixed in water. The pH of the solution was adjusted to 6.0 by addition of 1.0 M hydrochloric acid. Solutions of spermine or spermidine were prepared using the artificial urine solution.

Reference

(1) (a) Russell,D.H. *Nat.(London),NewBiol.***1971**, 233, 144–145. (b) Kawakita, M.; Hiramatsu, K. *J. Biochem.* **2006**, 139, 315–322. (c) Byun, J. A.; Choi, M. H.; Moon, M. H.; Kong, B.; Chung, B. C. *Cancer Lett.* **2009**, 273, 300–304.

(2) (a) Paik,M.J.; Kuon,D.; Cho,J.; Kim,K.-R. *AminoAcids* 2009, 37, 407–413. For a review, see (b) Bachrach, U. *Amino Acids* **2004**, *26*, 307–309.

(3) (a) Satrijo, A.; Swager, T. M. *J. Am. Chem. Soc*. **2007**, *129*, 16020–16028. (b) Tanima, D.; Imamura, Y.; Kawabata, T.; Tsubaki, K. *Org. Biol. Chem*. **2009**, *7*, 4689–4694.

(4) (a) Liu, Y.-l.; Palacios, M. A.; Anzenbacher, P., Jr. *Chem. Commun*. 2010, 1860–1862. (b) Zyryanov, G. V.; Palacios, M. A.; Anzenbacher, P., Jr. *Angew. Chem., Int. Ed*. 2007, 46, 7849–7852. (c) Palacios, M. A.; Nishiyabu, R.; Marquez, M.; Anzenbacher, P., Jr. *J. Am. Chem. Soc.* **2007**, *129*, 7538–7544. (d) Das, G.; Talukdar, P.; Matile, S. *Science* **2002**, *298*, 1600–1602. (e) Litvinchuk, S.; Tanaka, H.; Miyatake, T.; Pasini, D.; Tanaka, T.; Bollot, G.; Mareda, J.; Matile, S. *Nat. Mater*. **2007**, *6*, 576–580. (f) Wiskur, S. L.; Ait-Haddou, H.; Lavigne, J. J.; Anslyn, E. V. *Acc. Chem. Res.* **2001**, *34*, 963–972.

(5) (a) Kiyonaka, S.; Sada, K.; Yoshimura, I.; Shinkai, S; Kato, N.; Hamachi, I. *Nat. Mater*. **2004**, *3*, 58–64. (b) Koshi, Y.; Nakata, E.; Yamane, H.; Hamachi, I. *J. Am. Chem. Soc.* **2006**, *128*, 10413–10422. (c) Wada, A.; Tamaru, S.-i.; Ikeda, M.; Hamachi, I. *J. Am. Chem. Soc.* **2009**, *131*, 5321–5330. (d) Ikeda, M.; Ochi, R.; Hamachi, I. *Lab Chip* **2010**, *10*, 3325–3334.

(6) Ogawa, M.; Kuroda, K. *Chem.Rev.*1995, 95, 399–438.

(7) Komatsu, H.; Ikeda, M.; Hamachi, I. *Chem. Lett.* **2011**, 40, 198–200.

(8) (a) Viaene, K.; Caigui, J.; Schoonheydt, R. A.; DeSchryver, F. C. *Langmuir* **1987**, *3*, 107–111.

(b) DellaGuardla, R. A.; Thomas, J. K. *J. Phys. Chem*. **1983**, *87*, 3550–3557.

(9) Ethylenediamine would not act as dication but mainly as monocation due to its low second p*K*a (p*K*a1 = 9.93, p*K*a2 = 6.85). Ozaki, H.; Nakamura, A.; Arai, M.; Endo, M.; Sawai, H. *Bull. Chem. Soc. Jpn*. **1995**, *68*, 1981–1987.

(10) Wagner, B. D. *Molecules* 2009, 14, 210–237.

(11) The monomer unit concentration was set to be the same for poly(L-lysine)s. Increase in the total concentration of poly(L-lysine), (high Mw: PLL-HMW) induced a larger change in the fluorescence intensity ratio (data not shown).

(12) A standard urinary creatinine concentration of 1.3 mg/mL was used for the calculations. Urinary creatinine concentration is widely used as a dilution marker of the urine sample.

(13) Tsukiji, S.; Miyagawa, M.; Takaoka, Y.; Tamura, T.; Hamachi, I. *Nat. Chem. Biol*. **2009**, *5*, 341–343.

(14) Ikeda, M.; Fukuda, K.; Tanida, T.; Yoshii, T.; Hamachi, I. *Chem. Commun.,* **2012**, 48, 2716–2718.

(15) Brooks, T.; Keevil, C. W. *Lett. Appl. Microbiol.* **1997**, *24*, 203–206.

(16) Normal urinary protein concentration was reported to be below 30 μg/mL. Isoe, J.; Kaneko, E. *Chem. Lett.* **2006**, *35*, 922–923.

Chapter 2

Two-Photon-Responsive Supramolecular Hydrogel for Controlling Materials Motion in Micrometer Space

Abstract

Spatiotemporal control of fluidity inside soft-matrix by external stimuli allows us real-time manipulation of nano/micro materials. In this study, I constructed the first two-photon responsive peptide-based supramolecular hydrogel, the fluidity of which was dramatically controlled with high spatial resolution (10 μm × 10 μm × 10 μm). The Off-On switching of Brownian motion of nanobeads and bacterial chemotaxis by two-photon excitation was successfully demonstrated.

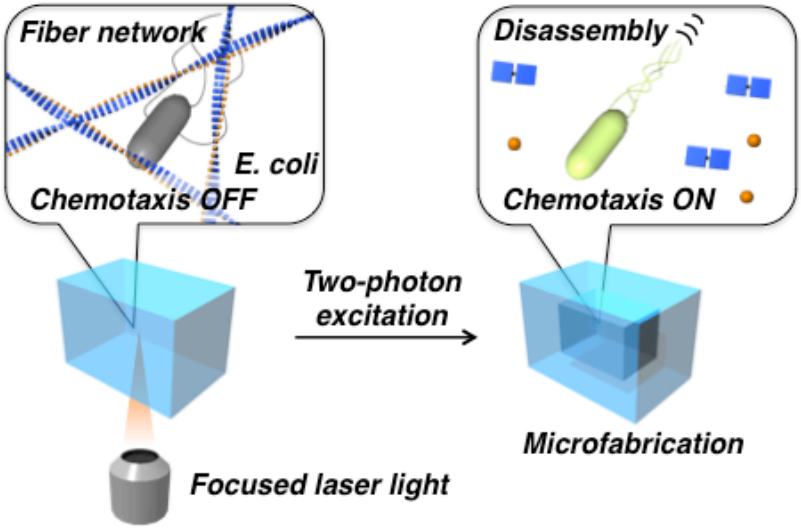

2-1. Introduction

Supramolecular hydrogels[1] formed by self-assembly of small molecules are promising biomaterials for numerous applications such as cellular scaffold[2], controlled drug release[3], and bio-sensing[4]. Compared to conventional polymer gels, supramolecular hydrogels are anticipated to exhibit unique functions such as fluidic nanofiber networks[5], dynamic or flexible stimuli responsive properties[6]. It is now recognized that precise control of the gel structure and functions is crucial for construction of sophisticated soft biomaterials comprising supramolecular hydrogels not only to facilitate understanding impact of surrounding environment on a unique biological function, but also for manipulating various biological phenomena[7]. Many stimuli-responsive supramolecular hydrogels[6] have been developed to date. Among them, light is an attractive stimulus because of its contactless mode and high spatiotemporal resolution. Indeed, several groups reported photo-responsive supramolecular hydrogels using photo-isomerization reaction or photo-click chemistry[8]. However, these simply employed UV light irradiation, which shows cytotoxicity without careful dose adjustment. Regarding biomaterials application, two-photon responsiveness is apparently superior to one-photon owing to its high biocompatibility. A few distinctive chromophores are able to absorb two-less energetic photons simultaneously upon irradiation of intense laser pulses[9] to generate the same excited state as that of one-photon excitation. This allowed one to utilize the two-fold longer wavelength light (typically near infrared (NIR) region), which is more appropriate to fabricate the hydrogels with less cytotoxicity. As another advantage, three-dimensional (3D) fabrication *inside* the gel matrix can be performed with the high spatial resolution by the two-photon process, because the two-photon excitation event occurs only at a focal point, depending on the numerical aperture of lens, wavelength of light, and the refractive

index of the materials. In this context, it was recently reported that two-photon-responsive polymer gels,[10] for example, hydrogels consisting of poly(ethylene glycol) cross-linked with a photolabile o-nitrobenzyl group,[10a,b] can be employed as cell culture matrices for controlling extracellular microenvironment (Figure 1).[10] Although the inside fluidity was not quantitatively examined in detail, the polymers remaining after photodegradation are presumed to remain in the irradiated space. By contrast, two-photon-responsive supramolecular hydrogels have not yet been developed, despite these being expected to show a drastic change in fluidity because all the photogenerated residues are small molecules. I describe herein the design of the first supramolecular hydrogel composed of peptide capable of exhibiting gel-sol transition upon two-photon excitation, which enables the creation of 3D fluidic micron spaces inside the gel with high spatial resolution and with high fluidity equivalent to aqueous solution. Also, I successfully demonstrated locally controlling the Brownian motion of nanobeads and regulation of chemotaxis of living bacteria in Off-On mode, without inactivation of biological process inside the two-photon responsive supramolecular hydrogel matrix.

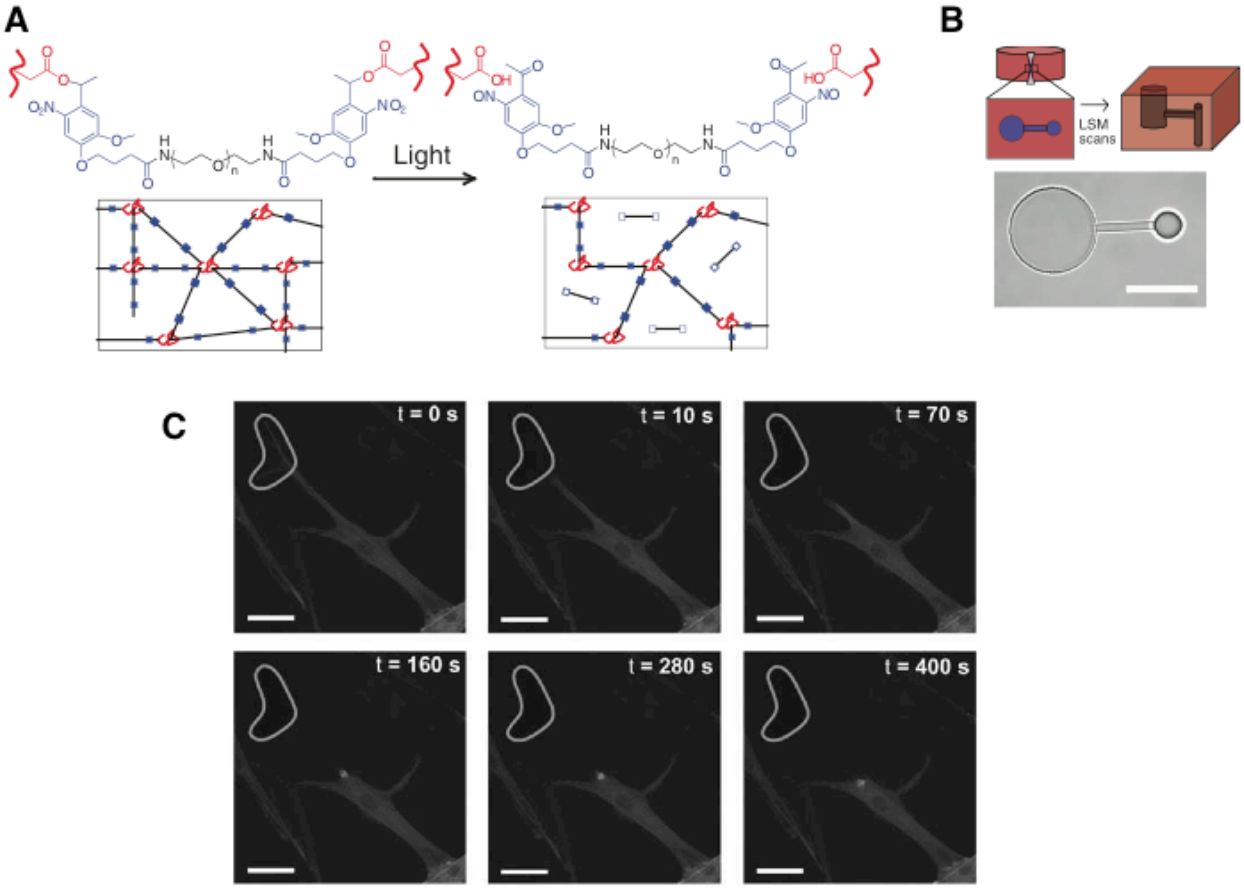

Figure 1. (**A**) Schematic representation of photodegradable polymeric hydrogel. (**B**) 3D photo-fabrication of the gel. (**C**) Two-photon induced detachment and retraction of GFP–actin transfected MSCs from PEGdiPDA hydrogels.

2-2. Results and Discussions

2-2-1. Molecular design and screening of the gelator

We recently established the semi-rational design strategy of various stimuli-responsive peptide-based supramolecular hydrogelators[11]. For instance, incorporating a photostimuli-responsive 7-bromo-hydroxycoumarin-4-yl-methoxycarbonyl (Bhcmoc) protecting group into the N-terminus of a dipeptide (FF, F: phenylalanine) allowed us to obtain a supramolecular gel was obtained, which showed the gel-sol change by (one) photo-triggered cleavage of Bhcmoc moiety (Figure 2A, B). Based on this scaffold, I sought to explore two-photon responsive hydrogels. Since the Bhcmoc-FF does not form hydrogel at physiological pH probably due to deprotonation of the hydroxyl group of Bhcmoc, I decided to replace Bhcmoc with dimethylamino-coumarin-4-yl-methoxycarbonyl[12] (DMACmoc) group, a typical two-photon absorption dye, at the N-terminal of peptides. A small library of DMACmoc-modified peptides by varying the peptide sequence was constructed as shown in Figure 3A and the gelator screening was conducted at pH 7.4. By the tube inversion method, I found four gelators that form transparent hydrogels, which should be appropriate for efficient photo-absorption with minimizing the photo-diffraction, in neutral aqueous conditions (pH 7.4) (Figure 3). The critical gelation concentrations (CGC) of each gelator were evaluated and summarized in Figure 3B. DMACmoc-FF(CF_3) showed the lowest CGC (0.050 wt%) in transparent gel, which was thus mainly used for further studies. Although DMACmoc-F(CF_3)F(CF_3) showed the lower CGC (0.025 wt%), the gel was opaque which was thought to be unsuitable for the photo-reaction.

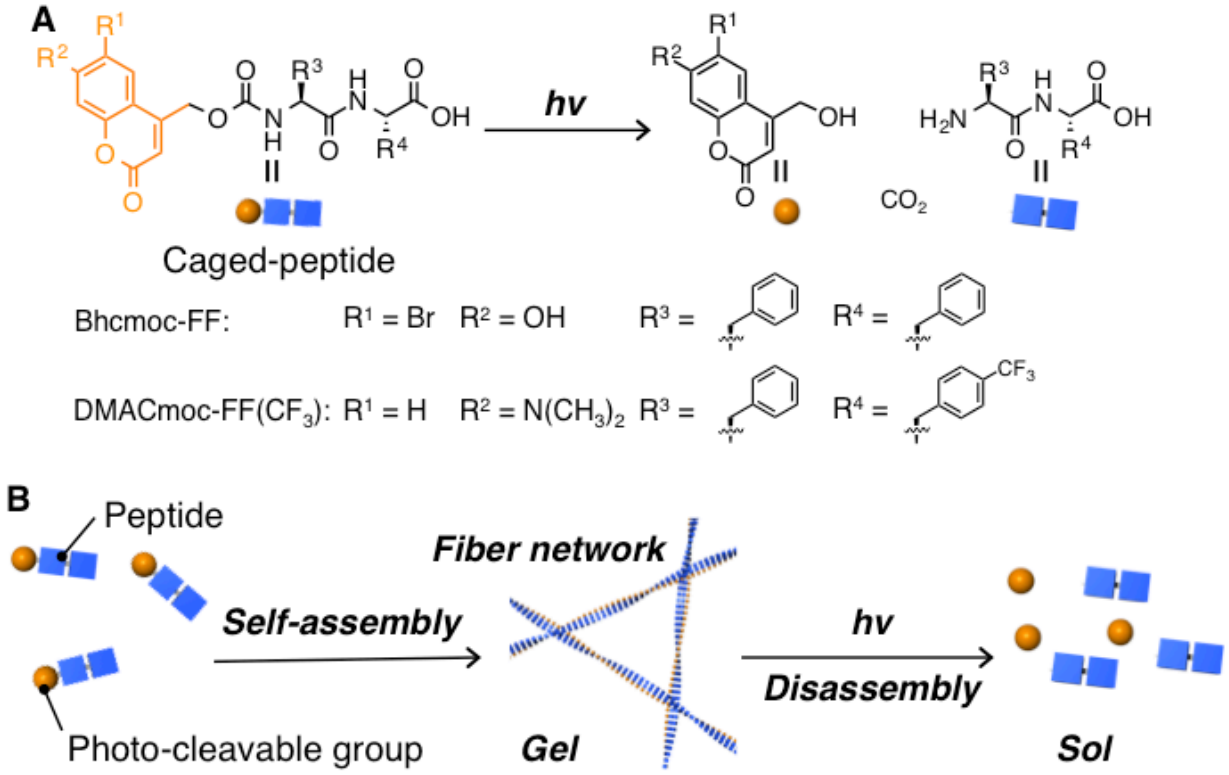

Figure 2. (**A**) Photo-induced cleavage reaction of caged-peptide gelator. (**B**) Schematic representation of the self-assembly of caged-peptide gelator to form a supramolecular hydrogel and its photo-responsive gel-to-sol transition.

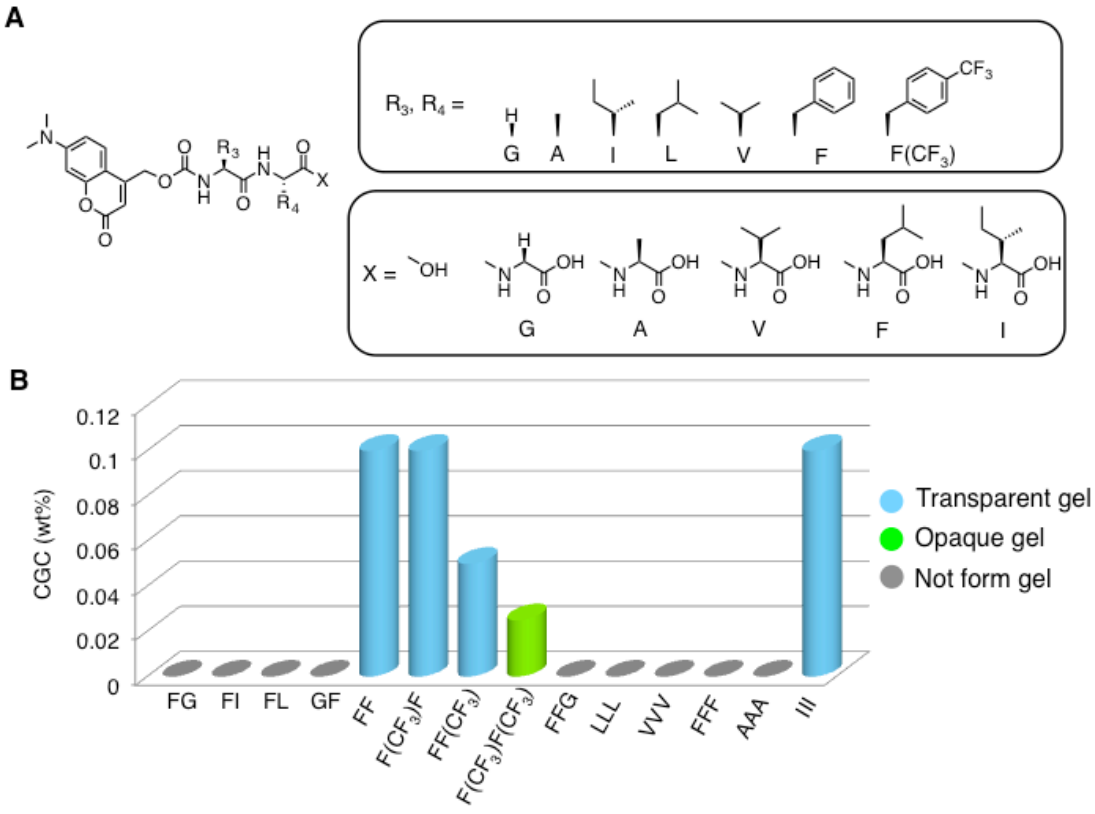

Figure 3. Result of the gelator screening. (**A**) Chemical structure of the gelator candidates. (**B**) Summary of the gelation test and critical gelation concentration (CGC; wt%) values.

2-2-2. Characteristic of the DMACmoc-FF(CF_3) gel

The nanostructure of the dried DMACmoc-FF(CF_3) gel was analyzed by transmission electron microscopy (TEM). Fibrous structure with diameters of 20-30 nm and micrometers in length was observed (Figure 4A). Confocal laser scanning microscopy (CLSM) observation of the DMACmoc-FF(CF_3) gel stained with a cationic fluorescence dye (DEAC-gua[4b]: 10 μM, Figure 4B) clearly revealed the presence of fiber network in a semi-wet state (Figure 4C). Circular dichroism (CD) spectrum suggested the formation of β-sheet-like secondary structure (217 nm) and chiral arrangement of aromatic side chains of the peptide (250 nm) and DMAC chromophore (394 nm) in

the fibrous aggregates[13]. The rheological data of the DMACmoc-FF(CF_3) hydrogel showed the typical viscoelastic property of the hydrogel consisting of fiber networks, that is *G'* is greater than *G"* (Figure 5)[14]. To evaluate the mesh size of the DMACmoc-FF(CF_3) gel, I then encapsulated fluorescent nanobeads and examined their Brownian motion[15]. In the case of beads with a diameter of 250 nm, random movement (Brownian motion) of the beads in DMACmoc-FF(CF_3) gel (0.075 wt%) was observed (Figure 6A). In contrast, the Brownian motion of beads having the diameter of 500 nm stopped due to entrapment by the entangled gel fiber meshes (Figure 6B). These results indicate that the DMACmoc-FF(CF_3) hydrogel (0.075 wt%) formed nanomeshs with the void spaces between 250 nm and 500 nm. The relationship between the Brownian motion at different beads sizes and gelator concentrations was evaluated in detail and summarized in Figure 6C.

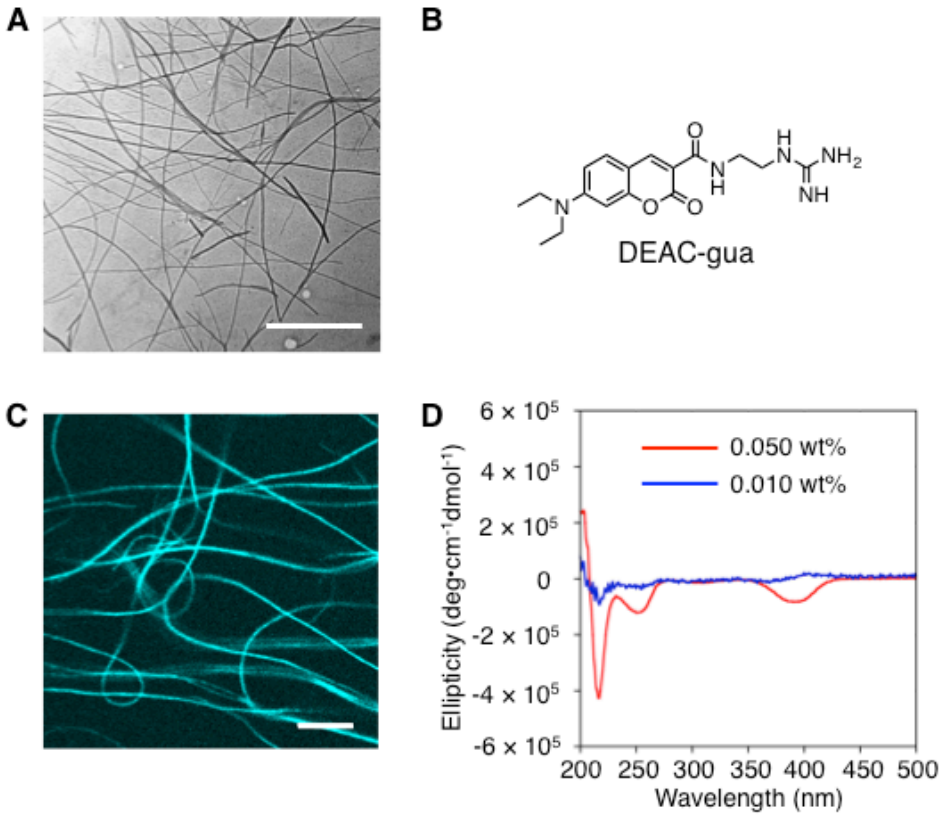

Figure 4. (**A**) TEM image of DMACmoc-FF(CF_3) gel. Scale bar is 500 nm. (**B**) Chemical structure of DEAC-gua. (**C**) CLSM image of DMACmoc-FF(CF_3) gel stained with DEAC-gua (10 μM). Scale bar is 5 μm. (**D**) CD spectra of DMACmoc-FF(CF_3) sol (0.01 wt%) and gel (0.05 wt%) in 200 mM HEPES (pH 7.4). A positive Cotton effect at 200 nm and a negative one at 217 nm appeared only in the gel state, indicating the formation of β-sheet-like secondary structure in the nanofiber. Also, induced CD signal at 250 nm and 394 nm showed the chiral arrangement of aromatic side chains of the peptide and DMAC chromophore in the fibrous aggregates, respectively.

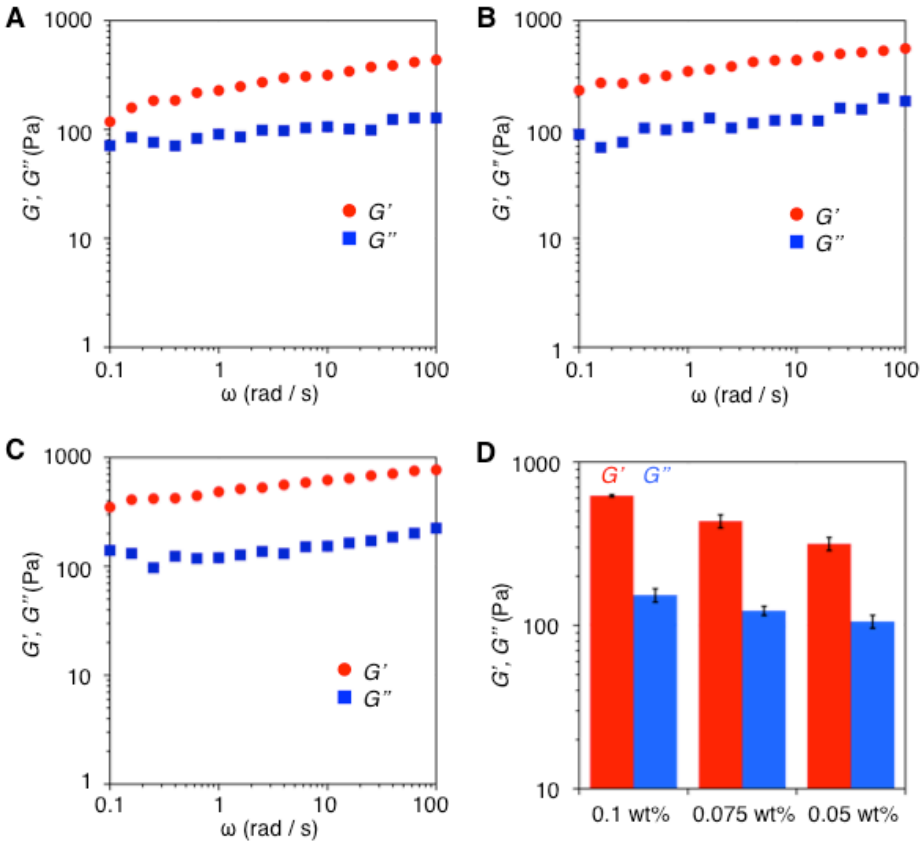

Figure 5. Rheological properties (1% strain) of DMACmoc-FF(CF_3) gel. (A-C) Frequency sweep rheological properties of DMACmoc-FF(CF_3) gel (*G´*: storage modulus, *G˝*: loss modulus). [DMACmoc-FF(CF_3)] = 0.05 wt% (A), 0.075 wt% (B). 0.10 wt% (C). (D) Summary of rheological properties (*G´*, *G˝* at angular frequency of 10 rad/s) of DMACmoc-FF(CF_3) gel at different concentrations (Standard deviations were evaluated from three different experimental results).

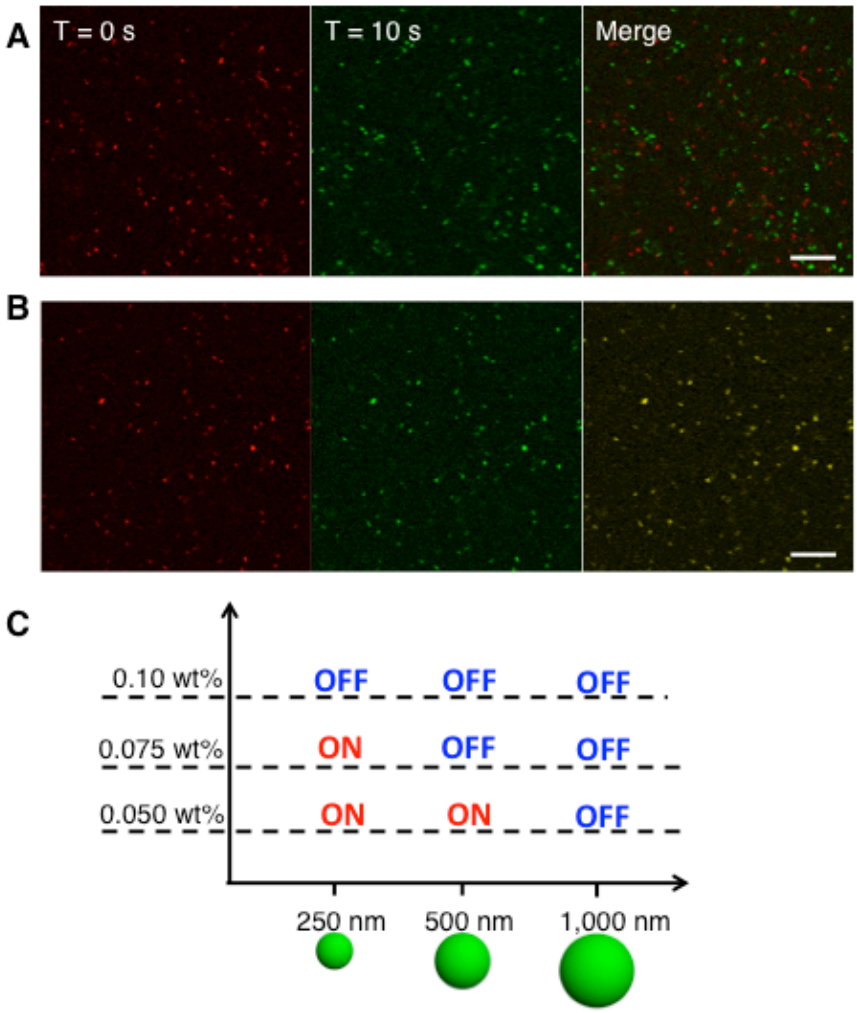

Figure 6. Brownian motion of the fluorescent 250 nm nanobeads in (A) 0.075 wt% and (B) 0.10 wt% DMACmoc-FF(CF_3) gel. The fluorescence images were converted into pseudocolors (red: T = 0 s, green: T = 10 s) and merged. (C) Summary of the Brownian motions of 250–1000 nm nanobeads in DMACmoc-FF(CF_3) hydrogel at different gelator concentrations.

2-2-3. One-photon-induced gel-sol transition

In order to confirm the photo-responsive function of DMACmoc-FF(CF_3) gel, I firstly irradiated the gel (0.080 wt%) with one-photon excitation by a stand-alone Hg lamp (360 nm, 49 mW, 5 min), which caused macroscopic gel-sol transition as shown in Figure 7A. HPLC analysis of

the photo irradiated sample revealed the decrease of the DMACmoc-FF(CF_3) and the concurrent increase of the cleaved product H-FF(CF_3) in an irradiation time dependent manner (Figure 8). These results indicate that the cleavage reaction at the DMACmoc moiety occurred by one-photon excitation. The gel to sol transition was observed after 56% of the gelator had decomposed, which was in good agreement with the CGC value of this gelator.

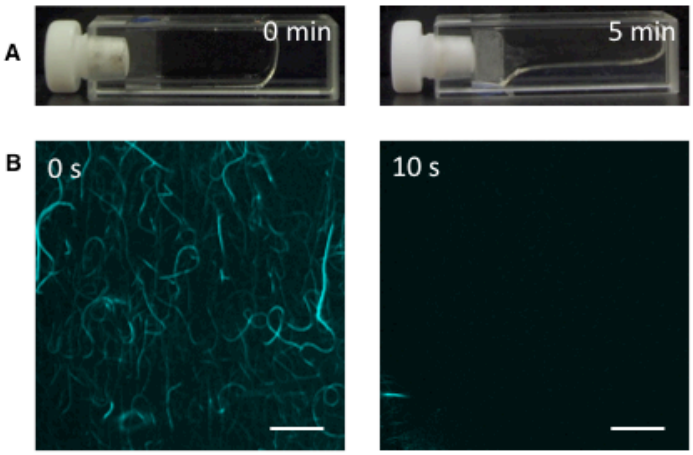

Figure 7. One-photon-responsive gel-sol transitions of DMACmoc-FF(CF_3) hydrogel. (A) Photographs of the DMACmoc-FF(CF_3) gel before and after the irradiation of UV light (360 nm). (B) CLSM images of the DMACmoc-FF(CF_3) gel stained with DEAC-gua (10 μM, see Fig. 4B for the molecular structure and experimental for the details) before and after UV light irradiation (360 nm) by the one-photon excitation using a Hg lamp (360 nm) equipped with CLSM through a 100× objective lens for 10 s. Scale bar is 20 μm.

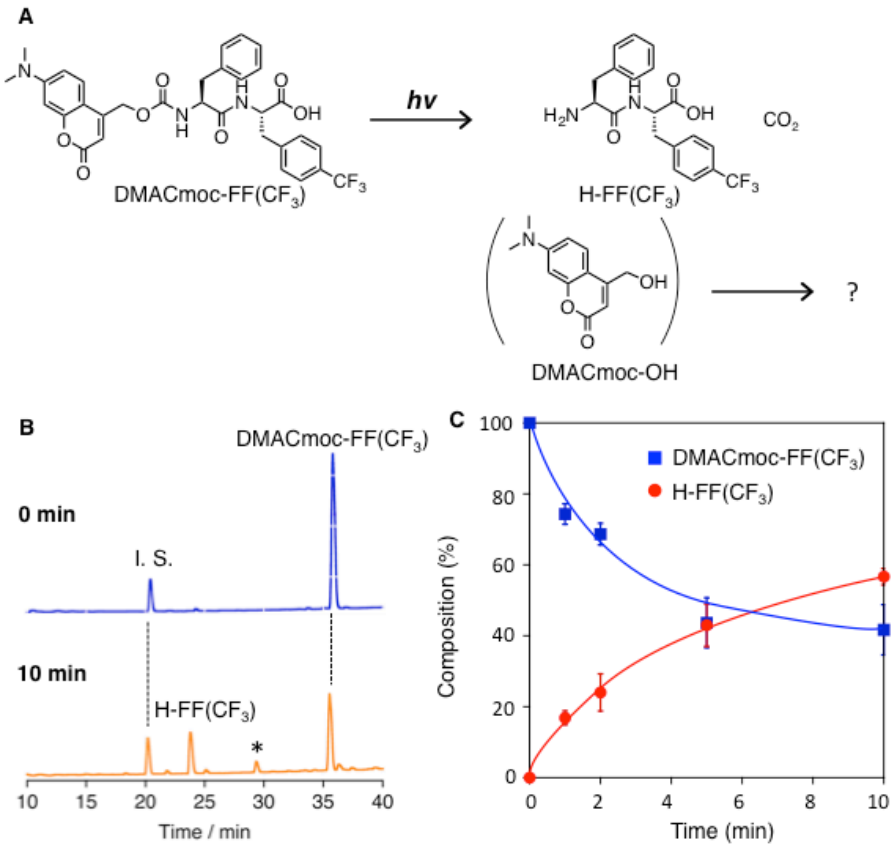

Figure 8. Analysis of photo-induced reaction. (A) Photo-induced cleavage reaction of DMACmoc-FF(CF_3). (B) HPLC traces of DMACmoc-FF(CF_3) gel before and after irradiation of UV light (360 nm, 10 min). 4-Nitrobenzensulfonamide was used as internal standard (I. S.). Peak with asterisk mark * (29 min): not identified. The peak assignable to DMACmoc-OH, which should appear 23 min, was not observed after irradiation of UV light most probably because of further decomposition of DMACmoc-FF(CF_3). (C) Time-dependent changes in the composition of each component estimated from HPLC traces during irradiation (360 nm).

2-2-4. Two-photon induced gel-sol transition

I next examined the local gel-sol transition inside the DMACmoc-FF(CF_3) gel upon two-photon excitation (Figure 9A). A two-photon laser scanning microscope was utilized both for observing the supramolecular fiber and for fabricating the supramolecular hydrogel at different powers, typically, 0.4% for the fiber observations and 10% for the gel fabrications (near-IR (NIR)

pulse laser at 740 nm, 3 W, 140 fs). When DMACmoc-FF(CF_3) gel (0.10 wt%) stained with the DEAC-gua (10 μM) was irradiated by the NIR laser (10%), the entangled fibers disappeared at the irradiated area for only 2 s of total irradiation time as shown in Figure 9B. It is noteworthy that the inside of DMACmoc-FF(CF_3) gel was three-dimensionally fabricated by two-photon excitation with 8 μm spatial resolution in *z*-axis direction (Figure 9C (right)). In contrast, the spatial resolution in *z*-axis by one-photon fabrication (UV laser at 405 nm, 30 mW, 30%, 2 s)) was rather broad, that is 25 μm (Figure 9D (right)). Apparently, the two-photon fabrication of DMACmoc-FF(CF_3) gel was three times more precise than the one-photon fabrication. This is attributed to the difficulty for the one-photon excitation to perfectly prevent the formation of the excited state along the space where the light passes through. Besides, the present response time is short (2 s) enough to fabricate more complex patterns such as alphabetical letters by scanning NIR laser light (Figure 9E).

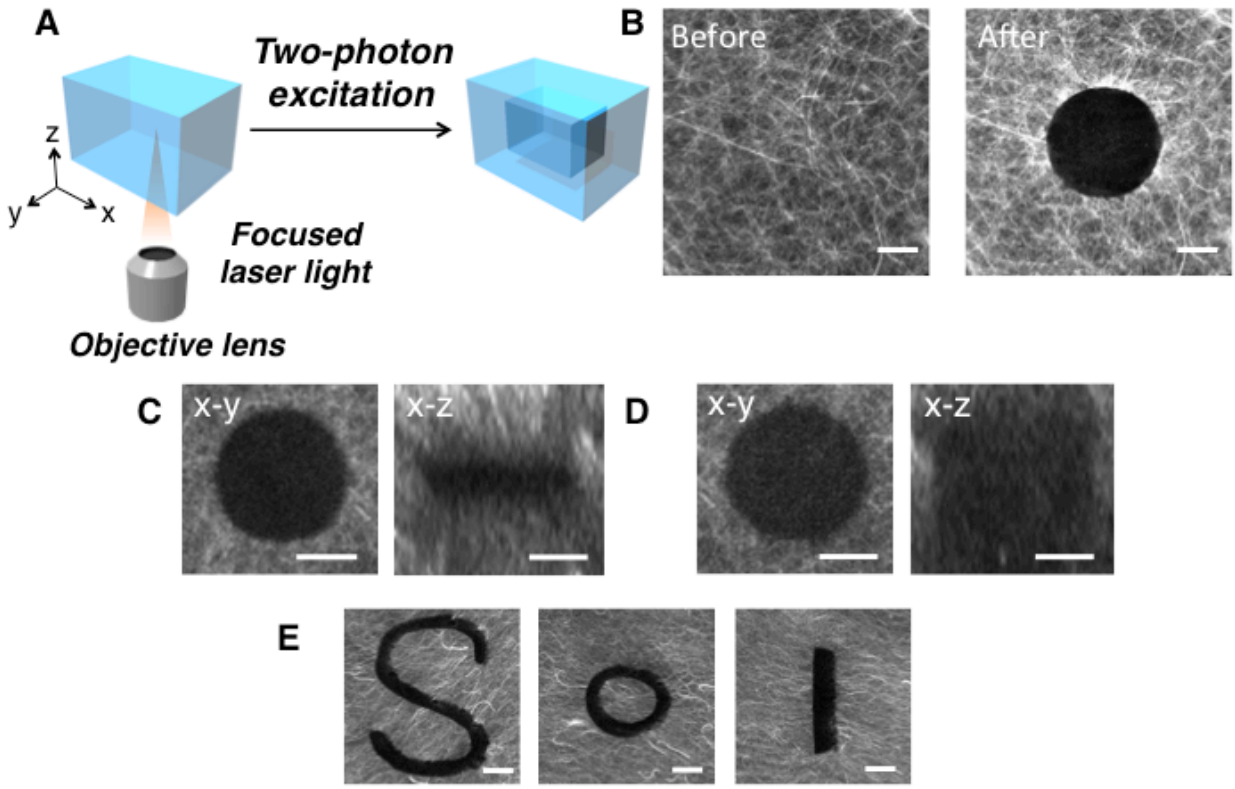

Figure 9. (A) Schematic representation of the photo-fabrication of DMACmoc- FF(CF_3) gel by two-photon excitation. (B) CLSM images of the DMACmoc- FF(CF3) gel (0.1 wt%) stained with DEAC-gua (10 μM) before and after two- photon irradiation (740 nm, 2 s). Scale bar is 10 μm. (C, D) CLSM images of x-y and x-z cross section DMACmoc-FF(CF_3) gel fabricated by (C) two-photon or (D) one-photon excitation. Scale bar is 10 μm. (E) Alphabetical letters patterned by two-photon excitation. Scale bar is 20 μm.

2-2-5. Photo-modulation of the Brownian motions of nanobeads

I subsequently sought to perform a remote photo-modulation of the Brownian motion of nanobeads inside the gel matrix by the focal gel-to-sol transition upon two-photon irradiation. The DMACmoc-FF(CF_3) gel encapsulating 500 nm nanobeads was treated by NIR light (740 nm, 3 W, 10%, 2 s). Before photo- irradiation, the locations of all bead at 0 s overlapped well with those after 10 s by CLSM observation (Figure 10A), indicating that the Brownian motion of the beads stopped

due to entrapment by nanomeshs of the gel fibers. After NIR irradiation, the locations of the beads did not merge in the irradiated area whereas the overlapping still remained in the un-irradiated area, which revealed that the Brownian motion restarted only by photo-irradiation. To evaluate the speed of the Brownian motion of the beads inside the gel, the beads motion was traced every 0.49 s and the migration distance was plotted against time (Figure 11). The speed in the irradiated area was determined to be 1.6 ± 0.6 μm/s. By contrast, the bead speed was approximately 25-fold slower (0.06 ± 0.04 μm/s) in the un-irradiated area (Figure 10B). Also, assuming a two-dimensional Brownian motion according to the Einstein-Smoluchowski relation, the analysis based on the mean-square displacements as a function of time allowed us to estimate the local viscosity (η) in the irradiated area to be 2.8×10^{-3} Pa·s according to the Stokes-Einstein equation. Remarkably, this is almost comparable to the viscosity of pure water (8.9×10^{-4} Pa·s)[16], suggesting that highly fluidic focal space was created inside the hydrogel matrix by the two-photon stimuli. These results indicate that the fluidity increased (or the viscosity decreased) along with the fiber disappearance (*vide supra*) only in the irradiated focal space, owing to the two-photon responsive gel-sol transition.

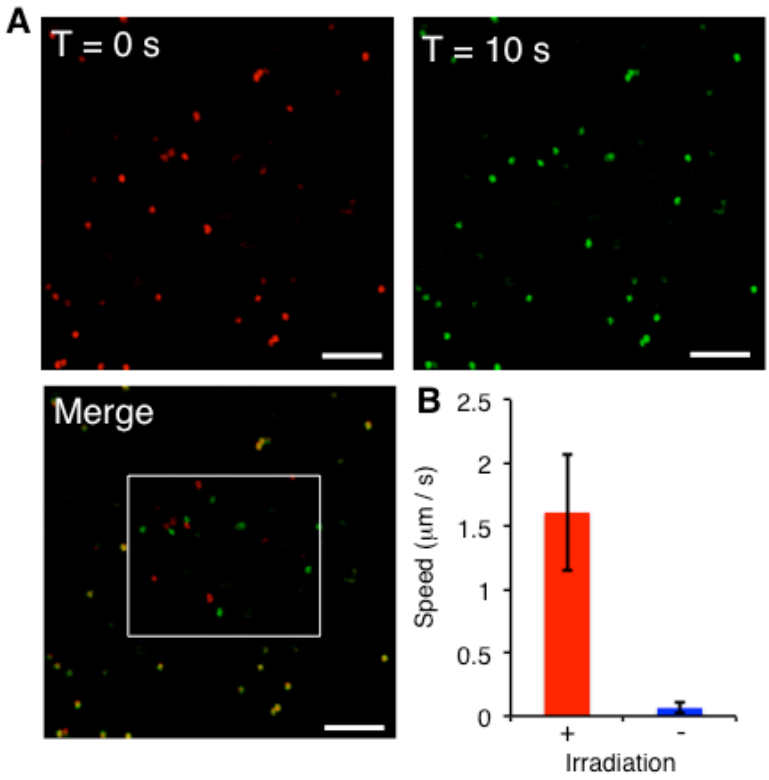

Figure 10. Controlling the local fluidity of DMACmoc-FF(CF_3) gel (0.075 wt%) by two-photon excitation evaluated by Brownian motion of nanobeads. (A) Time- lapse CLSM images of the fluorescent nanobeads (500 nm). The inset rectangle area shown in Merge panel was irradiated by focused laser light (740 nm). The fluorescence images were converted into pseudocolors (red: T = 0 s, green: T = 10 s) and merged. Scale bar is 5 μm. (B) Comparison of the mean speed of the Brownian motion of the nanobeads (500 nm) in the area with or without irradiation of two-photon excitation (740 nm).

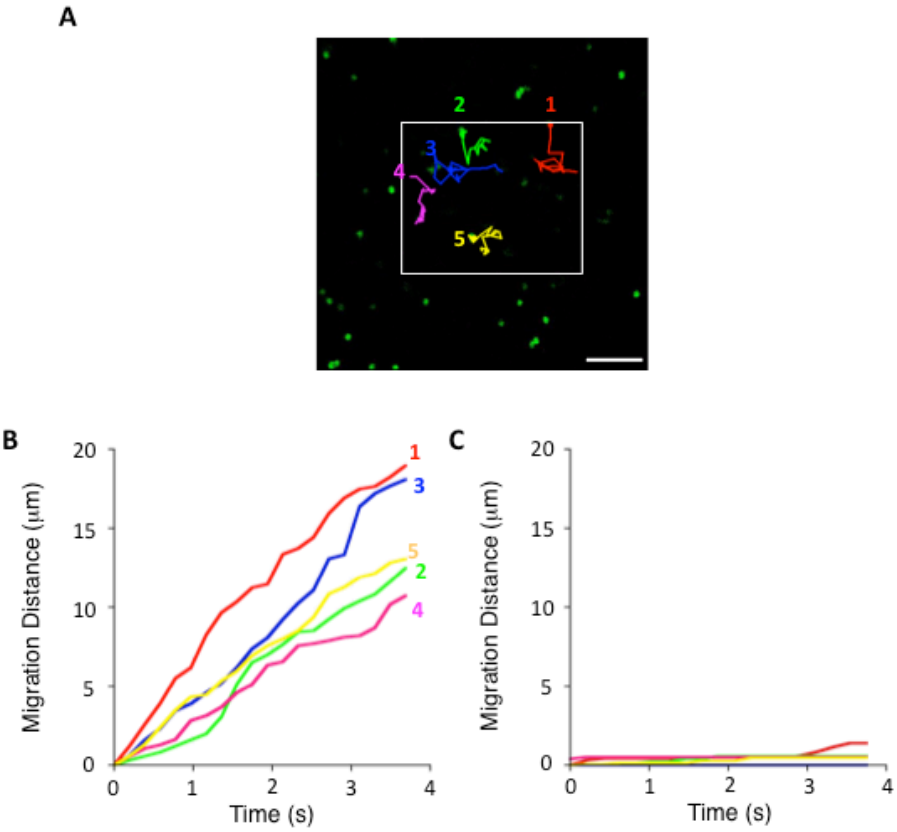

Figure 11. (A) Trace of the Brownian motion of 500 nm fluorescent nanobeads. Time courses of the accumulated migration distances of 500 nm fluorescent nanobeads (B) in the irradiated area and (C) unirradiated area in DMACmoc-FF(CF_3) gel.

2-2-6. Photo-manipulation of bacterial chemotaxis

Given the diameter of bacteria (250 nm-1000 nm) almost comparable to these beads, it might be reasonable to expect that a bacteria strain (*E. coli* RP437[17]) was encapsulated in DMACmoc-FF(CF_3) gel (0.075 wt%). CLSM observation confirmed that the chemotaxis of the bacteria stained with SYTO9 did not occur in the DMACmoc-FF(CF_3) gel (Figure 12), indicating that the nanomesh of the DMACmoc-FF(CF_3) gel is strong enough to become obstacles for the bacterial chemotaxis. Interestingly, we observed that bacteria in the NIR light irradiated area (740

nm, 3 W, 10%, 2 s) turned to motile state and moved in the limited micro-space (Figure 13). The rate of the bacterial chemotaxis was evaluated to be 6.6 ± 1.0 μm/s, which is comparable to the literature value[18]. In sharp contrast, one-photon UV light fabrication (405 nm, 30 mW) of DMACmoc-FF(CF_3) did not restore the chemotaxis of the entrapped bacteria (Figure 14), due to its high toxicity, which highlighted the advantage of two-photon excitation by NIR light over the one-photon for manipulating living materials.

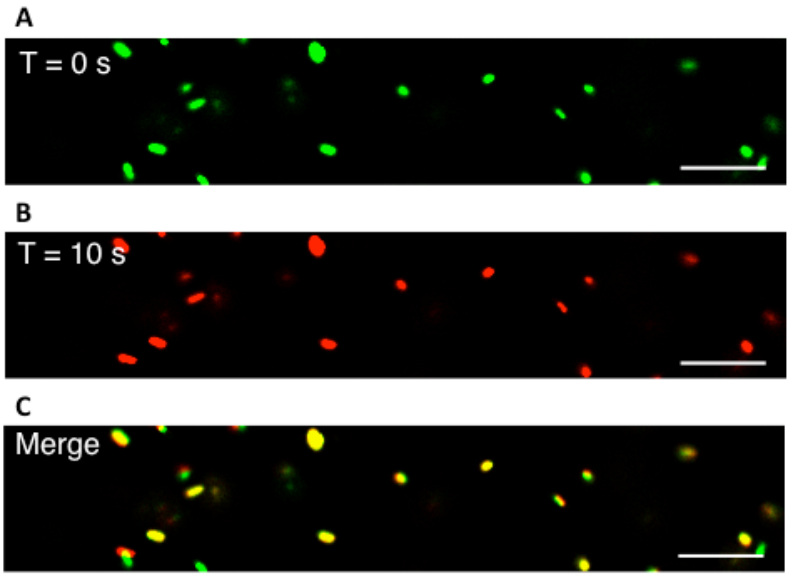

Figure 12. Time-lapse CLSM images of the SYTO9-labeled *E. coli* in DMACmoc-FF(CF_3). The fluorescence images were converted into pseudocolors (green: T = 0 s (A), red: T = 10 s (B)) and merged (C). Scale bar is 10 μm.

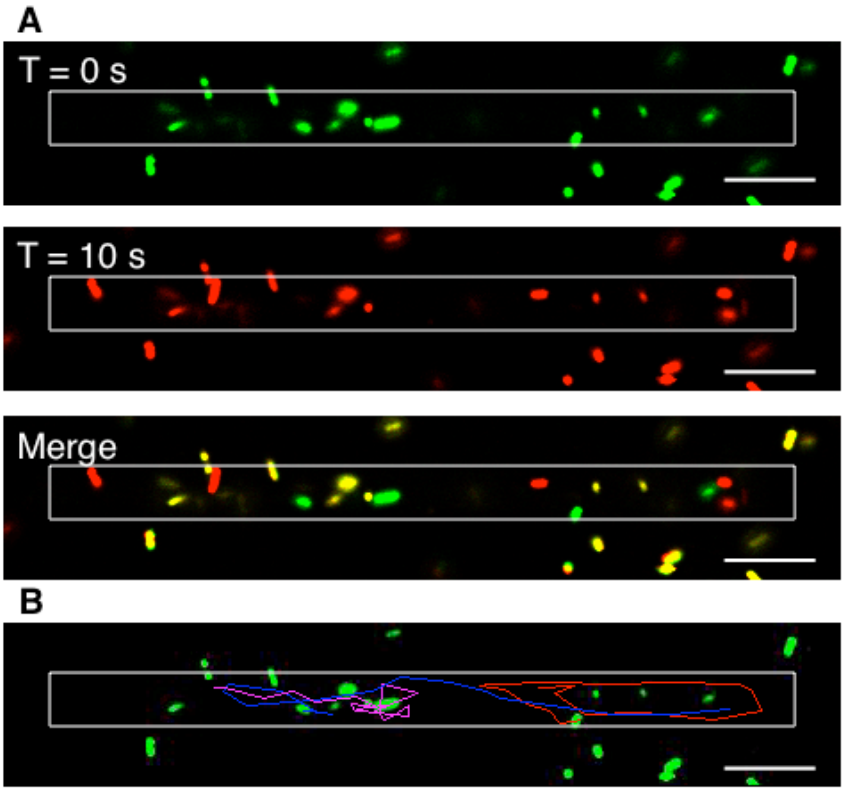

Figure 13. 3D spatial control of the chemotaxis of *E. coli* (RP437). (A) Time- lapse CLSM images of the SYTO9-labeled E. coli in DMACmoc-FF(CF_3) (0.075 wt%) gel. The inset rectangle area was irradiated by focused laser light (740 nm). The fluorescence images were converted into pseudocolors (green: T = 0 s, red: T = 10 s) and merged. (B) Three different tracks of each E. coli in the irradiation area shown in different colors. Scale bar is 10 μm.

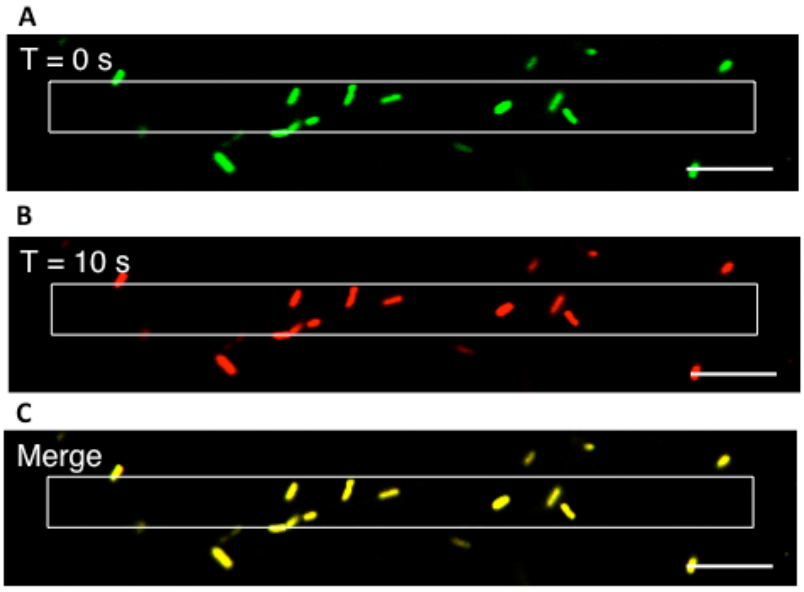

Figure 14. Time-lapse CLSM images of the SYTO9-labeled *E. coli*, in DMACmoc-FF(CF_3). The inset rectangle was irradiated by UV laser light (405 nm). The fluorescence images were converted into pseudocolors (green: T = 0 s (A), red: T = 10 s (B)) and merged (C). Scale bar is 10 μm.

2-3. Conclusion

In summary, I successfully developed the first two-photon responsive supramolecular hydrogel which can be readily fabricated by the two-photon NIR light excitation with high spatial resolution. By the benefit of the high biocompatibility of the two-photon NIR fabrication and the sufficient stiffness of the nanomeshes composed of the supramolecular fibers, the bacterial chemotaxis was remotely regulated in an Off-On mode. Present supramolecular material is potentially useful for defined cell culture matrix or controlled release in the deep tissue.

2-4. Experimental Section

Experimental generals:

Unless stated otherwise, all commercial reagents were used as received. Thin layer chromatography (TLC) was performed on silica gel $60F_{254}$(Merck). Column chromatography was performed on silica gel 60N (Kanto, 40–50 mm). Reverse phase HPLC (RP-HPLC) was conducted with a Hitachi Lachrom instrument equipped with YMC-pack Triart columns (250 mm × 4.6 mm I. D.). ^{1}H NMR spectra were obtained on a Varian Mercury 400 spectrometer with tetramethylsilane (TMS) or residual non-deuterated solvents as the internal references. Multiplicities are abbreviated as follows: s = singlet, d = doublet, t = triplet, q = quartet, m = multiplet, br = broad. ESI mass spectra were recorded using a Thermo Scientific Exactive mass spectrometer. The CD spectra were measured using a Jasco J-720WI spectropolarimeter. Elemental analysis was carried out using a Yanaco CHN coder MT-6 by the services at Kyoto University.

Hydrogel preparation:

Powder of DMACmoc-FF(CF_3) was suspended into 200 mM HEPES (pH 7.4) buffer. The suspension was heated until a homogeneous solution was obtained. The solution solidified into a hydrogel after standing for several hours at rt.

TEM observation:

Hydrogel (2 μL) was dropped on a copper TEM grid covered by an elastic carbon-support film (20–25 nm) with a filter paper underneath and the excess solution was blotted with the filter paper immediately. The TEM grid was dried under a reduced pressure overnight prior to TEM

observation. TEM images were acquired using a JEOL JEM-1400 (accelerating voltage: 80 kV) equipped with a CCD camera.

Rheological measurement of DMACmoc-FF(CF_3) gel:

Oscillatory experiments for the gel specimens with a diameter of 12 mm and a thickness of 0.9 mm were performed with a rheometer (RSA-G2, TA instrument) using compression mode at 25 ºC. Sample preparations were conducted as follows. The sol solutions (obtained by heating suspensions of gelator powders until the formation of homogeneous solutions and cooling to room temperature (rt)) were prepared in a vial after which the solution before gel formation (150 μL) was poured into a mold placed directly on the rheometer plate to prepare a disk-shaped gel. Storage and loss Young's moduli (E' and E'') are converted to the storage and loss shear moduli (G' and G'', respectively) using the relations of $G' = E'/3$ and $G'' = E''/3$ for incompressible materials like gels.

Photo-induced gel-sol transition of DMACmoc-FF(CF_3) gel:

A DMACmoc-FF(CF_3) gel (0.080 wt%, 200 mM HEPES (pH 7.4), 200 μL) in a quartz cell (10 mm × 2 mm) was irradiated with light from Hg lamp through a filter (wavelength cutoffs > 350 nm and < 370 nm) for at 25 ºC. The product was analyzed by RP-HPLC analysis with *p*-nitrobenzene sulfonamide as internal standard (YMC-Pack Triart columns (250 mm × 4.6 mm I. D.), wavelength of detection: 220 nm, eluent: A:B = 5:95-95:5 (A: acetonitrile/0.1%TFA, B: H_2O/0.1%TFA), linear gradient over 40 min, flow rate = 1.0 mL/min).

Two-photon fabrication of hydrogel:

Heat-dispersed gelator solution (20 μL) in 200 mM HEPES (pH 7.4) containing DEAC-gua (10 μM) was dropped onto a glass-bottom dish (Matsunami) and left at rest for 10 min at rt. The hydrogel was exposed to focused laser light using a two-photon confocal LSM (LSM 780, Zeiss) with a 740 nm laser (3W laser, ×40 objective (NA = 1.4, oil immersion), laser power = 10%). Zeiss Region of Interest (ROI) software was then used to draw and subsequently scan any arbitrary shape within an *x*-*y* plane of the gel. The results of the fabrication were also visualized with the LSM 780 by imaging the fluorescence of DEAC-gua.

Observation of Brownian motion of nanobeads in DMACmoc-FF(CF_3) gel :

Heat-dispersed gelator solutions (20 μL) in 200 mM HEPES (pH 7.4) containing 250, 500, or 1000 nm fluorescent nanobeads (Micromer-red F, POL) were dropped onto a glass-bottom dish (Matsunami) and left at rest for 10 min at rt. The Brownian motions of the beads inside the hydrogel were monitored by CLSM (Zeiss LSM780) at an excitation laser wavelength of 543 nm. Objective lens: ×40 (NA = 1.4, oil immersion) was used. I analyzed the locus and the accumulated distances of the beads movement every 0.49 s with a software (Move-tr/2D 7.0, Library).

Observation of bacteria entrapped in hydrogel:

An overnight culture of *Escherichia coli* RP437 cells grown in TB medium (1 mL, 1% Bacto-tryptone, 0.5% NaCl, (w/v)) at 30 ºC was centrifuged (5000 rpm for 10 min) at 4 ºC. The pellet was washed with PBS (1 mL × 2). The bacteria were suspended in PBS containing SYTO9 (10 μM, Molecular Probes) for fluorescence staining. After incubation at rt for 30 min, the suspension (2 μL) was mixed with a sol state of DMACmoc-FF(CF_3) (20 μL, in 200 mM HEPES

(pH 7.4)) on a glass-bottom dish (Matsunami). I observed the movement of the bacteria with CLSM (LSM780, Zeiss) and analyzed the locus and the accumulated distances of bacterial movement every 0.49 s (software Move-tr/2D 7.0, Library).

Synthesis

The typical procedure for the synthesis of hydrogelator DMACmoc-FF(CF_3) is shown in Scheme 1.

Scheme 1. Synthesis of hydrogelator DMACmoc-FF(CF_3)

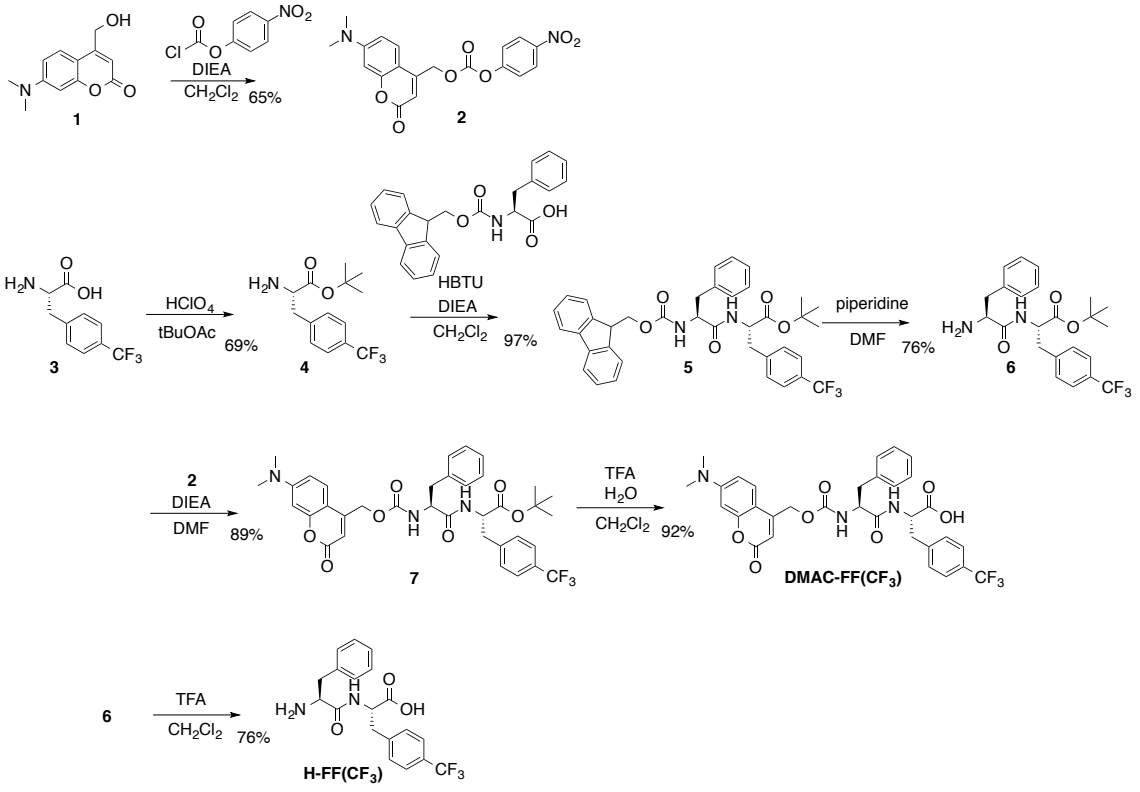

Synthesis of 2

To a stirred dry CH_2Cl_2 (140 mL) solution of **1** (2.3 g, 11 mmol, 1.0 equiv.) and *N*,*N*-diisopropylethylamine (DIEA) (7.3 mL, 42 mmol, 4.0 equiv.) was added dry CH_2Cl_2 (45 mL) solution of 4-nitrophenyl chloroformate (2.3 g, 12 mmol, 1.1 equiv.) dropwise in 30 min. The solution was stirred under Ar at rt for 2 h. Then a dry CH_2Cl_2 (45 mL) solution of 4-nitrophenyl chloroformate (2.3 g, 12 mmol 1.1 equiv.) was further added dropwise in 30 min to the reaction mixture. After stirring for 4 h, the mixture was washed with 5% citric acid aq. (200 mL × 2) and brine (100 mL). The organic layer was dried over anhydrous $MgSO_4$, and the solvent was removed by evaporation. The residue was purified by column chromatography (silica, $CHCl_3$:hexane = 5:1 to

$CHCl_3$:AcOEt = 20:1) to give **2** (2.71 g, 67%) as yellow solid. ^{1}H NMR (CD_3OD, 400 MHz, rt): δ = 3.08 (s, 6H), 5.42 (d, J = 1.2 Hz, 2H), 6.26 (s, 1H), 6.55 (d, J = 2.4 Hz, 1H), 6.64 (dd, J = 2.6 and 9.0 Hz, 1H), 7.34 (d, J = 8.8 Hz, 1H), 7.42 (dd, J = 2.2 and 7.0 Hz, 2H), 8.31 ppm (dd, J = 2.0 and 7.2 Hz, 2H).

Synthesis of 4

To a stirred *t*BuOAc (5.0 mL) solution of **3** (500 mg, 2.1 mmol) was added $HClO_4$ (60%, 0.35 mL). The mixture was stirred at rt for 12 h. To the mixture was added H_2O (10 mL) and 1 M HCl (6 mL). The residue was subsequently basified by adding 10% K_2CO_3 aq. The organic layer was extracted with CH_2Cl_2 (10 mL × 4). The collected organic layer was dried over anhydrous $MgSO_4$ and the solvent was evaporated to dryness to give **4** (430 mg, 69%) as colorless oil. ^{1}H NMR ($CDCl_3$, 400 MHz, rt): δ = 1.42 (s, 9H), 2.88-3.11 (m, 2H), 3.61-3.65 (m, 2H), 7.35 (d, J = 8.0 Hz, 2H), 7.56 ppm (d, J = 8.0 Hz, 2H).

Synthesis of 5

To a stirred CH_2Cl_2 (8 mL) solution of **4** (210 mg, 0.72 mmol, 1.2 equiv.), Fmoc-F-OH (234 mg, 0.60 mmol, 1.0 equiv.), DIEA (315 μL, 1.8 mmol, 3.0 equiv.), and *O*-(1H-benzotriazol-1-yl)-*N*,*N*,*N*',*N*'-tetramethyluronium hexafluorophosphate (HBTU) (275 mg, 0.72 mmol, 1.2 equiv.) was added. The mixture was stirred at rt for 2 h. The mixture was diluted with AcOEt (30 mL). The organic layer was washed with 5% citric acid aq. (30 mL × 3), sat. $NaHCO_3$ aq. (30 mL × 3), H_2O (30 mL × 3), and brine (30 mL). The organic layer was collected and dried over anhydrous Na_2SO_4, and the solvent was evaporated to dryness to give **5** (388 mg, 97%) as colorless oil. ^{1}H NMR ($CDCl_3$, 400 MHz, rt): δ = 1.35 (s, 9H), 2.98-3.15 (m, 4H), 4.17-4.49 (m, 4H), 5.22 (brs, 1H), 6.25 (brs, 1H), 7.15-7.36 (m, 9H), 7.38-7.42 (m, 2H), 7.47 (d, J =

8.0 Hz, 2H), 7.51-7.55 (m, 2H), 7.77 ppm (d, J = 7.6 Hz, 2H).

Synthesis of 6

To a stirred DMF (4 mL) solution of **5** (380 mg, 0.58 mmol) was added piperidine (1 mL) and the mixture was stirred at rt for 2 h. After removal of the solvent, the residue was purified by column chromatography (silica, $CHCl_3$:MeOH = 1:0-50:1) and washed with hexane to give **6** (173 mg, 68%) as white solid. ^{1}H NMR ($CDCl_3$, 400 MHz, rt): δ = 1.39 (s, 9H), 2.71-3.18 (m, 4H), 3.67-3.71 (m, 1H), 4.73-4.79 (m, 1H), 7.18-7.33 (m, 7H), 7.50 (d, J = 8.0 Hz, 2H), 7.73 ppm (d, J = 7.2 Hz, 1H).

Synthesis of 7

To a stirred dry DMF (5 mL) solution of **6** (170 mg, 0.39 mmol, 1.5 equiv.) was added DIEA (135 μL, 0.78 mmol, 3.0 equiv.) and **2** (100 mg, 0.26 mmol, 1.0 equiv.). The solution was stirred at rt for 12 h. The solvent was removed under reduced pressure and the residue was dissolved in CH_2Cl_2 (30 mL). The mixture was washed with sat. $NaHCO_3$ aq. (30 mL × 4), 5% citric acid aq. (30 mL), and brine (30 mL). The organic layer was dried over anhydrous $MgSO_4$ and the solvent was removed by evaporation. The residue was purified by column chromatography (silica, $CHCl_3$:AcOEt = 20:1). The residue was further purified by reprecipitation with diethyl ether to give **7** (158 mg, 89%) as yellow solid. ^{1}H NMR ($CDCl_3$, 400 MHz, rt): δ = 1.36 (s, 9H), 3.00-3.11 (m, 10H), 4.37-4.41 (m, 1H), 4.62-4.68 (m, 1H), 5.12-5.27 (m, 2H), 5.48 (brd, J = 7.6 Hz, 1H), 6.10 (s, 1H), 6.52 (d, J = 2.4 Hz, 1H), 6.59 (dd, J = 2.4, 8.8 Hz), 7.17-7.30 (m, 6H), 7.49 ppm (d, J = 7.6 Hz, 2H).

Synthesis of DMACmoc-FF(CF_3)

A mixture of **7** (150 mg, 0.22 mmol), H_2O (1 mL), and TFA (25 mL) in CH_2Cl_2 (75 mL) was

stirred at rt for 3 h. Toluene (100 mL) was then added to the mixture and the solvent was removed under reduced pressure. After azeotropy with toluene (2 mL × 3), the residue was washed with diisopropyl ether (30 mL × 3) to give DMACmoc-FF(CF_3) (126 mg, 92%) as yellow solid. ^{1}H NMR (DMSO-d_6, 400 MHz, rt): δ = 2.65-3.16 (m, 10H), 4.24-4.28 (m, 1H), 4.30-4.70 (m, 1H), 5.12(s, 2H), 5.93 (s, 2H), 6.55 (d, J = 2.4 Hz, 1H), 6.67 (dd, J = 2.4, 8.8 Hz, 1H), 7.22-7.30 (m, 2H), 7.38 (d, J = 8.8 Hz, 1H), 7.44 (d, J = 8.0 Hz, 2H). 7.59 (d, J = 8.4 Hz, 2H), 7.75 (d, J = 8.8 Hz, 1H), 8.38 ppm (d, J = 8.0 Hz, 1H). HR-FTMS (ESI): Calcd. for $[M(C_{32}H_{30}F_3N_3O_7)+H]^+$: m/z = 626.2109; Found: 626.2091. Anal. Calcd. for $C_{32}H_{30}F_3N_3O_7 \bullet (H_2O)_{0.5}$: C, 60.57; H, 4.92; N, 6.62; Found: C, 60.42; H, 4.84; N, 6.63 %.

Synthesis of H-FF(CF_3)

A mixture of **6** (30 mg, 69 μmol) and TFA (1 mL) in CH_2Cl_2 (2 mL) was stirred at rt for 3 h. The solvent was removed under reduced pressure. After azeotropy with toluene (2 mL × 3), the residue was washed with diethyl ether (10 mL) to give H-FF(CF_3) (26 mg, 76%) as yellow solid. ^{1}H NMR ($CDCl_3$, 400 MHz, rt): δ = 1.39 (s, 9H), 2.71-3.18 (m, 4H), 3.67-3.71 (m, 1H), 4.73-4.79 (m, 1H), 7.18-7.33 (m, 7H), 7.50 (d, J = 8.0 Hz, 2H), 7.73 ppm (d, J = 7.2 Hz, 1H). HR-FTMS (ESI): Calcd. for $[M(C_{19}H_{19}F_3N_2O_3 \bullet CF_3COOH)+H]^+$: m/z = 381.1421; Found: 381.1408. Anal. Calcd. for $C_{19}H_{19}F_3N_2O_3 \bullet CF_3COOH$: C, 51.02; H, 4.08; N, 5.67; Found: C, 50.91; H, 4.19; N, 5.49 %.

Data for other compounds are shown below.

DMACmoc-FL. ^{1}H NMR (DMSO-d_6, 400 MHz, rt): δ = 0.82-0.89 (m, 6H), 1.50-1.66 (m, 3H), 2.70-3.04 (m, 8H), 4.21-4.32 (m, 2H), 5.12(s, 2H), 5.94 (s, 1H), 6.54 (d, J = 2.4 Hz, 1H), 6.67 (dd, J = 2.4, 9.2 Hz, 1H), 7.14-7.40 (m, 6H), 7.73 (d, J = 8.8 Hz, 1H), 8.25 ppm (d, J = 8.0 Hz, 1H).

HR-FTMS (ESI): Calcd. for $[M(C_{28}H_{33}N_3O_7)+H]^+$: *m/z* = 524.2391; Found: 524.2385.

DMACmoc-FI. ^{1}H NMR (DMSO-d_6, 400 MHz, rt): δ = 0.81-0.86 (m, 6H), 1.18-1.22 (m, 1H), 1.38-1.42 (m, 1H), 1.79 (m, 1H), 2.75-3.05 (m, 8H), 4.20 (m, 1H), 4.38 (m, 1H), 5.13 (s, 2H), 5.93 (s, 1H), 6.55 (d, *J* = 2.4 Hz, 1H), 6.67 (dd, *J* = 2.4, 8.8 Hz, 1H), 7.14-7.31 (m, 5H), 7.39 (d, *J* = 8.8 Hz, 1H), 7.74 (d, *J* = 8.8 Hz, 1H), 8.08 ppm (d, *J* = 8.0 Hz, 1H). HR-FTMS (ESI): Calcd. for $[M(C_{28}H_{33}N_3O_7)+H]^+$: *m/z* = 524.2391; Found: 524.2384.

DMACmoc-FF. ^{1}H NMR (DMSO-d_6, 400 MHz, rt): δ = 1.26 (t, *J* = 7.0 Hz, 6H), 3.05-3.25 (m, 4H), 3.48 (q, *J* = 7.1 Hz, 4H), 4.72-4.79 (m, 2H), 6.50 (d, *J* = 2.4, 1H), 6.66 (dd, *J* = 2.4 and 9.0 Hz, 1H), 6.93-7.28 (m, 11H). 7.40 (d, *J* = 9.2 Hz, 1H), 8.48 (s, 1H), 9.21 ppm (d, *J* = 6.8, 1H). HR-FTMS (ESI): Calcd. for $[M(C_{31}H_{31}N_3O_7)+H]^+$: *m/z* = 558.2235; Found: 558.2230.

DMACmoc-GF. ^{1}H NMR (DMSO-d_6, 400 MHz, rt): δ = 2.83-3.05 (m, 8H), 3.57-3.67 (m, 2H), 4.40-4.43 (m, 1H), 5.22 (s, 2H), 6.01 (s, 1H), 6.56 (d, *J* = 2.4 Hz, 1H), 6.70 (d, *J* = 9.2 Hz, 1H), 7.17-7.26 (m, 5H), 7.46 (d, *J* = 9.2 Hz, 1H), 7.67 ppm (t, *J* = 6.0 Hz, 1H), 8.17 ppm(d, *J* = 8.4, 1H). HR-FTMS (ESI): Calcd. for $[M(C_{24}H_{25}N_3O_7)+H]^+$: *m/z* = 468.1765; Found: 468.1761.

DMACmoc-FG. ^{1}H NMR (DMSO-d_6, 400 MHz, rt): δ = 2.71-3.05 (m, 8H), 3.73-3.80 (m, 1H), 4.26-4.29 (m, 1H), 5.12 (s, 2H), 5.94 (s, 1H), 6.55 (d, *J* =2.8 Hz, 1H), 7.14-7.29 (m, 10H), 7.38 (d, *J* = 9.2 Hz, 1H), 7.80 (d, *J* = 9.2 Hz, 1H), 8.41 ppm (t, *J* = 5.6 Hz, 1H). HR-FTMS (ESI): Calcd. for $[M(C_{24}H_{25}N_3O_7)+H]^+$: *m/z* = 468.1765; Found: 468.1760.

DMACmoc-F(CF_3)F. ^{1}H NMR (DMSO-d_6, 400 MHz, rt): δ = 2.76-3.10 (m, 10H), 4.01-4.44 (m, 2H), 5.11 (s, 2H), 5.93 (s, 1H), 6.55 (d, *J* = 2.8 Hz, 1H), 6.68 (dd, *J* = 2.4, 9.2 Hz, 1H), 7.14-7.26 (m, 5H), 7.39 (d, *J* = 8.8 Hz, 1H), 7.49 (d, *J* = 8.0 Hz, 2H), 7.60 (d, *J* = 7.6 Hz, 2H), 7.81 (d, *J* = 8.4 Hz, 1H), 8.33 (brs, 1H), 12.74 ppm (brs, 1H). HR-FTMS (ESI): Calcd. for $[M(C_{32}H_{30}F_3N_3O_7)+H]^+$:

m/z = 626.2109; Found: 626.2098.

DMACmoc-F(CF$_3$)F(CF$_3$). ^{1}H NMR (DMSO-d_6, 400 MHz, rt): δ = 2.76-3.06 (m, 10H), 4.22-4.35 (m, 2H), 5.06-5.18 (m, 2H), 5.93 (s, 1H), 6.55 (d, *J* = 2.4 Hz, 1H), 6.68 (dd, *J* = 2.4, 9.2 Hz, 1H), 7.37-7.42 (m, 3H), 7.48 (d, *J* = 8.0 Hz, 2H), 7.56 (d, *J* = 8.0 Hz, 2H), 7.60 (d, *J* = 8.0 Hz, 2H), 7.86 (d, *J* = 8.0 Hz, 2H), 8.24 ppm (brs, 1H). HR-FTMS (ESI): Calcd. for [M($C_{33}H_{29}F_6N_3O_7$)+H]$^+$: *m/z* = 694.1982; Found: 693.1971.

DMACmoc-FFG. ^{1}H NMR (DMSO-d_6, 400 MHz, rt): δ = 2.64-2.70 (m, 1H), 2.78-2.84 (m, 1h), 2.93-3.06 (m, 8H), 3.71 (s, 2H), 4.02-4.26 (m, 1H), 4.52-4.60 (m, 1H), 5.11 (s, 2H), 5.93 (s, 1H), 6.55 (d, *J* = 2.4 Hz, 1H), 6.64 (d, *J* = 2.4, 8.8 Hz, 1H), 7.13-7.23 (m, 10H), 7.39 (d, *J* = 9.2 Hz, 1H), 7.69 (d, *J* = 9.2 Hz, 1H), 8.10-8.23 ppm (m, *2*H). HR-FTMS (ESI): Calcd. for [M($C_{33}H_{34}N_4O_8$)+H]$^+$: *m/z* = 615.2449; Found: 615.2441.

DMACmoc-LLL. ^{1}H NMR (DMSO-d_6, 400 MHz, rt): δ = 0.79-0.87 (m, 18H), 1.39-1.51 (m, 6H), 1.54-1.65 (m, 3H), 3.01 (s, 6H), 4.03-4.09 (m, 1H), 4.14-4.20 (m, 1H), 4.29-4.35 (m, 1H), 5.21 (s, 2H), 6.03 (s, 1H), 6.56 (d, *J* =2.4 Hz, 1H), 6.71 (dd, *J* = 2.4, 9.2 Hz, 1H), 7.45 (d, *J* = 9.2 Hz, 1H), 7.68 (d, *J* = 8.8 Hz, 1H), 7.93-7.98 ppm (m, 1H). HR-FTMS (ESI): Calcd. for [M($C_{31}H_{46}N_4O_8$)+H]$^+$: *m/z* = 603.3388; Found: 603.3376.

DMACmoc-VVV. ^{1}H NMR (DMSO-d_6, 400 MHz, rt): δ = 0.80-1.07 (m, 18H), 1.89-2.05 (m, 3H), 3.01 (s, 6H), 3.85-3.97 (m, 1H), 4.08-4.11 (m, 1H), 4.25-4.29 (m, 2H), 5.22 (s, 2H), 6.06 (s, 1H), 6.56 (d, *J* = 2.4 Hz, 1H), 6.71 (dd, *J* = 2.4, 9.2 Hz, 1H), 7.46 (d, *J* = 9.2 Hz, 1H), 7.64 (d, *J* = 8.8 Hz, 1H), 7.88 (d, *J* = 6.8 Hz, 1H), 12.49 ppm (brs, 1H). HR-FTMS (ESI): Calcd. for [M($C_{28}H_{40}N_4O_8$)+H]$^+$: *m/z* = 561.2919; Found: 561.2915.

DMACmoc-FFF. ^{1}H NMR (DMSO-d_6, 400 MHz, rt): δ = 2.60-3.08 (m, 12H), 4.20 (m, 1H), 4.45

(m, 1H), 4.56 (m, 1H), 5.10 (s, 2H), 5.92 (s, 1H), 6.55 (d, J = 2.4 Hz, 1H), 6.66 (dd, J = 2.8, 9.6 Hz, 1H), 7.12-7.27 (m, 15H), 7.37 (d, J = 9.6 Hz, 1H), 7.70 (d, J = 8.8 Hz, 1H), 8.13 (d, J = 8.0 Hz) 8.33 ppm (t, J = 8.0 Hz, 1H). HR-FTMS (ESI): Calcd. for $[M(C_{40}H_{40}N_4O_8)+H]^+$: m/z = 705.2919; Found: 705.2901.

DMACmoc-AAA. ^{1}H NMR (DMSO-d_6, 400 MHz, rt): δ = 1.18-1.25 (m, 18H), 3.01 (s, 6H), 4.05-4.09 (m, 1H), 4.12-4.18 (m, 1H), 4.25-4.30 (m, 1H), 5.21 (s, 2H), 6.04 (s, 1H), 6.56 (d, J = 2.4 Hz, 1H), 6.71 (dd, J = 2.4, 9.2 Hz, 1H), 7.46 (d, J = 8.8 Hz, 1H), 7.06 (d, J = 7.6 Hz, 1H), 7.97 (d, J = 7.6 Hz, 1H), 8.05 ppm (d, J = 6.8 Hz, 1H). HR-FTMS (ESI): Calcd. for $[M(C_{22}H_{28}N_4O_8)+H]^+$: m/z = 477.1980; Found: 477.1979.

DMACmoc-III. ^{1}H NMR (DMSO-d_6, 400 MHz, rt): δ = 0.75-0.83 (m, 18H), 1.05-1.41 (m, 6H), 1.61-1.80 (m, 3H), 3.01 (s, 6H), 3.93-3.98 (m, 1H), 4.05-4.15 (m, 1H), 4.22-4.29(m, 1H), 5.22 (s, 2H), 6.05 (s, 1H), 6.56 (d, J = 2.4 Hz, 1H), 6.71 (J = 2.4, 9.2 Hz, 1H), 7.46 (d, J = 9.2 Hz, 1H), 7.62 (d, J = 8.8 Hz, 1H), 8.86 ppm (m, 2H). HR-FTMS (ESI): Calcd. for $[M(C_{31}H_{46}N_4O_8)+H]^+$: m/z = 603.3388; Found: 603.3379.

References

(1) a) Estroff, L. A.; Hamilton, A. D. *Chem. Rev.* **2004**, *104*, 1201–1217. b) Hirst, A. R.; Escuder, B.; Miravet, J. F.; Smith, D. K. *Angew. Chem., Int. Ed.* **2008**, *47*, 8002–8018.

(2) a) Silva, G. A.; Czeisler, C.; Niece, K. L.; Beniash, E.; Harrington, D. A.; Kessler, J. A.; Stupp, S. I. *Science* **2004**, *303*, 1352–1355. b) Zhou, M.; Smith, A. M.; Das, K. A.; Hodson, N. W.; Collins, R. F.; Ulijn, R. V.; Gough, J. E. *Biomaterials* **2009**, *30*, 2523–2530.

(3) a) Boekhoven, J.; Koot, M.; Wezendonk, T. A.; Eelkema R.; van Esch, J. H. *J. Am. Chem. Soc.* **2012**, *134*, 12908–12911. b) Ikeda, M.; Ochi, R.; Wada A.; Hamachi, I. *Chem. Sci*. **2010**, *1*, 491. c) Li, J.; Kuang, Y.; Gao, Y.; Du, X.; Shi, J.; Xu, B. *J. Am. Chem. Soc.* **2012**, *135*, 542–545.

(4) a) Ikeda, M.; Ochi R.; Hamachi, I. *Lab Chip* **2010**, *10*, 3325–3334. b) Ikeda, M.; Yoshii, T.; Matsui, T.; Tanida, T.; Komatsu, H.; Hamachi, I. *J. Am. Chem. Soc*. **2011**, *133*, 1670–1673. c) Yang, Z.; Xu, B. *Chem. Commun*. **2004**, 2424–2425. d) Bhowmik, S.; Maitra, U. *Chem. Commun*. **2012**, *48*, 4624–4626.

(5) Tamaru, S.-i.;. Ikeda, M.; Shimizu, Y.; Matsumoto, S.; Takeuchi, S.; Hamachi, I. *Nat. Commun*. **2010**, *1*, 20, DOI: 10.1038/ ncomms1018.

(6) a) Dasgupta, A.; Mondal, J. H.; Das, D. RSC *Adv*. **2013**, *3*, 9117–9149. b) Moon, K.-S.; Kim, H.-J.; Lee, E.; Lee, M. *Angew. Chem., Int. Ed.* **2007**, *46*, 6807–6810. c) Bowenmen, C. J.; Nilsson. B. L. *J. Am. Chem. Soc.* **2010**, *132*, 9526–9527. d) Schneider, J. P.; Pochan, D. J.; Ozbas, B.; Rajagopal, K.; Pakstis, L.; Kretsinger, J. *J. Am. Chem. Soc.* **2002**, *124*, 15030–15037.

(7) a) Lutolf, M. P.; Hubbell, J. A. *Nat. Biotechnol*. **2005**, *23*, 47–55. b) Benoit, D. S. W.; Schwartz, M. P.; Durney, A. R.; Anseth, K. S. *Nat. Mater.* **2008**, *7*, 816–823. c) Huang, Z.; Lee, H.; Lee, E.; Kang, S.-K.; Nam, J.-M.; Lee, M. *Nat. Commun*. **2011**, *2*, 459, DOI: 10.1038/ ncomms1465.

(8) a) Matsumoto, S.; Yamaguchi, S.; Ueno, S.; Komatsu, H.; Ikeda, M.; Ishizuka, K.; Iko, Y.; Tabata, K. V.; Aoki, H.; Ito, S.; Noji, H.; Hamachi, I. *Chem. -Eur. J*. **2008**, *14*, 3977–3986. b) Komatsu, H.; Tsukiji, S.; Ikeda, M.; Hamachi, I. *Chem. -Asian J.* **2011**, *6*, 2368–2375. c) Matsumoto, S.; Yamaguchi, S.; Wada, A.; Matsui, T.; Ikeda, M.; Hamachi, I. *Chem. Commun*. **2008**, 1545–1517. d) He, I. M.; Li, J.; Tan, S.; Wang, R.; Zhang, Y. *J. Am. Chem. Soc*. **2013**, *135*, 18718–18721. e) Muraoka, T.; Koh, C. Y.; Cui, H. G.; Stupp, S. I. *Angew. Chem., Int. Ed*. **2009**, *48*, 5946–5949. f) Li, X. M.; Gao, Y.; Kuang, Y.; Xu, B. *Chem. Commun*. **2010**, *46*, 5364–5366. g) Haines, L. A.; Rajagopal, K.; Ozbas, B.; Salick, D. A.; Pochan, D. J.; Schneider, J. P. *J. Am. Chem. Soc.* **2005**, *127*, 17025–17029. h) Frkanec, L.; Jokic, M.; Makarevic, J.; Wolsperger, K.; Zinic, M. *J. Am. Chem. Soc.* **2002**, *124*, 9716–9717.

(9) Pawlicki, M.; Collins, H. A.; Denning, R. G.; Anderson, H. L. *Angew. Chem., Int. Ed*. **2009**, *48*, 3244–3266.

(10) a) Kloxin, A. M.; Kasko, A. M.; Salinas, C. N.; Anseth, K. S. *Science* **2009**, *324*, 59–63. (b) DeForest, C. A.; Anseth, K. S. *Nat. Chem.* **2011**, *3*, 925–932. (c) Tibbitt, M. W.; Kloxin, A. M.; Dyamenahallic, K. U.; Anseth, K. S. *Soft Matter*, **2010**, 6, 5100–5108. (d) Wosnick, J. H.; Shoichet, M. S. *Chem. Mater*. **2008**, *20*, 55–60. (e) Wylie, R. G.; Ahsan, S.; Aizawa, Y.; Maxwell, K. L.; Morshead C. M.; Shoichet, M. S. *Nat. Mater*. **2011**, *10*, 799–806.

(11) Ikeda, M.; Tanida, T.; Yoshii, T.; Hamachi, I. *Adv. Mater.* **2011**, *23*, 2819–2822.

(12) a) Furuta, T.; Wang, S. S.-H.; Dantzker, J. L.; Dore, T. M.; Bybee, W. J.; Callaway, E. M.; Denk, W.; Tsien, R. Y. *Proc. Natl. Acad. Sci. U.S.A.* **1999**, *96*, 1193–1200. (b) Geißler, D.; Antonenko, Y. N.; Schmidt, R.; Keller, S.; Krylova, O. O.; Wiesner, B.; Bendig, J.; Pohl, P.; Hagen, V. *Angew. Chem., Int. Ed*. **2005**, *44*, 1195–1198.

(13) a) Magar, M. E. *Biochemistry* **1968**, *7*, 617–620. (b) Greenfield, N. J.; Fasman, G. D. *Biochemistry* **1969**, *8*, 4108–4116.

(14) a) Aggeli, A.; Bell, M.; Boden, N.; Keen, J. N.; Knowles, P. F; McLeish, T. C. B. Pitkeathly, M.; Radford, S. E. *Nature* **1997**, *386*, 259–262. (b) Miao, X.; Cao, W.; Zheng, W.; Wang, J.; Zhang, X.; Gao, J.; Yang, C.; Kong, D.; Xu, H; Wang, L.; Yang Z. *Angew. Chem., Int. Ed.* **2012**, *51***,** 4388–4392.

(15) a) Mason, T. G.; Weitz, D. A. *Phys. Rev. Lett.* **1995**, *74*, 1250–1253. (b) Crocker, J. C.; Valentine, M. T.; Weeks, E. R.; Gisler, T.; Kaplan, P. D.; Yodh, A. G.; Weitz, D. A. *Phys. Rev. Lett*. **2000**, *85*, 888–891. (c) Nowak, A. P.; Breedveld, V.; Pakstis, L.; Ozbas, B.; Pine, D. J.; Pochan, D. J.; Deming, T. J. *Nature* **2002**, *417*, 424–428.

(16) *CRC Handbook of Chemistry and Physics*, 93rd ed. (Ed.: W. M. Haynes), CRC, Boca Raton, FL, 2012.

(17) Y. Asai, T. Yakushi, I. Kawagishi, M. Homma, *J. Mol. Biol.* **2003**, *327*, 453–463. b) J. S. Parkinson, S. E. Houts, *J. Bacteriol.* **1982**, *151*, 106–113.

(18) Alon, U.; Camarena, L.; Surette, M. G.; Arcas, B. A.; Liu, Y.; Leibler, S.; Stock, J. B. *EMBO J.* **1998**, *17*, 4238–4248.

Chapter 3

Reversible Assembly/Disassembly of Nanoprobes for Turn-on Fluorescent Imaging of Endogenous Proteins in Live Cells

Abstract

Supramolecular nanomaterials responsive to specific intracellular proteins should be greatly promising for protein sensing and imaging, controlled drug release or dynamic regulation of cellular processes in living cells. However, valid design strategies to create functional supramolecules are poorly developed. Herein, I describe the reversible disassembly/self-assembly of fluorescent ligand-tethered nanoprobes that can be controlled by selective ligand-protein recognition in live cells. The probe self-assembled into nanoaggregates in the "signal-off" mode in the absence of target protein while disassembly was induced in its presence to "turn-on" the fluorescence signal. Using the supramolecular nanoprobe, I specifically visualized endogenously expressed human carbonic anhydrase and heat shock protein 90 inside living mammalian cells. The intracellular reversibility of the supramolecular probes allowed us to construct an imaging-based inhibitor assay system for these proteins in live cells, highlighting the potential of reversible/dynamic supramolecules as novel intelligent biomaterials.

3-1. Introduction

Proteins are involved in all biological events, and as such, their localization, expression level and functions are dynamically regulated in live cells.[1] Therefore, protein-responsive materials should hold promise for specific protein sensing, live imaging, controlled drug release, and regulation of cellular processes.[2] The use of supramolecular nanomaterials in response to selective proteins in live cells is attractive owing to their dynamic reversibility and potentially high biodegradability.[3] Cell surface proteins as therapeutic and/or diagnostic biomarkers are easiliy accessible for synthetic biomaterials and thus many promising nanomaterials have been developed.[4] In contrast, intracellular proteins are known to be extremely difficult to target and the development of supramolecular nanomaterials that are responsive to "intracellular proteins" remains challenging. There are various obstacles that must be overcome for nanomaterials to be workable inside living cells, including sufficient cell permeability through biomembranes, high target protein specificity under crude intracellular conditions, and effective switching functions that are operatable inside live cells. As pioneering works, enzymatic reaction-triggered self-assembling nanostructures that function inside living cells have been reported by Rao et al., in which an intracellular protease intiates the deprotection reaction of precursor molecules to yield covalently linked fluorescent oligomers.[5] Xu et al. have succeeded in the formation of phosphatase-triggered supramolecular hydrogels in live cells, demonstrating their use in an activity assay for the cytosolic enzyme.[6] Aggregation-induced emission resulting in a turn-on fluorescence in response to a target enzyme was also recently applied to specific protein sensing in live cells.[7] Although these examples indicate the successful formation of supramolecular nanostructures in living cells, reversible self-assembly/disassembly of such materials has never been achieved. Reversible

self-assembly/disassembly would be a desirable feature of supramolecular nanomaterials, and could lead to various applications including dynamic protein seinsing in response to the expression level or protein-triggered intracellular drug release.

Hamachi et al. recently developed a disassembly-driven turn-on nanoprobe, where the ligand-tethered fluorophores exhibited unique self-assembling features and showed a reversible turn-on fluorescent change toward non-enzymatic-proteins on a live cell surface, as well as toward purified ones in a test tube.[8] Furthermore, Dr. Mizusawa in Hamachi group succeeded in fluorescently visualizing overexpressed dihydrofolate reductase (eDHFR) in living cell by disassembly-driven turn-on nanoprobe **1** (Figure 1). This probe **1** is composed of the following four modules: (i) methotrexate (MTX) as a hydrophilic ligand for targeting eDHFR, (ii) tetramethylrhodamine (TMR) as a fluorophore for imaging, (iii) phenylalanine as a hydrophobic module for finely tuning the aggregation property, and (iv) a relatively hydrophobic linker for connecting these modules (Figure 1b).[8d] The probe **1** formed spherical or oval aggregates with a mean diameter of 40 nm, the fluorescence of which was greatly suppressed owing to self-aggregation and was enhanced by 37-fold upon addition of purified eDHFR in a test tube. Moreover, using overexpressed eDHFR in mammalian cells as proof-of-principle experiment, it was revealed that (1) the nanoprobe can be incorporated into the inside cells by an endocytosis mechanism, and (2) self-assembly/disassembly of the probe indeed occurred reversibly in living cells upon a specific ligand-protein recognition

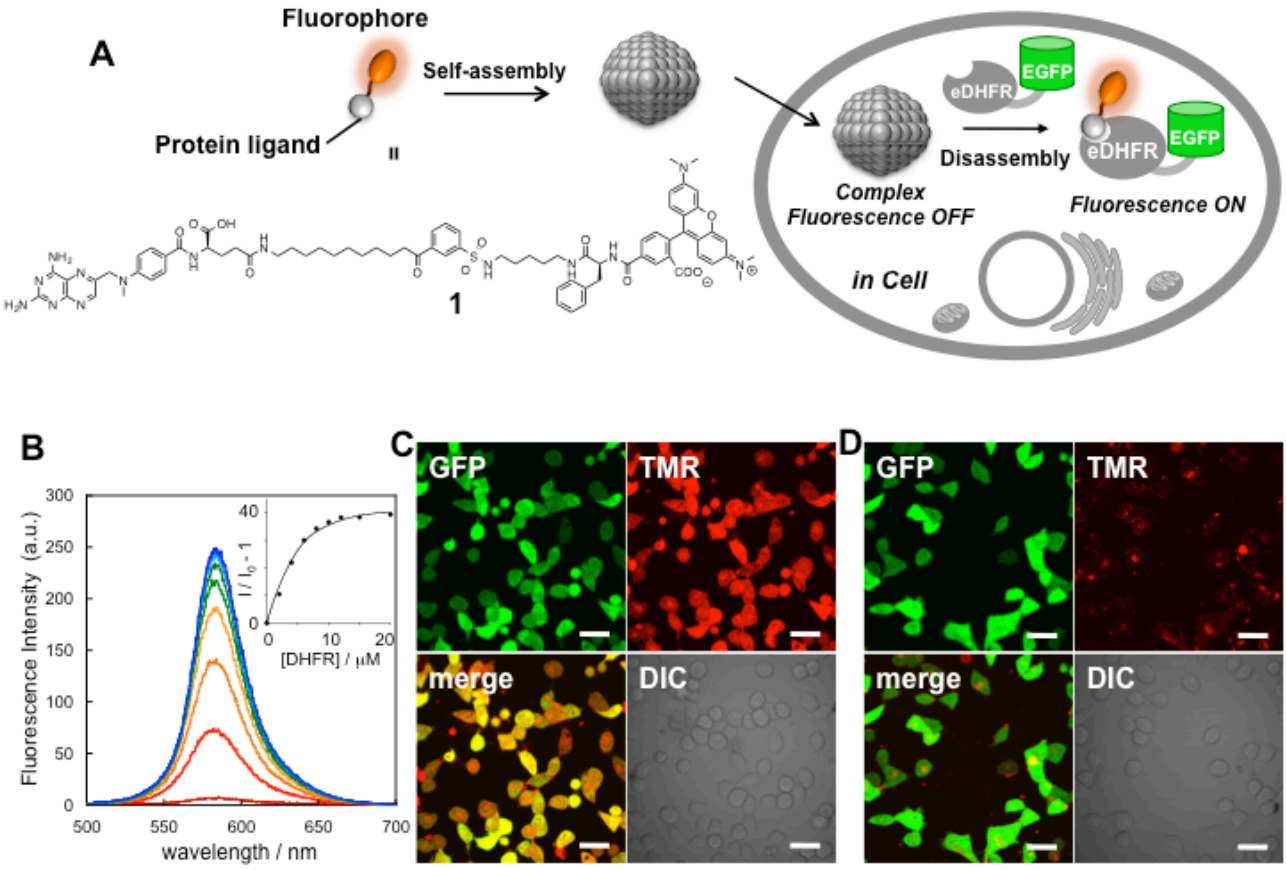

Figure 1. (**A**) Schematic illustration of in cell eDHFR imagiing by self-assembling turn-on nanoprobe. (**B**) Fluorescence spectra changes of probe **1** (10 μM) upon addition of eDHFR (0−20 μM) (λ_{ex} = 480 nm). (Inset) Fluorescence titration curve (λ_{em} = 584 nm). (**C**, **D**) CLSM images of HeLa-DG cells treated with probe **1** (2 μM) for 12 h at 37°C in cultured media (**C**) or after addition of TMP (10 μM) (**D**). Scale bars, 20 μm.

Herein, I sought to extend this strategy of the self-assembling nanoprobe to achieve intracellular imaging of "endogeneously" expressed proteins such as human carbonic anhydrase (hCAII) and heat shock protein 90 (HSP90) with turn-on manner (Figure 2). Moreover, imaging-based inhibitor assay for these endogenous proteins using live cells was successfully constructed, clearly highlighting the advantage of incorporating a reversible assembly/disassembly function in the design of sophisticated supramolecular biomaterials.

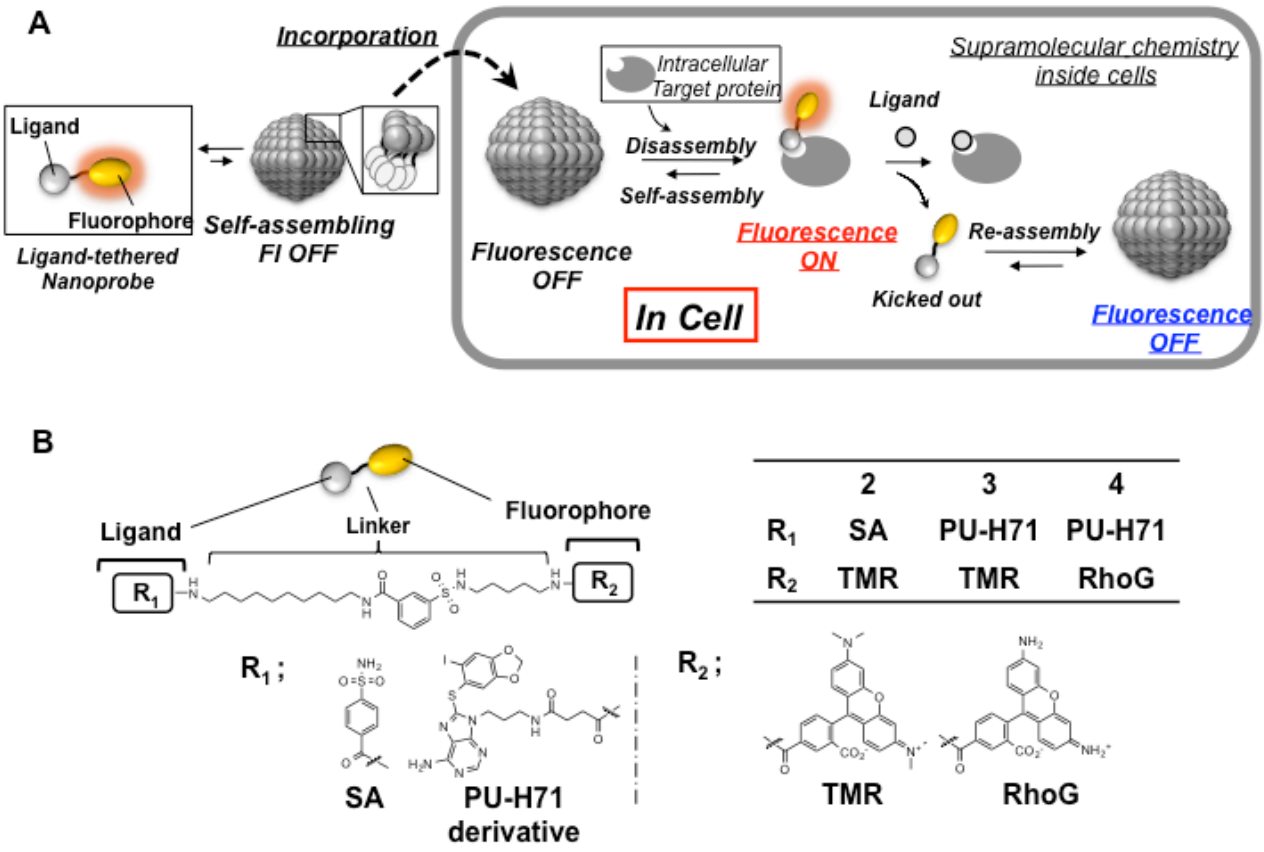

Figure 2. (**A**) Schematic illustration of in cell reversible protein sensing by self-assembling turn-on nanoprobe. (B) Chemical structures of ligand-tethered nanoprobes for intracellular hCAII and HSP90 imaging: **2** for hCAII and **3**, **4** for HSP90.

3-2. Result and Discussion

3-2-1. Imaging of endogeneous hCAII in MCF-7 cells.

Cytosolic hCAII, a protein related to various diseases such as epilepsia or glaucoma was selected as the target. Using the same design strategy as the eDHFR probe, a TMR-tethered probe **2** carrying a benzenesulfonamide ligand, a selective inhibitor of the hCA family, [9] was prepared (Figure 2B). Atomic force microscopy (AFM) or dynamic light scattering (DLS) data revealed the formation of spherical or oval aggregates of **2** with a mean diameter of 100 nm in aqueous buffer

(Figure 3C, D). We also confirmed that probe **2** showed a 30-fold increase in the fluorescent intensity in response to purified hCAII in a test tube (Figure 3A, B). Imaging of endogenous hCAII in live MCF7 cells, a human breast cancer cell line naturally expressing hCAII, was then conducted using probe **2**. When **2** was mixed with MCF7 cells, followed by incubation for 4 h at 37°C, strong fluorescence from TMR was observed in the cytosol region including the nucleus by CLSM (Figure 4A). The strong fluorescence inside the cells dramatically decreased upon addition of ethoxazolamide (EZA) (Figure 4B), an hCAII inhibitor,[9] implying that the selective ligand-hCAII recognition was cruicial for the turn-on imaging, similar to the above-mentioned nanoprobe **1**. These results demonstrated that an endogenously expressed intracellular protein can be visualized by our disassembly-driven turn-on nanoprobe.

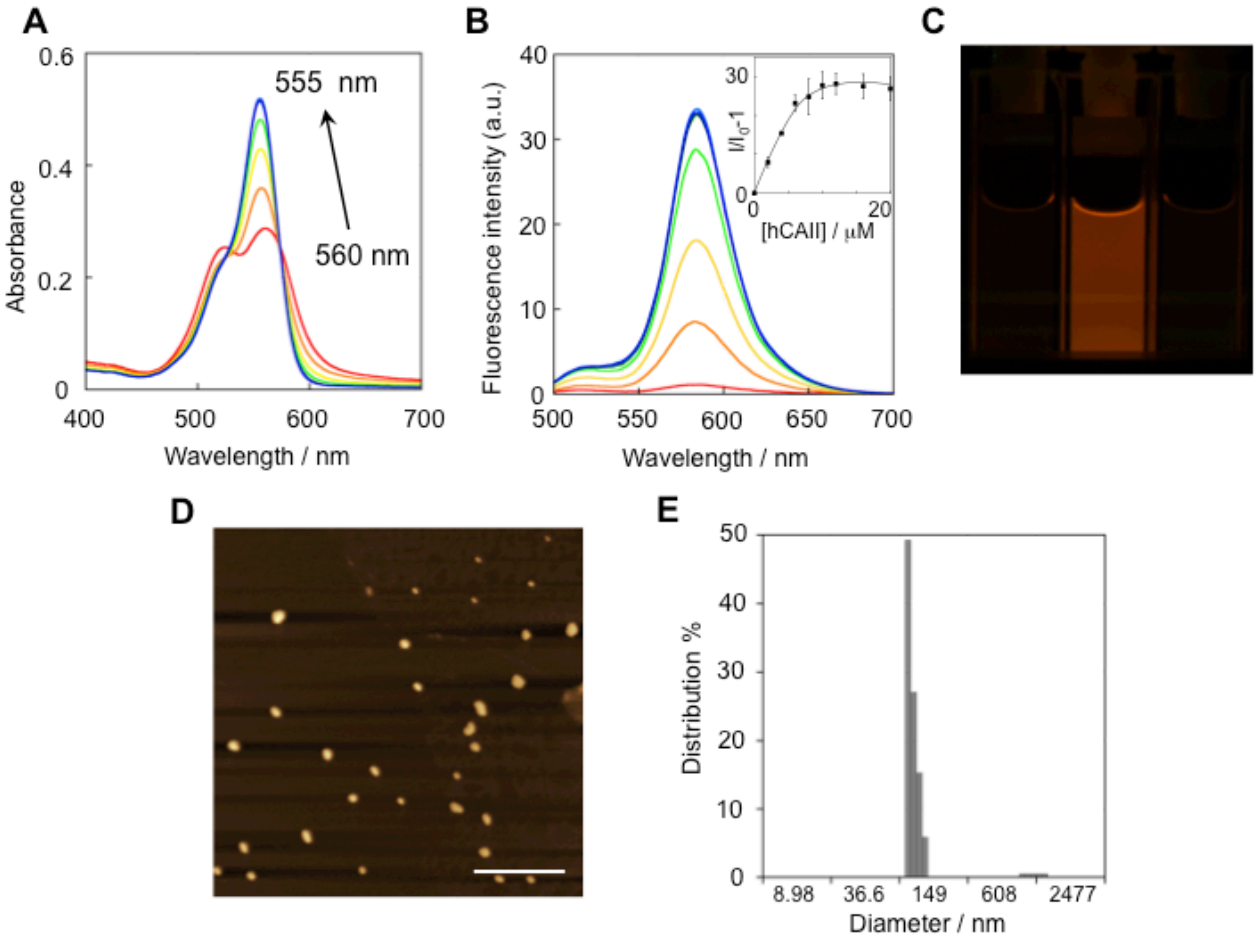

Figure 3. (**A**) UV–vis absorbtion spectral changes of probe **2** (10 μM) upon addition of hCAII (0−20 μM) in 50 mM HEPES buffer (pH 7.2, 150 mM NaCl). (**B**) Fluorescence spectra change of probe **2** (10 μM) upon addition of purified hCAII (0-20 μM) (λ_{ex} = 480 nm) in 50 mM HEPES buffer (pH 7.2, 150 mM NaCl). (Inset) The relative fluorescence intensity change was plotted with the concentration of hCAII. The experiments were performed in triplicate to obtain mean and standard deviation values (shown as error bars). (**C**) Photographs of probe **2** (10 μM) in the absence (left) and presence (middle) of hCAII (20 μM), and after addition of EZA (100 μM) to the solution of **2** and hCAII (right). (**D**) AFM image of probe **2** (2 μM) in 50 mM HEPES buffer (pH 7.2, 150 mM NaCl). (**E**) DLS analysis of probe **2** (2 μM) only in 50 mM HEPES buffer (pH 7.2, 150 mM NaCl).

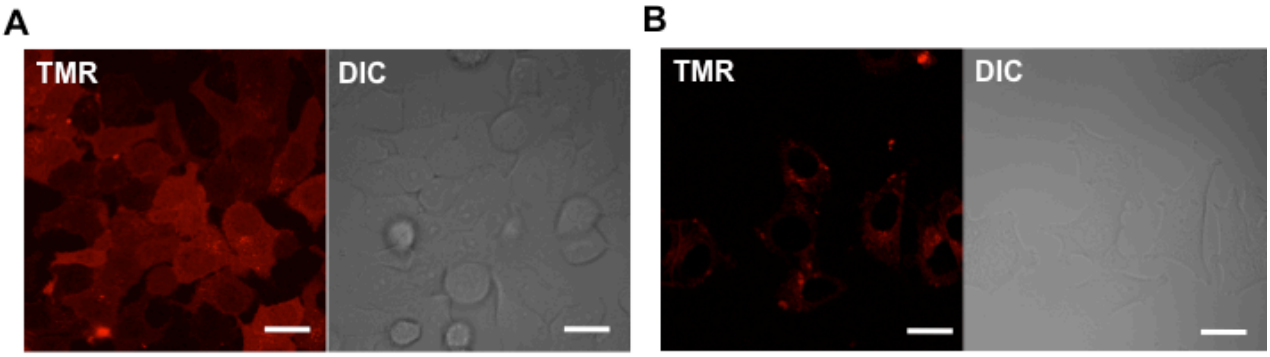

Figure 4. CLSM images of MCF7 cells treated with probe **2** (100 nM) for 4 h at 37°C in cultured media in the absence (**A**) or presence (**B**) of EZA (100 μM). Scale bars, 20 μm.

3-2-2. hCAII inhibitor assay in MCF-7 cells

Owing to the reversible properties in living cells, a unique imaging-based inhibitor screening was next constructed using **2**. After staining with **2**, the MCF7 cells were incubated with an hCAII inhibitor such as EZA, acetazolamide (AAZ) or 4-sulfamoylbenzoic acid (SBA), followed by fluorescence monitoring by CLSM. When the strong inhibitor EZA was added, a significant decrease in the fluorescent intensity of the intracellular region was induced, which saturated in the nM concentration range as shown in Figure 5A. In contrast, no substantial change was observed by addition of 0.1 mM of *p*-toluenesulfonic acid (TSA), which has negligible affinity for the CA family (Figure 5D). I prepared the titration curve on the basis of the CLSM imaging changes, giving IC_{50} values (half maximal inhibitory concentration of fluorescence intensity change), of 9.9×10^{-9} M for EZA, 2.7×10^{-8} M for AAZ and 1.3×10^{-6} M for SBA, respectively (Figure 5B, C, D, F,). The literature values (K_i) determined by using purified hCAII were reported to be 8×10^{-9} M (EZA), 1.2×10^{-8} M (AAZ) and 2.6×10^{-7} M (SBA).[9,10] While these K_i values for EZA or AAZ were almost the same as those obtained from our cell-based assay, the value for SBA was clearly different. This

may be attributed to the fact that our method evaluated the lower cell-permeability and/or the lower in-cell selectivity of SBA, together with the simple affinity to CA, implying that the present cell-based inhibitor assays allow us to estimate the drug potencies under more real conditions. More importantly, these results strongly suggested that the reversible self-assembly/disassembly phenomenon of the supramolecular nanoprobes is powerful for sensing dynamic ligand/protein interactions, an essential function of endogenous proteins, even in the interior of living cells.

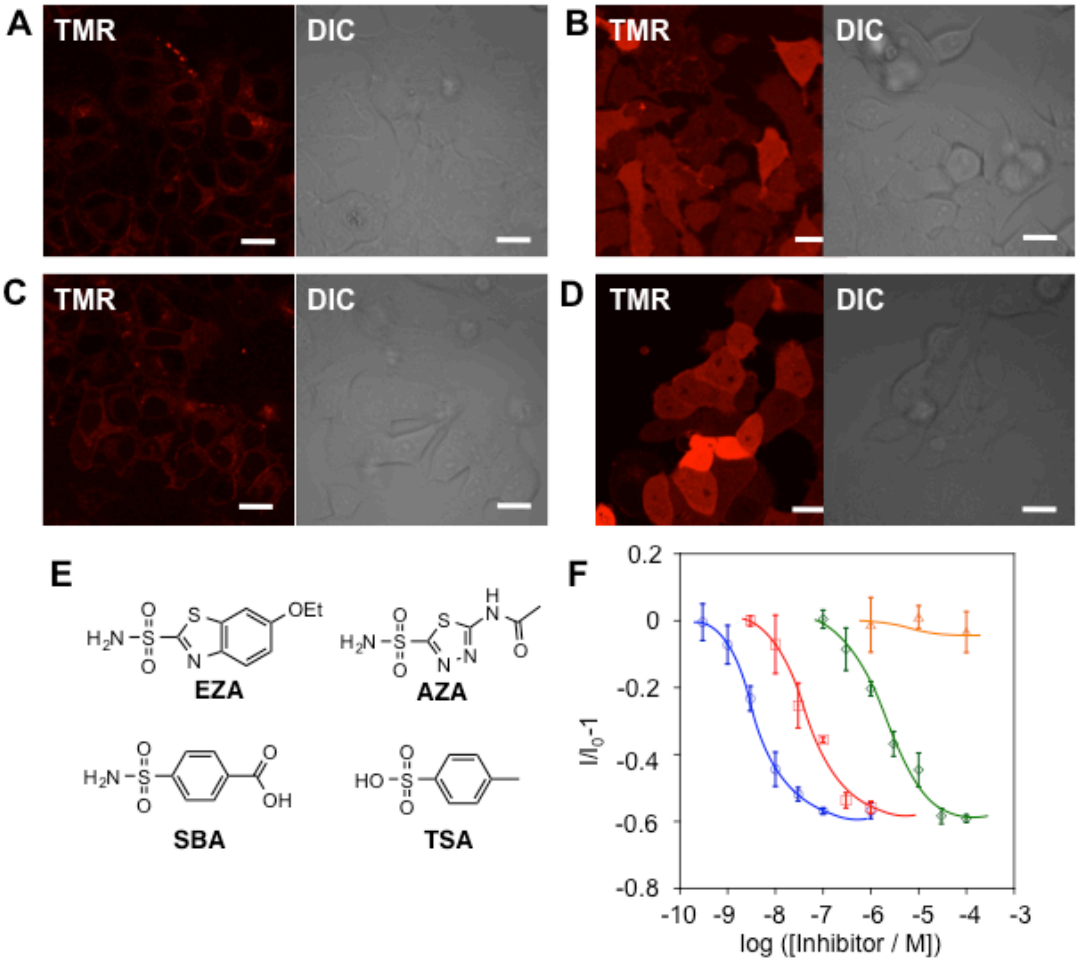

Figure 5. Imaging-based hCAII inhibitor assay with probe **2**. (**A**-**D**) Fluorescence images of MCF7 cells treated with probe **2** (100 nM) in the presence of hCAII inhibitors [(**A**) EZA (10 nM), (**B**) AAZ (10 nM), (**C**) AAZ (300 nM) and (**D**) SBA (1 μM)]. Scale bars, 20 μm. (**E**) Chemical structures of inhibitors for hCAII used in this study. EZA is 6-ethoxy-2-benzothiazolesulfonamide, AAZ is acetazolamide, SBA is 4-sulfamoylbenzoic acid, and TSA is 4-toluenesulfonic acid. (**F**) Fluorescence titration profile of the relative change in fluorescence intensity ($I/I_0 - 1$) from the intracellular region vs inhibitor concentration for EZA (○, blue), AAZ (□, red), SBA (◇, green) and non-inhibitor TSA (△, orange). Fluorescence intensities were evaluated at 10 cells in 5 regions in each dish, and the experiments were performed in triplicate to obtain mean and standard error values (shown as error bars).

3-2-3. Hsp90 imaging and inhibitor assay in SK-BR-3

Benefiting from the modular design, a self-assembling fluorescence turn-on nanoprobe was constructed by replacing the ligand part for another endogenously expressed intracellular protein, HSP90, a well-known tumor biomarker and valuable drug target for cancer diagnostics and treatment.[11] TMR-tethered probe **3** (λ_{em} = 585 nm) carrying PU-H71 as a ligand, a selective inhibitor of HSP90, was designed (Figure 2B).[12] It showed a 32-fold increase in fluorescent intensity by addition of the N-terminal ATP-binding domain of HSP90 (HSP90-N) (Figure 6A–C).[13] I then sought to fluorescently image endogenous HSP90 in live SK-BR-3 cells, a human breast cancer cell line,[14] using probe **3**. When probe **3** was mixed with SK-BR-3 cells, strong TMR fluorescence was detected in the cytosol area of SK-BR-3 cells by CLSM observation (Figure 7A). This image was almost identical to that of the immunostaining pattern obtained using an anti-HSP90 antibody. The fluorescence intensity inside the cells was substantially decreased upon addition of PU-H71 (Figure 7B), suggesting that **3** was kicked out of the HSP90 binding pocket and re-assembled into nano-aggregates, similar to probe **1** (for over-expressed eDHFR) and **2** (for endogenous hCAII). The titration curves for several HSP90 inhibitors were obtained, allowing the determination of the IC50 values 2.1×10^{-6} M for PU-H71 and 8.1×10^{-6} M for MPC3100 (Figure 7D). In contrast, no substantial change was observed upon addition of 10 mM of geldanamycin, an another inhibitor for HSP90. To date, various HSP90 inhibitors have been developed as anti-cancer agents, the potencies of which (typically as IC50 values) were examined by an indirect phenotype assay, such as via tumor cell growth inhibition (the reported values are 5×10^{-8} M for PU-H71,[12a] 6×10^{-8} M for MPC-3100[15] and 2×10^{-9} M for geldanamycin,[16] respectively). To the best of our knowledge, the results described herein provide affinity values for HSP90 inhibitors toward active

HSP90 in living cells for the first time. Ultimately, this methodology should prove helpful for direct drug discovery applications in the future. Moreover, it is likely that these reversible self-assembling nanoprobes can be adapted for use in fluorescently visualizing a number of intracellular protein functions by varying the ligand and fluorophore.

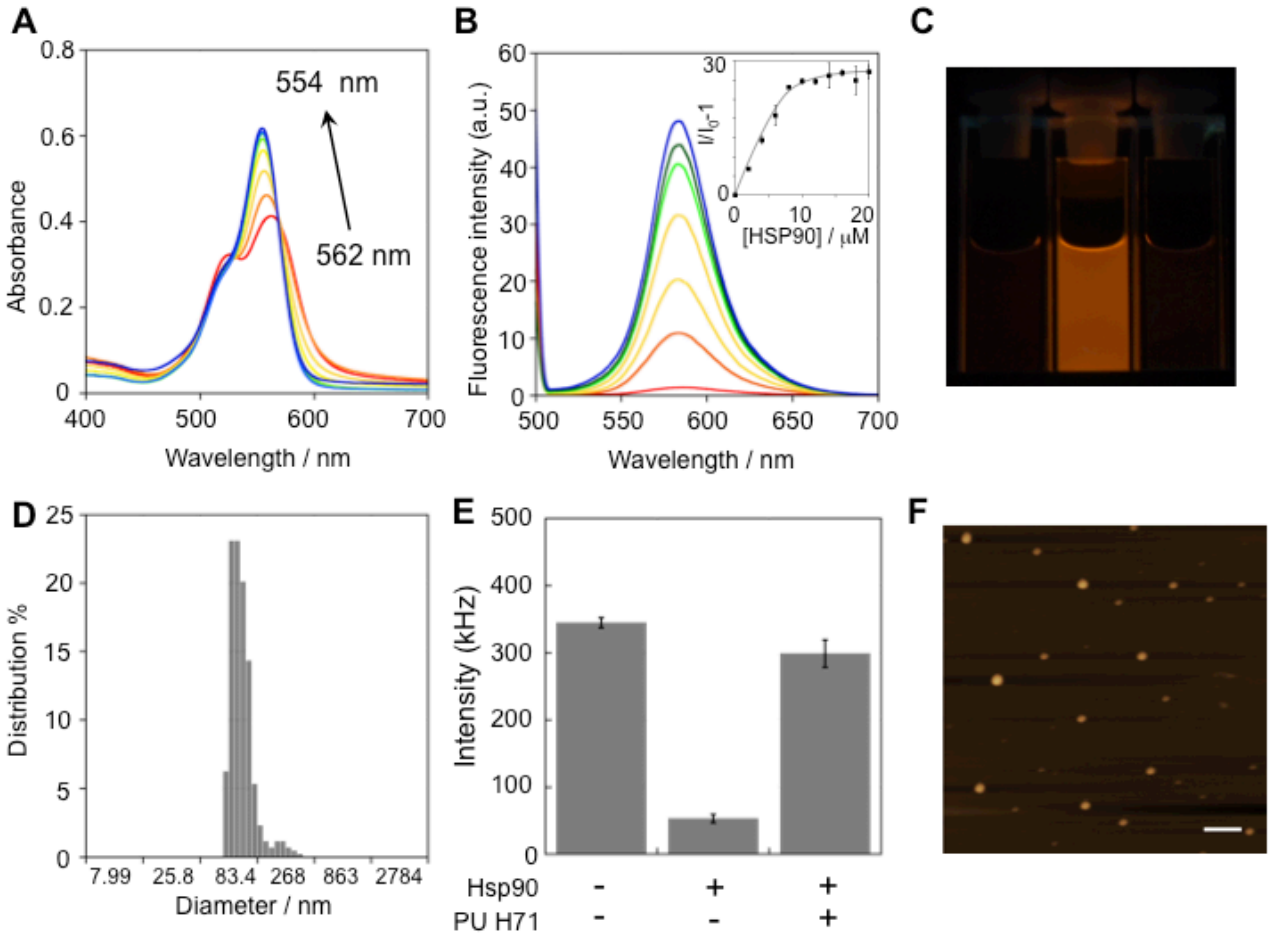

Figure 6. UV–vis absorbtion spectral changes of probe **3** (10 μM) upon addition of HSP90-N (0−20 μM) in 50 mM HEPES buffer (pH 7.2, 150 mM NaCl). (**B**) Fluorescence spectra change of probe **3** (10 μM) upon addition of purified HSP90-N (0-20 μM) (λ_{ex} = 480 nm) in 50 mM HEPES buffer. (Inset) Fluorescence titration curve of probe **3** upon addition of HSP90-N (0-20 μM) (λ_{em} = 585 nm). (**C**) Photographs of probe **3** (10 μM) in the absence or presence of HSP90-N (20 μM, left or middle, respectively), and after addition of PU-H71 (100 μM) to the solution of **3** and HSP90-N (right). (**D**) DLS analysis of probe **3** only (5 μM) in 50 mM HEPES buffer (pH 7.2). (**E**) Scattering intensity of probe **3** (5 μM) in the absence (left) and presence (middle) of Hsp90-N (10 μM) and after addition of PU-H71 (100 μM) to the solution of **3** and Hsp90-N (right). (**F**) AFM image of probe **3** (2 μM) in 50 mM HEPES buffer.

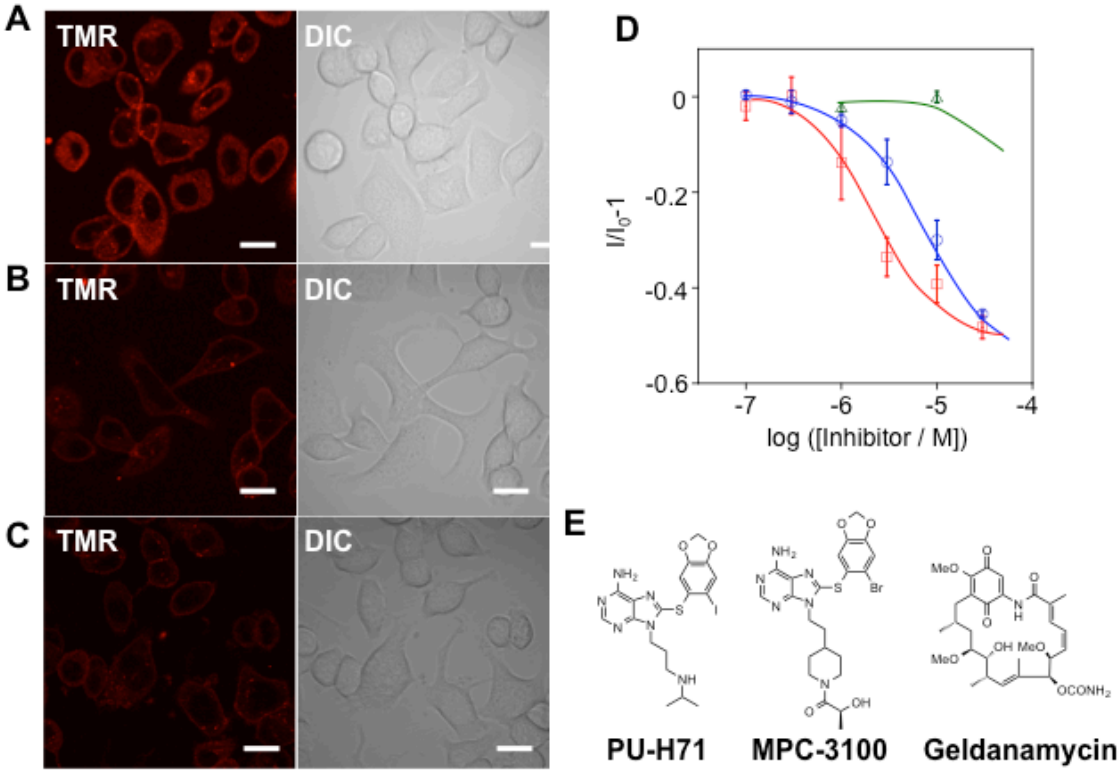

Figure 7. (**A**-**C**) CLSM images of SK-BR-3 cells treated with probe **3** (100 nM) for 12 h at 37°C in cultured media (**A**) or after addition of PU-H71 (**B**, 10 μM) or MPC3100 (**C**, 30 μM). Scale bars, 20 μm. (**D**) Fluorescence titration profile of the relative change in fluorescence intensity ($I/I_0 - 1$) from the intracellular region vs inhibitor concentration for PU-H71 (□, red), MPC-3100 (○, blue) and Geldanamycin (△, green). Fluorescence intensities were evaluated at 10 cells in 5 regions in each dish, and the experiments were performed in triplicate to obtain mean and standard error values (shown as error bars). (**E**) Chemical structures of HSP90 inhibitors used in this study.

In addition to **3**, another turn-on probe **4** was also synthesized by replacing TMR with rhodamine-green (RhoG), which emitted a distinct color (λ_{em} = 530 nm) enhancing the fluorescence intensity by 350-fold in response to HSP90-N (Figure 8). An almost identical imaging pattern at a different emission wavelength was obtained using probe **4** (Figure 9A). The fluorescence intensity inside the cells was substantially decreased upon addition of PU-H71 (Figure 9B), suggesting that probe **4** was also kicked out of the HSP90 binding pocket and re-assembled into nano-aggregates.

These results imply that the disassembly-driven turn-on probe can be used for the multi-color imaging.

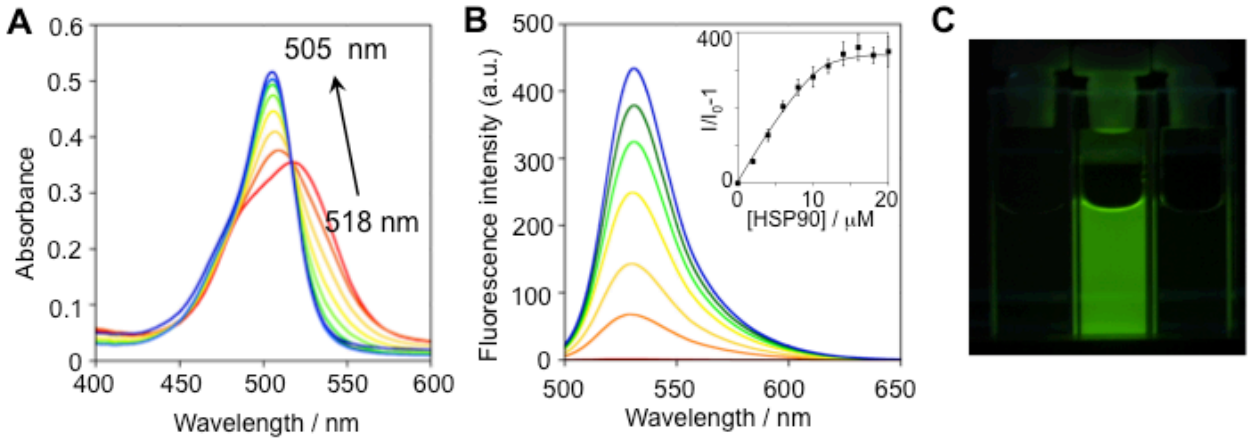

Figure 8. UV−vis absorption spectra changes of TMR-type probe **4** (10 μM) upon addition of HSP90-N (0−20 μM). (b) Fluorescence spectra changes of probe **4** (10 μM) upon addition of HSP90-N (0−20 μM) (λ_{ex} = 450 nm). (Inset) Fluorescence titration curve (λ_{em} = 530 nm). (c) Photographs of probe **4** (10 μM) in the absence or presence of HSP90-N (20 μM, left or middle, respectively), and after addition of PU-H71 (100 μM) to the solution of **4** and HSP90-N (right).

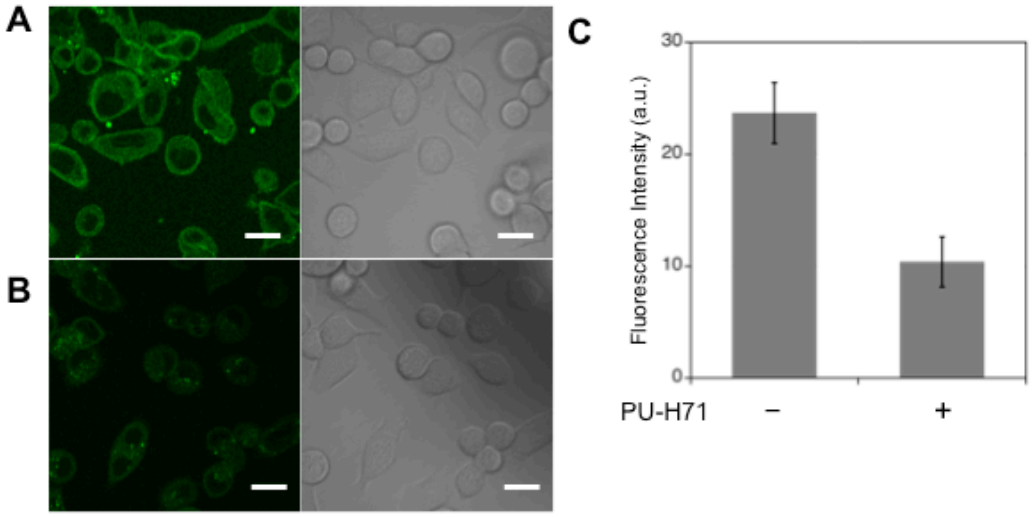

Figure 9. (**A**, **B**) CLSM images of SK-BR-3 cells treated with probe **4** (100 nM) for 12 h at 37ºC in cultured media (**A**) or after addition of PU-H71 (**B**, 10 μM). Scale bar, 20 mm. (c) Fluorescence intensity of intracellular region of **4**-stained SK-BR-3 cells with or without PU-H71. The intensities were evaluated at 10 cells in 5 regions in each dish, and the experiments were performed in triplicate to obtain mean and standard error values (shown as error bars).

4-3. Conclusion

In summary, the results indicate that the self-assembling supramolecular nanoprobe can be designed for turn-on imaging of endogeneous proteins even inside living cells. The quantitative study using an overexpressed model protein revealed that the designed nanoprobes form self-assembling aggregates in the signal-off mode in living cells in the absence of the target endogeneous protein, whereas the disassembly-driven turn-on fluorescent change is induced in the presence of the target by a specific ligand-protein recognition process. Interestingly, the addition of a competitive inhibitor induced the nanoprobe to re-assemble so that the fluorescence was turned off, explicitly verifying that the reversible assembly/disassembly of these supramolecular nanoprobes took place even inside the living cells. The intracellular reversibility of the collapse and formation of our self-assembled nanoaggregates is unprecedented. This dynamic sensing

mechanism allowed to construct a quantitative cell-based inhibitor assay for intracellular endogenous proteins such as hCAII and HSP90, two valuable diagnostic and therapeutic protein targets. This work should inspire new research into supramolecular approaches, which work inside cells in a programmable manner for cell-selective tissue engineering,[17] intracellular protein-triggered drug release, or cell signaling modulation.

4-4. Material and Method

General materials and methods:

Purified human carbonic anhydrase II (hCAII) was purchased from Sigma. Other chemical reagents and solvents were purchased from commercial chemical suppliers (Sigma, Aldrich, TCI, Wako, or Watanabe Chemical Industries) and used without further purification. ^{1}H NMR spectra were recorded on a Varian Mercury-400 spectrometer (400 MHz). High-resolution electrospray ionization Fourier transform mass spectrometry (HR-ESI-MS) spectra were recorded using a Thermo Scientific Exactive mass spectrometer. Cell imaging was performed with a confocal laser scanning microscope (CLSM, Olympus, FV1000, IX81) equipped with a 60×, NA = 1.35 oil objective lens. Fluorescence images were acquired using the 515-nm line of an argon laser to excite Rho-G (emission, 530−630 nm) and the 543-nm line of a HeNe Green laser to excite tetramethylrhodamine (emission, 555−655 nm). Hela cells, and MCF-7 cells were maintained in DMEM supplemented with 10% fetal bovine serum (FBS), penicillin (100 units/mL), and streptomycin (100 mg/ mL) at 37°C in 5% CO_2 and 95% air. SK-BR-3 cells were maintained in McCoy's 5A Modified Media supplemented with 10% FBS, penicillin (100 units/mL), and streptomycin (100 mg/ mL) at 37°C in 5% CO_2 and 95% air. The cells were plated at a density of

2.0×10^5 cells per a 35-mm glass-bottomed dish and cultured in the medium for 24 h at 37°C in 5% CO_2 and 95% air and used for fluorescence imaging.

Ultraviolet (UV)-Visible Absorption and Fluorescence Spectroscopic Analyses:

All probes were dissolved in dimethyl sulfoxide (DMSO) to generate stock solutions. The concentrations of probes **2**, **3,** and **4** were determined by their absorbance (at 543 nm for **2** and **3**, 504 nm for **4**) in methanol using a molar extinction coefficient of 92,000 M^{-1} cm^{-1} for **2** and **3**, and 78,000 M^{-1} cm^{-1} for **4**,[18] respectively. HCAII was dissolved in PBS buffer (pH 7.2), and HSP90-N was dissolved in 10 mM Tris buffer (pH 7.4). The concentrations of these proteins were determined by their absorbance at 280 nm using literature molar extinction coefficients of 54,000 M^{-1} cm^{-1} for hCAII[19] and 27,000 M^{-1} cm^{-1} for Hsp90-N, which was determined by its absorption spectra and BCA protein assay kit allowing stock solutions of known concentrations to be prepared. All experiments were performed at 25°C in test tubes. UV-visible absorption spectra were recorded on a Shimadzu UV-visible 2550 spectrometer. Fluorescence spectra were measured using a Perkin-Elmer LS55 fluorescent spectrometer. Absorption and fluorescence measurements were performed 30 min after adding the protein to each probe solution (10 μM stock solution).

Fluorescence Imaging in MCF7 Cells and SK-BR-3 Cells with Probes 2–4:

MCF7 cells plated on a 35-mm glass-bottomed dish were rinsed with $DMEM_i$, and treated with probe **2** (30 nM, <1% DMSO (v/v)) in $DMEM_i$ (1 mL). After incubation for 4 h, a stock solution of EZA was added (final concentration, 100 μM) to the cells. Fluorescence imaging was carried out 1 h after staining without performing any washing. SK-BR-3 cells plated on the 35-mm

glass-bottomed dish were rinsed with DMEM, and treated with probe **3** or **4** (100 nM, <1% DMSO (v/v)) or probe **3** or **4** (100 nM) and the corresponding inhibitor (<1% DMSO (v/v)) in DMEM (1 mL). Fluorescence imaging was carried out 4 h after staining without performing any washing.

Inhibitor Assay for hCAII in MCF7 Cells:

Probe **2** (100 nM) was added to the MCF-7 cells plated on a 35-mm glass-bottomed dish. After incubation for 4 h, a stock solution of each inhibitor was added to the cells. After an additional incubation for 1 h, fluorescence imaging was carried out without performing any washing. To determine the fluorescence intensity in the cell, CLSM images were analyzed with ImageJ 1.44 on a Macintosh PC.

Dynamic light scattering and atomic force microscopy:

DLS measurements were performed on NICOMP 380zls at 20 °C in 50 mM HEPES buffer (pH 7.2, 150 mM NaCl) using a plastic cuvette (3 ml volume). A DMSO stock solution of each compound was slowly added to the buffer solution to give a final concentration of 2 mM (1.0 % DMSO (v/v)) for probe **2** and 5 μM for probe **3**. All measurements were carried out in triplicate. In AFM imaging, a solution of each compound was spin-coated onto a freshly cleaved mica surface and dried *in vacuo*. Images of the samples were obtained with a tapping-mode AFM on a SHIMADSU SP-9600 microscope.

Expression and Purification of Hsp90-N:

Hsp90-N was expressed and purified according to a slight modification of the method reported

previously[13a]. Plasmids ppHSP90 purchased from Addgene were transformed into *E. coli* strain BL21 (DE3) and induced by 0.1 mM IPTG at OD_{650} = 0.8 for 15 h at 15^{o}C. Briefly, the cultures were harvested and the cells were resuspended in 20 mM tris (pH 8.0, 100 mM NaCl) buffer. Cells were disrupted by sonication and clarified by centrifugation. The supernatant was loaded onto a 5 ml Talon metal affinity column (Clontech) and eluted with buffer (100 mM Imidazole, 20 mM tris pH 8.0, 100 mM NaCl) and dialyzed in 10 mM Tris (pH 7.4) buffer. The concentration of the protein was determined by BCA assay.

Synthesis

Synthesis of probe 2

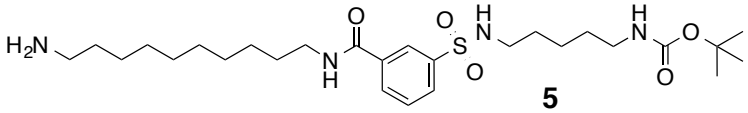

5

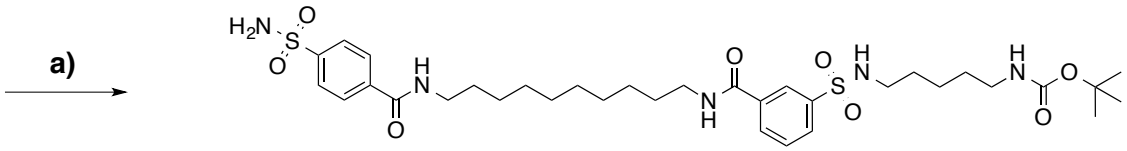

6

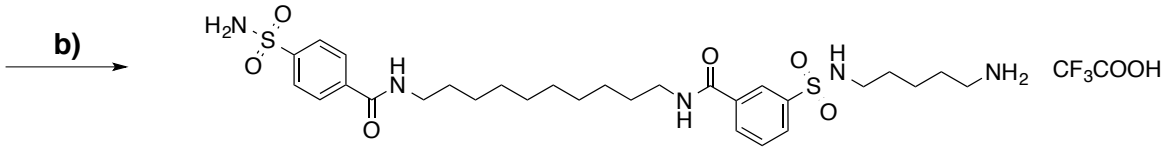

7

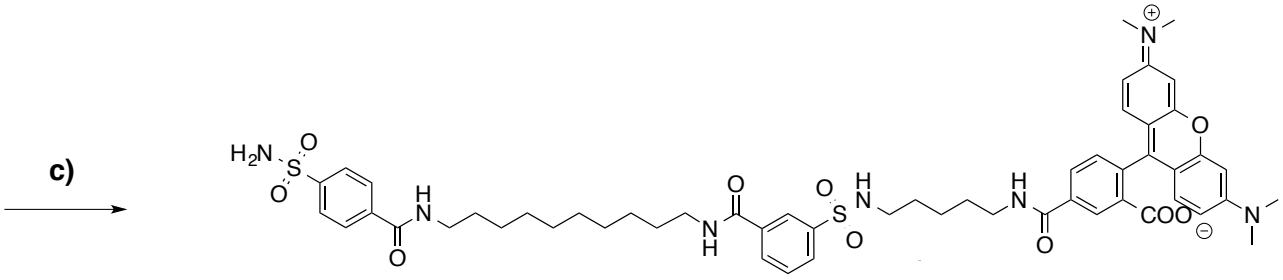

2

Scheme S1. Synthetic scheme of probe **2**. Reaction conditions: (a) SA-OSu, *N*,*N*-diisopropylethylamine (DIEA) in dry *N,N*-dimethylformamide (DMF); (b) trifluoroacetic acid (TFA) in CH_2Cl_2; (c) 5-carboxytetramethylrhodamine, *N,N,N',N'*-tetramethyl-*O*-(1*H*-benzotriazol-1-yl)uranium hexafluorophosphate (HBTU), DIEA in dry DMF.

Synthesis of 6

To a stirred dry DMF (1 ml) solution of **5**[8d] (50 mg, 92 mmol, 1.0 eq) and DIEA (50 µl, 0.29 mmol, 3.1 eq) was added SA-OSu[20] (33 mg, 0.11 mmol, 1.2 eq). The mixture was stirred at r.t. for 2 h. The solvent was evapolated. The residue was added $CHCl_3$ and was washed with sat. $NaHCO_3$ (50 ml x 3), 5% citric acid (50 ml) and brine (50 ml). The organic layer was collected and dried over $MgSO_4$. The solvent was evapolated to dryness to afford **6** as white solid (59 mg, 88%). ^{1}H NMR (CD_3OD, 400 MHz, r.t.). δ/ppm = 1.13-1.33 (m, 31H), 2.65-2.71 (m, 2H), 2.78-2.81 (m, 2H), 6.70 (m, 1H), 7.64-7.68 (m, 1H), 7.85-7.89 (m, 3H), 8.02 (d, J = 8.4 Hz, 2H), 8.04 (d, J = 8.0 Hz, 1H), 8.22 (s, 1H).

Synthesis of 7

To a stirred CH_2Cl_2 (4 ml) solution of **6** (59 mg, 82 µmol, 1.0 eq) was added TFA (2 ml). The mixture was stirred at r.t. for 1 h. The reaction was analysed by TLC (silica, $CHCl_3$: MeOH = 4 : 1) to confirm the completion. The solvent was removed by azeotropy with toluene (2 ml x 3) to afford **7** as colorless oil (60 mg, quantitatve). ^{1}H NMR (DMSO-d_6, 400 MHz, r.t.) δ/ppm = 1.26-1.50 (m, 22H), 2.68-2.71 (m, 4H), 3.14-3.23 (m, 2H), 7.65-7.69 (m, 1H), 7.64-7.68 (m, 1H), 7.85-7.89 (m, 3H), 7.95 (d, J = 8.4 Hz, 2H), 8.06 (d, J = 7.6 Hz, 1H), 8.22 (s, 1H).

Synthesis of 2

To a stirred DMF (500 µl) solution of **7** (6 mg, 8.1 µmol, 1.0 eq), DIEA (14 µl, 81 µmol, 10 eq), and 5-carboxytetramethylrhodamine was added HBTU (3.7 mg, 9.8 µmol, 1.2 eq). The mixure was stirred at room temperature for overnight. The solvent was evaporated. The residue was purified by

RP-HPLC (YMC Pack ODS-A, H_2O (containing 0.1% TFA): acetonitrile (conatinig 0.1% TFA) = 30 : 70 to 70: 30, linear gradient over 40 min, flow rate 9.999 ml/min) to give **2** (3.6 mg, 43%) as red solid. ^{1}H NMR (DMSO-d_6, 400 MHz, r.t.) δ/ppm = 1.28-1.60 (m, 22H), 2.92 (t, J = 6.8 Hz, 2H), 3.29-3.40 (m, 18H), 6.97 (d, J = 2.4 Hz, 2H), 7.05 (dd, J = 2.4 and 9.6 Hz, 2H), 7.14 (d, J = 9.6 Hz, 2H), 7.51 (d, J = 8.0 Hz, 1H), 7.64-7.68 (m, 1H), 7.89-8.03 (m, 6H), 8.25 (dd, J = 2.0 and 8.0 Hz 1H), 8.29 (m, 1H), 8.77 (d, J = 2.0 Hz, 1H). HR-FTMS (ESI): Calcd. for $[M(C_{54}H_{65}N_7O_{10}S_2)+H]^+$: m/z = 1036.4307; Found: 1036.4348.

Synthesis of Probe 2 and 3

Scheme S2. Synthetic scheme of probes **3** – **4**. Reaction conditions: (a) N-tert-Butoxycarbonyl -3-aminopropanol, triphenylphosphine (PPh_3) in dry diethyl diazenedicarboxylate (DEAD) in dry CH_2Cl_2; (b) TFA in CH_2Cl_2; (c) succinic anhydride, DIEA in dry CH_2Cl_2; (d) **9**, HBTU, 1-hydroxy-*1H*-benzotriazole monohydrate (HOBT•H_2O), DIEA; (e) TFA in CH_2Cl_2; (f) 5-carboxytetramethylrhodamine, HBTU, DIEA in dry DMF; (g) TFA in CH_2Cl_2; (h) 5-carboxyrhodamine 110, HBTU, DIEA in dry DMF.

Synthesis of 9

To a stirred dry CH_2Cl_2 (8 ml) sotluion of **8**[12a] (300 mg, 0.73 mmol, 1.0 eq), N-tert-Butoxycarbonyl-3-aminopropanol (191 mg, 1.09 mmol, 1.5 eq), and PPh_3 (381 mg, 1.45 mmol, 2.0 eq) was added DEAD (2.2 M in toluene, 1.65 ml, 3.6 mmol, 5.0 eq). The solvent was removed under reduced pressure. The crude was purified by column chromatography (silica, $CHCl_3$: MeOH = 10 : 1) to afford **9** as yellow film (241 mg, 58%). ^{1}H-NMR ($CDCl_3$, TMS, 400 MHz, rt): δ/ppm = 1.45 (s, 9H), 1.93 (m, 2H), 3.02 (m, 2H), 4.28 (t, J = 6.2 Hz, 2H), 5.51 (brs, 2H), 5.99 (s, 2H), 6.92 (s, 1H), 7.31 (s, 1H), 8.34 (s, 1H).

Synthesis of 10

To a stirred dry CH_2Cl_2 (2.0 ml) sotluion of **9** (300 mg, 0.73 mmol, 1.0 eq) was added TFA (2.0 ml). The solution was stirred at rt for 2h. The solvent was removed under reduced pressure. The volatile was removed by azeotropy with toluene (2 ml x 3) to afford **10** as white solid (133 mg, quantitative yield). ^{1}H-NMR (CD_3OD, 400 MHz, rt): δ/ppm = 2.26 (m, 2H), 3.05 (t, J = 7.6 Hz, 2H), 4.43 (t, J = 6.8 Hz, 2H), 6.09 (s, 2H), 7.26 (s, 1H), 7.49 (s, 1H), 8.34 (s, 1H).

Synthesis of 11

To a stirred dry DMF (5 ml) solution of **5** (150 mg, 0.27 mmol, 1.0 eq) and succinic anhydride (31 mg, 0.31 mmol, 1.1 eq), was added DIEA (145 µl, 0.83 mmol, 3.1 eq). The solution was stirred at rt for 1h. To this solution was added ethylenediamine dihydrochlorate (7.4 mg). The solvent was removed under reduced pressure. The residue was added 5% citric acid and extracted with $CHCl_3$ (100 ml x 3). The combined organic layer was dried over $MgSO_4$. The solvent was evaporated to

dryness to afford **11** as white solid (133 mg, 75%). ^{1}H NMR (CD_3OD, 400 MHz, rt): δ/ppm = 1.28-1.55 (m, 29H), 1.60-1.65 (m, 2H), 2.26 (t, J = 6.8 Hz, 2H), 3.05 (t, J = 6.8 Hz, 2H), 4.43 (m, 6H), 6.09 (t, J = 7.2 Hz 2H), 7.26 (m, 1H), 7.49 (m, 2H), 8.31 (m, 1H).

Synthesis of 12

To a stirred dry DMF (1 ml) sotluion of **11** (15 mg, 23 μmol, 1.0 eq) and HOBT•H_2O (5.4 mg, 35 μmol, 1.5 eq), **3** (18 mg, 31 μmol, 1.3 eq), and DIEA (20 μl, 115 μmol, 5.0 eq), was added HBTU (13 mg, 34 μmol, 1.5 eq). The solution was stirred at rt for 2h. The solvent was removed under reduced pressure. The residue was purified by column chromatography (silica, $CHCl_3$: MeOH = 50 : 1 to 20 : 1) to afford **12** as white amorphous (13 mg, 51%). ^{1}H NMR ($CDCl_3$, 400 MHz, rt): δ/ppm = 1.28-1.46 (m, 29H), 1.61-1.65 (m, 2H), 2.02-2.06 (m, 2H), 2.48-2.51 (m, 4H), 2.85-3.36(m, 10H), 4.28 (t, J = 7.4 Hz, 2H), 6.07 (s, 2H), 7.12 (s, 1H), 7.42 (s, 2H), 7.62-7.74 (m, 1H), 7.96-8.03 (m, 2H), 8.18 (s, 1H), 8.29 (s, 1H).

Synthesis of 3

To a stirred dry CH_2Cl_2 (2 ml) soluion of **12** (3 mg, 2.7 μmol, 1.0 eq) was added TFA (1 ml). The solution was stirred at rt for 2 h. The solvent was removed under reduced pressure. The volatile was removed by azeotropy with toluene (1 ml x 3). The residue was dissolved in DMF (500 μl). To this solution was added 5-carboxytetramethylrhodamine (1.7 mg, 4.0 mmol, 1.5 eq), DIEA (5 μl, 29 μmol, 11 eq), and HBTU (1.6 mg, 4.2 μmol, 1.6 eq). The solvent was removed under reduced pressure. The residue was purified by RP-HPLC (YMC-Pack, ODS-A, H_2O (containing 0.1% TFA) : acetonitrile (containing 0.1% TFA) = 70:30 to 30:70, linear gradient over 40 min, flow rate

9.999 ml/min) to afford **3** as purple solid (2.6 mg, 67%). ^{1}H-NMR ($CDCl_3/CD_3OD$ = 1/5, 400 MHz, rt): δ/ppm = 1.25-1.61 (m, 22H), 2.02-2.08 (m, 2H), 2.40-2.50 (m, 4H), 2.91 (t, J = 6.8 Hz, 2H), 3.03-3.22(m, 8H), 4.28 (t, J = 7.6 Hz, 2H), 6.05 (s, 2H), 6.89 (d, J = 2.4 Hz, 2H), 6.96 (dd, J = 2.4 and 9.6 Hz, 2H), 7.10-7.14 (m, 3H), 7.39-7.43 (m, 2H), 7.60-7.62 (m, 1H), 7.95-8.10 (m, 2H), 8.21-8.27 (m, 3H), 8.77 (m, 1H). HR-FTMS (ESI): Calcd. for $[M(C_{66}H_{77}IN_{12}O_{11}S_2)+H]^+$: *m/z* = 1405.4374; Found: 1405.4394.

Synthesis of 4

To a stirred dry CH_2Cl_2 (2 ml) soluion of **12** (3 mg, 2.7 μmol, 1.0 eq) was added TFA (1 ml). The solution was stirred at rt for 2 h. The solvent was removed under reduced pressure. The volatile was removed by azeotropy with toluene (1 ml x 3). The residue was dissolved in DMF (500 μl). To this solution was added 5-carboxyrhodamine 110 (1.5 mg, 4.0 μmol, 1.5 eq), DIEA (5 μl, 29 μmol, 11 eq), and HBTU (1.6 mg, 4.2 μmol, 1.6 eq). The solvent was removed under reduced pressure. The residue was purified by RP-HPLC (YMC-Pack, ODS-A, H_2O (containing 0.1% TFA) : acetonitrile (containing 0.1% TFA) = 70:30 to 30:70, linear gradient over 40 min, flow rate 9.999 ml/min) to afford **4** as red solid (1.0 mg, 27%). ^{1}H-NMR ($CDCl_3/CD_3OD$ =1/5, 400 MHz, rt): δ/ppm = 1.26-1.62 (m, 22H), 2.05-2.15 (m, 2H), 2.46-2.50 (m, 4H), 2.91 (t, J = 6.8 Hz, 2H), 3.09-3.48 (m, 8H), 4.31 (t, J = 7.6 Hz, 2H), 6.06 (s, 2H), 6.80 (m, 4H), 7.05 (d, J = 9.2 Hz, 2H), 7.21 (s, 1H), 7.45 (s, 1H), 7.64-7.68 (m, 1H), 7.98-8.03 (m, 2H), 8.22-8.29 (m, 3H), 8.74 ppm (m, 1H). HR-FTMS (ESI): Calcd. for $[M(C_{62}H_{69}IN_{12}O_{11}S_2)+H]^+$: *m/z* = 1349.3755; Found: 1349.3768.

References:

(1) (a) Giepmans, B. N. G.; Adams, S. R.; Ellisman, M. H.; Tsien, R. Y. *Science*, **2006**, *312*, 217–224. (b) Kobayashi, H.; Ogawa, M.; Alford, R.; Choyke, P. L.; Urano, Y. *Chem. Rev.* **2010**, *110*, 2620–2640.

(2) (a) Zhang, H.; Fan, J. L.; Wang, J. Y.; Zhang, S. Z.; Dou, B. R.; Peng, X. J. *J. Am. Chem. Soc.* **2013**, *135*, 11663−11669. (b) Tang, R.; Kim, C. S. Solfiell, D. J.; Rana, S.; Mout, R.; Vela´zquez-Delgado, E. M.; Chompoosor, A.; Jeong, Y.; Yan, B.; Zhu, Z.-J.; Kim, C.; Hardy, J. A.; Rotello V. M. *ACS Nano*, **2013**, *7*, 6667–6673.

(3) (a) Azagarsamy, M. A.; Yesilyurt, V.; Thayumanavan, S. *J. Am. Chem. Soc.* **2010**, *132*, 4550–4551. (b) You, C. C.; Miranda, O. R.; Gider, B.; Ghosh, P. S.; Kim, I. B.; Erdogan, B.; Krovi, S. A.; Bunz, U. H. F.; Rotello, V. M. *Nat. Nanotechnol.* **2007**, *2*, 318–323.

(4) (a) Cabral, H.; Nishiyama, N.; Kataoka, K. *Acc. Chem. Res*. **2011**, *44*, 999–1008. (b) Sapsford, K. E; Algar, W. R.; Berti, L.; Gemmill, K. B.; Casey, B. J.; Oh, E.; Stewart, M. H.; Medintz, I. L. *Chem. Rev.* **2013**, *113*, 1904–2074.

(5) (a) Liang, G.; Ren, H. J.; Rao, J. H. *Nat. Chem.* **2010**, *2*, 54–60. (b) Ye, D.; Shuhendler, A. J.; Cui, L.; Tong, L.; Tee1, S. S.; Tikhomirov, G.; Felsher, D. W.; Rao, J. *Nat. Chem.* **2014**, *6*, 519–526.

(6) (a) Gao, Y.; Shi, J. F.; Yuan, D.; Xu, B.; *Nat. Commun.* **2012**, *3*, DOI: 10.1038/ncomms2040. (b) Li, J.;Gao, Y.; Kuang, Y.; Junfeng Shi, J.; Du, X.; Zhou, J.; Wang, H.; Yang, Z.; Xu, B. *J. Am. Chem. Soc.* **2013**, *135*, 9907–9914.

(7) (a) Ding, D., Kai, L. K., Liu, B., & Tang, B. Z. *Acc. Chem. Res.* **2013**, *46,* 244–2453. (b) Shi, H.; Liu, J.; Geng, J.; Tang, B. Z.; Liu, B. *J. Am. Chem. Soc.* **2012**, *134*, 9569–9572.

(8) (a) Takaoka, Y.; Sakamoto, T.; Tsukiji, S.; Narazaki, M.; Matsuda, T.; Tochio, H.; Shirakawa, M.; Hamachi, I. *Nat. Chem.* **2009**, *1*, 557–561. (b) Takaoka, Y.; Kiminami, K.; Mizusawa, K.; Matsuo, K.; Narazaki, M.; Matsuda, T.; Hamachi, I. *J. Am. Chem. Soc.* **2011**, *133*, 11725–11731. (c) Mizusawa, K.; Mizusawa, K.; Ishida, Y.; Takaoka, Y.; Miyagawa, M.; Tsukiji, S.; Hamachi, I. *J. Am. Chem. Soc.* **2010**, *132*, 7291–7293. (d) Mizusawa, K.; Takaoka, Y.; Hamachi, I. *J. Am. Chem. Soc.* **2012**, *134*, 13386–13995.

(9) Supuran, C. T. *Nat. Rev. Drug. Discov.* **2008**, *7*, 168–181.

(10) Casisni, A.; Abbate, F.; Scozzafava, A. Supuran, C. T. *Bioorg. Med. Chem. Lett.* **2003**, *13*, 2759–2763.

(11) (a) Trepel, J.; Mollapour, M.; Giaccone, G.; Neckers, L. *Nat. Rev. Cancer.* **2010**, *10*, 537–549. (b) Chiosis, G.; Neckers, L. *ACS Chem. Biol.* **2006**, *1*, 279–284.

(12) (a) He, H.; Zatorska, D.; Kim, J.; Aguirre, J.; Llauger, L.; She, Y.; Wu, N.; ,†Immormino, R. M. Gewirth, D. T.; Chiosis, G. *J. Med. Chem*. **2006**, *49*, 381–390. (b) Modi, S.; Stopeck, A.; Linden, H.; Solit, D.; Chandarlapaty, S.; Neal Rosen, N.; D'Andrea, G.; Dickler, M.; Moynahan, M. E.; Sugarman, S.; Ma, W.; Patil, S.; Norton, L.; Hannah,A. L.; Clifford Hudis, C. *Clin. Cancer Res.* **2011***, 17*, 5132–5139.

(13) (a) Prodromou, C.; Piper, P. W.; Peal, L. H. *Proteins: Struct., Funct., Genet.* **1996**, *25*, 517–522. (b) Maroney, A. C.; Marugan, J. J.; Mezzasalma, T. M.; Barnakov, A. N.; Garrabrant, T. A.; Weaner, L. E.; Jones, W. J.; Barnakova, L. A. Koblish, H. K.; Todd, M. J.; Masucci, J. A.; Deckman, I. C.; Galemmo, R. A., Jr.; Johnson, D. L. *Biochemistry* **2006**, *45,* 5678–5685.

(14) (a) Chiosis, G.; Timaul, M. N.; Lucas, B.; Munster, P. N.; Zheng, F. F.; Sepp-Lorenzino, L.; Rose, N. *Chem. Biol.* **2001**, *8*, 289–299. (b) Taldone, T. Gomes-DaGama, E. M. Zong, H.; Sen, S.; Alpaugh, M. L.; Zatorska, D.; Alonso-Sabadell, R.; Guzman, M. L.; Chiosis, G. *Bioorg. Med. Chem. Lett.* **2011**, *21*, 5347–5352.

(15) Kim, S.-H. Bajji, A.; Tangallapally, R.; Markovitz, B.; Trovato, R.; Shenderovich, M.; Baichwal, V.; Bartel, P.; Cimbora, D.; McKinnon, R.; Robinson, R.; Papac, D.; Wettstein, D.; Carlson, R.; Yager, K. M. *J. Med. Chem.* **2012**, *55*, 7480-7501.

(16) Hartmann F.; Horak, E. M.; Cho, C.; Lupu, R.; Bolen J. B.; Stetler-Stevenson M. A.; Pfreundschuh M.; Waldmann T. A.; Horak I. D. *Int. J. Cancer* **1997**, *70*, 221–229 (1997).

(17) Hirata, N.; Nakagawa, M.; Fujibayashi, Y.; Yamauchi, K.; Murata, A.; Minami, I.; Tomioka, M.; Kondo, T.; Kuo, T. F.; Endo, H.; Inoue, H.; Sato, S.; Ando, S.; Kawazoe, Y.; Aiba, K.; Nagata, K.; Kawase, E.; Chang, Y.T.; Suemori, H.; Eto, K.; Nakauchi, H.; Yamanaka, S.; Nakatsuji, N.; Ueda, K.; Uesugi, M. *Cell Reports* **2014**, *6*, 1165–1174.

(18) Haugland, R. P. The handbook: a guide to fluorescent probes and labeling technologies, 10th

ed.; Invitrogen: Carlsbad, CA, 2005.

(19) Supuran, C. T., Briganti, F., Tilli, S., Chegwidden, W. R. Scozzafava, A. *Bioorg. Med. Chem*. **2001**, *9*, 703–714.

(20) Tsukiji, S.; Miyagawa, M.; Takaoka, Y.; Tamura, T.; Hamachi, I. *Nat. Chem. Biol.* **2009**, *5*, 341–34.

List of Publications

Chapter 1 Montmorillonite-Supramolecular Hydrogel Hybrid for Fluorocolorimetric Sensing of Polyamines

Masato Ikeda, Tatsuyuki Yoshii, Toshihiro Matsui, Tatsuya Tanida, Harunobu Komatsu, and Itaru Hamachi

J. Am. Chem. Soc. **2011**, *133*, 1670–1673.

Chapter 2 Two-photon responsive supramolecular hydrogel for controlling materials motion in micrometer space

Tatsuyuki Yoshii, Masato Ikeda, Itaru Hamachi

Angew. Chem., Int. Ed. **2014**, *53*, 7264–7267.

Chapter 3 Reversible Assembly/Disassembly of Nanoprobes for Turn-on Fluorescent Imaging of Intracellular Proteins in Live Cells

Yousuke Takaoka, Tatsuyuki Yoshii, Keigo Mizusawa, Itaru Hamachi

Manuscript in preparation

Other Publications

1. Installing Logic Gate Response to a Variety of Biological Substances in Supramolecular Hydrogel-Enzyme Hybrids

   Masato Ikeda, Tatsuya Tanida, Tatsuyuki Yoshii, Kazuya Kurotani, Shoji Onogi, Kenji Urayama, Itaru Hamachi

   Nature Chemistry, **2014**, *6*, 511–518.

2. A supramolecular hydrogel containing boronic acid-appended receptor for fluorocolorimetric sensing of polyols with a paper platform

   Masato Ikeda, Keisuke Fukuda, Tatsuya Tanida, Tatsuyuki Yoshii, Itaru Hamachi.

   Chemical Communications, **2012**, *48*, 2716–2718.

3. Rational molecular design of stimuli-responsive supramolecular hydrogel based on dipeptide

   Masato Ikeda, Tatsuya Tanida, Tatsuyuki Yoshii, Itaru Hamachi

   Advanced Materials, **2011**, *23*, 2819–2822.

Review and Books

「超分子ヒドロゲル」

吉井　達之・黒谷和哉・浜地　格

遺伝子医学BOOK別冊　ここまで広がるドラッグ徐放技術の最前線　古くて新しいドラッグデリバリーシステム(DDS), メディカルドゥ, 124–130.

「セミウェット材料としての超分子ヒドロゲル」

吉井　達之・浜地　格

機能材料, 第 32 巻, 第 3 号, 13–17, シーエムシー出版.

List of Presentation

1. Photo-fabricaiton of the peptide-based supramolecular hydrogel by two-photon excitation

   Tatsuyuki Yoshii, Masato Ikeda, Itaru Hamachi

   62th Symposium on Macromolecules, Ishikawa, Japan (2013).

2. Supramolecular hydrogel for biological applications (1): Development of two-photon responsive hydrogel

   Tatsuyuki Yoshii, Masato Ikeda, Itaru Hamachi

   93th Annual Meeting of Chemical Society of Japan, Shiga, Japan (2013).

3. Biofunctional supramolecular materials (4): Controlling dynamic behavior of supramolecular machine in living cell

   Tatsuyuki Yoshii, Masato Ikeda, Itaru Hamachi

   92th Annual Meeting of Chemical Society of Japan, Kanagawa, Japan (2012).

4. Development of polyamine sensor by hybridization of supramolecular hydrogel and montmorillonite

   Tatsuyuki Yoshii, Masato Ikeda, Itaru Hamachi

   60th Symposium on Macromolecules, Okayama, Japan (2013).

5. Supramolecular soft matrix (2): Highly-sensitive detection of polyamine using supramolecular hydrogel and MMT hybrid material

Tatsuyuki Yoshii, Toshihiro Matsui, Harunobu Komatsu, Masato Ikeda, Itaru Hamachi

91th Annual Meeting of Chemical Society of Japan, Presentation Program, Japan (2011).

6. New development of supramolecular matrix (2): Introduction of an orthogonal domain into supramolecular hydrogel and the development of functional materials

Tatsuyuki Yoshii, Atsuhiko Wada, Masato, Ikeda, Itaru Hamachi

89th Annual Meeting of Chemical Society of Japan, Chiba, Japan (2009).

7. In-cell imaging of endogenous protein by self-assembled fluorescent nano-probe

Tatsuyuki Yoshii, Keigo Mizusawa, Yousuke Takaoka, Itaru Hamachi

14th Forum on Biomolecular Chemistry. Shizuoka, Japan (2014).

8. Development of two-photon responsive supramolecular hydrogel

Tatsuyuki Yoshii, Masato Ikeda, Itaru Hamachi

The 24th Symposium on Biofunctional Chemistry Summer School, Tokyo, Japan (2013)

9. Intracellular derivery and controlling dynamic behavior of rotaxane molecule

Tatsuyuki Yoshii, Masato Ikeda, Itaru Hamachi

6th Joint Symposium on Biorelevant Chemistry, Hokkaido, Japan (2012)

10. Development of photo-responsive supramolecular hydrogel

Tatsuyuki Yoshii, Masato Ikeda, Itaru Hamachi

The 23rd Symposium on Biofunctional Chemistry Summer School. Fukuoka, Japan (2012)

11. Development of colorimetric polyamine sensor by hybridization of supramolecular hydrogel and montmorillonite

Tatsuyuki Yoshii, Masato Ikeda, Itaru Hamachi

The 22nd Symposium on Biofunctional Chemistry Summer School, Hiroshima, Japan (2011)

12. Construction of photo-responsive supramolecular hydrogel

Tatsuyuki Yoshii, Masato Ikeda, Itaru Hamachi

58th Symposium on Macromolecules, Kumamoto, Japan (2009).